


Spring 2018

# 3D Bioprinting Systems for the Study of Mammary Development and Tumorigenesis

John Reid  
*Old Dominion University*

Follow this and additional works at: [https://digitalcommons.odu.edu/ece\\_etds](https://digitalcommons.odu.edu/ece_etds)

 Part of the [Biology Commons](#), [Biomedical Commons](#), and the [Biomedical Engineering and Bioengineering Commons](#)

---

## Recommended Citation

Reid, John. "3D Bioprinting Systems for the Study of Mammary Development and Tumorigenesis" (2018). Doctor of Philosophy (PhD), dissertation, Electrical/Computer Engineering, Old Dominion University, DOI: 10.25777/d1hj-6a76  
[https://digitalcommons.odu.edu/ece\\_etds/28](https://digitalcommons.odu.edu/ece_etds/28)

This Dissertation is brought to you for free and open access by the Electrical & Computer Engineering at ODU Digital Commons. It has been accepted for inclusion in Electrical & Computer Engineering Theses & Dissertations by an authorized administrator of ODU Digital Commons. For more information, please contact [digitalcommons@odu.edu](mailto:digitalcommons@odu.edu).

**3D BIOPRINTING SYSTEMS FOR THE STUDY OF MAMMARY DEVELOPMENT  
AND TUMORIGENESIS**

by

John Reid  
B.A. May 2009, Hampden-Sydney College

A Dissertation Submitted to the Faculty of  
Old Dominion University in Partial Fulfillment of the  
Requirements for the Degree of

DOCTOR OF PHILOSOPHY

BIOMEDICAL ENGINEERING

OLD DOMINION UNIVERSITY

May 2018

Approved by:

Patrick C. Sachs (Co-Director of  
Committee)

Dean J. Krusienski (Co-Director of  
Committee)

Robert D. Bruno (Member)

Christian W. Zemlin (Member)

Roy C. Ogle (Member)

## ABSTRACT

### 3D BIOPRINTING SYSTEMS FOR THE STUDY OF MAMMARY DEVELOPMENT AND TUMORIGENESIS

John Anderson Reid  
Old Dominion University, 2018  
Co-Directors: Dr. Patrick C. Sachs  
Dr. Dean J. Krusienski

Understanding the microenvironmental factors that control cell function, differentiation, and stem cell renewal represent the forefront of developmental and cancer biology<sup>1</sup>. To accurately recreate and model these dynamic interactions *in vitro* requires both precision-controlled deposition of multiple cell types and well-defined three-dimensional (3D) extracellular matrix (ECM). To achieve this goal, we hypothesized that accessible bioprinting technology would eliminate the experimental inconsistency and random cell-organoid formation associated with manual cell-matrix embedding techniques commonly used for 3D, *in vitro* cell cultures. The first objective of this study was to adapt a commercially-available, 3D printer into a 3D bioprinter. Goal-based computer simulations were used to identify, evaluate, and optimize the performance of a 3D bioprinting system. Implementing these findings yielded a bioprinting system with reduced needle clogging and single cell print resolution. The minimal disruption of cell function was confirmed by the retention of pluripotency marker TRA-1-81 in bioprinted human induced pluripotent stem cells (hiPSCs) 7-days post-printing. This system was then used to investigate cell behavior during the initial stages of organoid-structure formation by generating 3D bioprinted arrays of individual, mammary epithelial cell (MEC) organoid-structures. This quantifiable, 3D bioprinting approach, was able to direct the ‘self-assembly’ of large MEC structures through organoid ‘fusion’ events among individual, bioprinted organoids along the printing template. Bioprinting maintained experimental consistency among multiple 3D scaffolds and experimental conditions, and presents the capability to generate high-fidelity, 3D arrays with multiple cell types. Compared to manual matrix embedding, bioprinted, co-culture experiments, containing normal MECs and breast cancer cell lines, significantly increased the ability to generate chimeric (tumor/normal) MEC structures. Thus, bioprinting stands highly qualified to investigate the role of microenvironmental processes related to cell fate determination and tissue formation.

Copyright, 2018, by John Anderson Reid, All Rights Reserved.

## **ACKNOWLEDGMENTS**

I extend many thanks to my committee members for their patience, advice and encouragement.

## NOMENCLATURE

<i>BM</i>	Basement Membrane
<i>CAD</i>	Computer-Aided-Design
<i>CFD</i>	Computational Fluid Dynamics
<i>Ck5</i>	Cytokeratin 5
<i>Ck8</i>	Cytokeratin 8
<i>CNC</i>	Computer-Numerically Controlled
<i>Cx30</i>	Connexin 30
<i>Cx32</i>	Connexin 32
<i>EB</i>	Embryoid Body
<i>ECM</i>	Extracellular Matrix
<i>FEM</i>	Finite Element Modeling
<i>GFP</i>	Green Fluorescent Protein
<i>GJ</i>	Gap Junction
<i>GJIC</i>	Gap Junctional Intercellular Communication
<i>hiPSC</i>	Human Induced Pluripotent Stem Cell
<i>MEC</i>	Mammary Epithelial Cell
<i>RFP</i>	Red Fluorescent Protein
<i>TEB</i>	Terminal End Bud

## TABLE OF CONTENTS

	Page
LIST OF TABLES .....	viii
LIST OF FIGURES .....	ix
Chapter	
1 INTRODUCTION .....	11
1.1 Overview .....	11
1.2 Mammary Gland Formation .....	14
1.3 The Use of 3D Culture Systems to Study Epithelial Biology .....	19
1.4 Bioprinting Platforms in Biological Research .....	22
2. DESIGN RATIONALE, DEVELOPMENT, AND UTILIZATION OF A 3D BIOPRINTING DEVICE .....	26
2.1 Overview .....	26
2.2 Introduction .....	27
2.3 Materials and Methods .....	29
2.4 Results .....	36
2.5 Discussion .....	49
3. 3D BIOPRINTING MAMMARY EPITHELIAL ORGANOIDs .....	53
3.1 Overview .....	53
3.2 Introduction .....	54
3.3 Materials and Methods .....	56
3.4 Results .....	59
3.5 Discussion .....	75
3.6 Conclusion .....	77
4. 3D BIOPRINTING CHIMERIC MEC ORGANOIDs .....	78
4.1 Overview .....	78
4.2 Introduction .....	80
4.3 Materials and Methods .....	81
4.4 Results .....	84
4.5 Discussion .....	107
4.6 Conclusion .....	108
5. SUMMARY AND FUTURE WORK .....	109
5.1 Summary of the Current Study .....	109
5.2 Additional Considerations for Future Research .....	110
5.3 Future Directions for Bioprinting in MEC Research .....	114
5.4 Conclusion .....	117
REFERENCES .....	119

	Page
APPENDICES	
A: GELATION PROTOCOL FOR COLLAGEN I, RAT TAIL .....	125
VITA .....	126



**LIST OF TABLES**

Table	Page
1: Analytical solutions to CFD simulations of the bioprinting process using various microneedle geometries. -----	37
2. Evaluation of chimeric organoid formation. -----	97

## LIST OF FIGURES

Figure	Page
1. CAD design and 3D printing of bioprinter modifications to the Felix 3.0. -----	35
2. CFD particle studies of the bio-deposition process under conditions that favor aggregation. -----	40
3. Shear Rate results from CFD particle studies of the bio-deposition process using various microneedle geometries. -----	42
4. MCF-12A alamar blue cell viability studies post-printing. -----	44
5. Printer resolution and functional limitations. -----	46
6. 3D printed hiPSCs. -----	48
7. Manual method of MCF-12A Organoid Formation. -----	60
8. Design of the 3D bioprinting platform. -----	62
9. Bioprinting results in consistent organoid formation. -----	64
10. Organoid fusion occurs between organoids printed up to 500 $\mu$ m apart. -----	65
11. Maturation and formation of MCF-12A organoids. -----	67
12. Directed printing of non-linear organoids. -----	69
13. Alternating RFP/GFP MCF-12A cell deposits to form contiguous organoids. -----	70
14. Alternating RFP/GFP MCF-12A cell deposits in human collagen. -----	72
15. Immunofluorescent staining of MCF-12A cell organoids in human collagen. -----	74
16. 3D Bioprinting consistent breast tumor organoids. -----	85
17. Histological analysis of bioprinted MCF-7 breast tumor organoids. -----	86
18. Histological analysis of bioprinted MDA-MB-468 breast tumor organoids. -----	87
19. Comparison of 3D bioprinted, epithelial organoid-structures. -----	88
20. Collagen density affects morphology of MCF-7 organoid structures. -----	89

Figure	Page
21. Quantitative analysis of Ki-67 positive epithelial cells grown in 1.0 mg/ml collagen gel.-----	91
22. Bioprinted multicellular assays are more efficient than manual method. -----	92
23. Within 7 days, 3D bioprinting enabled the reliable formation of large chimeric mammary epithelial organoid-structure containing (a) tumorigenic cells (MDA-MB-468) and (b) ‘normal’ MCF-12A cells.-----	93
24. Within 21 days, initial mixtures of ‘normal’ MCF-12A cells and tumorigenic cells MDA-MB-468 undergo coordinated organoid fusion events to generate a large chimeric epithelial organoid-structure.-----	94
25. Distribution of normal and tumorigenic cell types in chimeric organoids. -----	99
26. Immunohistochemical comparison of cadherin expression in chimeric epithelial organoids.-----	100
27. Immunohistochemical comparison of connexin expression in chimeric epithelial organoids containing MCF-7 and MCF-12A cells. -----	101
28. Immunohistochemical comparison of connexin 30 (Cx30) expression in chimeric epithelial organoids containing MDA-MB-468 and MCF-12A cells. -----	102
29. Immunohistochemical comparison of connexin 32 (Cx32) expression in chimeric epithelial organoids containing MDA-MB-468 and MCF-12A cells. -----	103
30. Manipulating cell-cell interactions through bioprinting. -----	104
31. Alternative methods for generating chimeric organoids. -----	105
32. Bioprinted breast organoids form ‘TEB-like’ morphologies.-----	113
33. Algorithm to standardize measurement of histological data. -----	116

The cell is a wonderfully complex and precise little mechanism;  
disease is but disorder of this mechanism.  
The aim of medicine is to prevent or repair such disorders.  
The aim of biology is to understand the cellular machinery.

A. Szent-Györgyi

## CHAPTER 1

### INTRODUCTION

#### 1.1 Overview

The focus of most tissue engineering research tries to identify the unique processes that enable cells to make tissues with a different form and function. It turns out that a substantial amount of gene expression in cells originates from signals in the micro-environment. However, as with most things, our ability to study this has been limited due to a lack of available technology. For example, because the iconic, flat-surface of a plastic petri-dish fails to mimic real-world conditions, cells grown in two-dimensional (2D) environments do not carry out their tissue-specific functions. As a result, we now understand that the structure of a tissue or organ is indispensable for its function. This is important because most of the information about cell biology we have today originated from 2D cultures. Thus, many treatment options currently available to clinicians were derived from flat-plastic, 2D, monolayer cultures. So, while numerous genomic and gene expression arrays can provide evidence of a cell's status or identity, these results mean little unless we can provide the cells with a 3D environment that recapitulates the 'context' presented in the real-world structure. While animal models have provided a large amount of evidence of the importance of tissue microenvironments in regulating cellular behavior, they limit our ability to identify the specific features involved in this process. Thus, a huge challenge for breast cancer research comes from the need to incorporate 'context' into *in vitro* research models.

From computational fluid dynamics (CFD) to additive manufacturing, the main goal of this work attempts to implement engineering technology and techniques to design 3D, *in vitro* models

which better recapitulate the *in vivo* situation. To achieve this, we hypothesized that accessible bioprinting technology would eliminate the experimental inconsistency and random cell-organoid formation associated with manual cell-matrix embedding techniques commonly used for 3D, *in vitro* cell cultures. Specifically, to improve upon our current understanding of the cell-cell interactions associated with human tissue micro-environments, this work attempted to use accessible 3D bioprinting techniques to increase our ability to create ‘contextual’ information by reliably patterning multiple cell types inside 3D, *in vitro* models using human based ‘bio-inks’. We began this study by designing an accessible, 3D bioprinter to deposit small cell quantities inside 3D environments. Next, we used this system to determine the necessary parameters to reliably generate MEC organoid-structures in a 3D environment. Last, we investigated the ability to reliably generate ‘chimeric’ organoids composed of ‘normal’ MECs and tumorigenic cell lines.

Chapter 1 begins with a summary of MEC biology. This sets fourth information about the growth and development of the mammary gland. This information provides a general understanding of the dynamic relationships among the unique cell populations, physical environment, and cyclical nature of mammary gland growth and regulation. Using these criteria as a guide, the next portion presents the current ability of 3D cell culture methods to generate *in vitro* models of mammary gland biology. This includes a general overview of a typical 3D cell culture experiment. Chapter 1 concludes with a description of how limitations of current 3D cell culture methods negatively impact the ability to standardize 3D cell culture research.

Chapter 2 provides the first contribution of the dissertation, which is the design and optimization of an extrusion device to reliably print small quantities of cells. This includes detailed information about the hardware components of the system, an overview of a typical 3D bioprinting printing experiment, and additional variables related to tailoring the instrument for the specific needs of a given experiment.

Chapter 3 details the use of the bioprinting system to identify the necessary printing parameters to reliably control MEC organoid formation. This chapter provides the second contribution of this dissertation, which is the identification of the unique printing parameters related to MEC organoid formation. By standardizing the cell quantity and proximity among individual cell-deposits, a uniform rate of organoid formation was achieved in bioprinted arrays of MECs. Identifying these printing parameters enabled the development of a more reliable and practical 3D culture model for studying MEC morphogenesis and epithelial biology.

Chapter 4 presents the utilization of a bioprinting apparatus to reliably generate chimeric, luminal-structures of normal MCF-12A cells and tumorigenic cells. The characterization of these interactions represents the third main contribution of this dissertation. The comparative analysis of subcellular proteins of normal, tumorigenic, and chimeric (tumor/normal) organoids contributed to a better understanding of the aberrant signaling associated with the neoplastic state. Overall, Chapters 2, 3, and 4 illustrate the common features of bioprinter operation and important variables for designing experimental protocols using bioprinters.

Chapter 5 presents the conclusion of these studies, along with a discussion and summary of the main results of the dissertation, as well as proposing future extensions of this research. Using bioprinting techniques to reliably deposit user-specified cell quantities in defined spatial-coordinates, our results indicated MEC organoid formation rates are dependent on the quantity of local cell numbers. Furthermore, bioprinting experiments designed to sequentially vary inter-organoid spacing indicated a time sensitive window of developmental plasticity; the resulting organoid geometry can be manipulated to match any desired geometry and size when initial cell-deposits were maintained within this spacing window. Lastly, we show accessible bioprinting techniques provide a reliable method to pattern multiple cell types inside 3D, *in vitro* cultures. This enabled a significant increase in the ability to reliably generate ‘chimeric’ cell organoids. Thus, bioprinting technology appears well suited to recreate the ‘contextual’ cues to further current research.

Here we show 3D bioprinting devices contain the capacity to reliably harness the remarkable affinity of living cells to spontaneously ‘self-organize’ into structures large enough for transplantation. As the power of any given scientific technology is rooted in the ability to reliably recreate experimental results, 3D bioprinting stands as an optimal technology to address the ‘big-data’ questions of many biological systems. Beginning with deciphering the microenvironmental variables present in the *in vivo* condition, bioprinting will illuminate the regulatory information for proper differentiation of cells, stem cell renewal, and eventually the development of complete tissues and organs.

## 1.2 Mammary Gland Formation

From the bumblebee bat to the blue whale, the mammary gland distinguishes mammals from all other animals. Beyond protocols of modern taxonomy, the tissue structure and function of the mammary gland are also unique because of the cyclical nature of the cell-cell and cell-extracellular matrix (ECM) interactions which also depend on the developmental stage and reproductive history of the mammal. For this reason, the mammary gland presents an optimal model system to study developmental biology. Studies of mammary gland development have presented valuable insights into the mechanisms regulating cell and tissue polarity, cell fate specification, branching morphogenesis, and the involution of a functional organ. Investigating these developmental programs are of interest to cancer biologists; many of the dysregulated pathways and processes observed throughout breast cancer progression mimic those observed during normal mammary gland development and tissue remodeling. However, the study of this system also stimulates a compelling desire to comprehend and solve the problem of breast cancer. Breast cancer affects 1 in 8 women in the United States. Thus, at one time or another, almost every family will have to deal with its consequences. We begin this overview by highlighting the different cell types that make up the mammary gland, with a specific focus on mammary gland ‘stem/progenitor cells’. We also discuss the external factors within the mammary gland microenvironment, which influence cell fate and function.

While rodent and human mammary glands have important structural variances, the mouse is a tractable, model organism, with well-researched methods and established protocols that have provided many insightful studies<sup>2</sup>. It is not surprising that much of our knowledge of mammary gland development, function, and tumorigenesis has emerged from investigations in the mouse. Both the human and rodent mammary gland are comprised of two types of epithelial cells: apically oriented luminal epithelial cells that line the ducts, and basally oriented myoepithelial cells. Luminal cells predominantly express keratins 8 and 18 (Ck8, Ck18), and are responsible for producing casein and other milk proteins. Myoepithelial cells predominantly express keratins 5 and 14 (Ck5, Ck14), as well as alpha smooth muscle actin which mediates their contractile function<sup>3</sup>. For this reason, myoepithelial cells are viewed as a hybrid of smooth muscle cells and epithelial cells because their contraction functions to cause secretion of milk during lactation<sup>4</sup>.

During embryogenesis, initial mammary development begins with the emergence of epithelial buds from ectoderm into mammary mesenchyme to form a rudimentary system of ducts, which continue a moderate rate of elongation after birth and with increases in body weight. Specifically, the first visible evidence of the mouse mammary gland is a subtle enlargement of the epidermis in the embryo on the E10 to E11. This single layered ectoderm enlarges to form the mammary lines, which extend from the anterior limb bud in the hindlimb to the posterior limb bud on the forelimb on both sides<sup>3</sup>. The individual mammary buds are formed as the epidermal cells in this band migrate to separate “centers of concentration” on the E12. The lens-shaped, multilayered, ectodermal structures called placodes then rise slightly above the surrounding ectoderm. The placodes then become bulbs of epithelial cells distinct from the surrounding epidermis. This separation event defines the future locations of the nipples and the accompanying mammary ducts. Mesenchymal cells around the bud condense and become the mammary mesenchyme. Between E12-16, the mammary rudiment maintains a slow growth. However, androgen receptor activation in the mesenchyme of male embryos between E13.5 and E15.5 signals for the degradation of the mammary buds<sup>3</sup>. On the other hand, female mammary gland development continues at E15.5, wherein the mammary rudiment starts to elongate by rapid cellular proliferation in the bud, leading to the formation of a sprout that invades the fat pad precursor<sup>3</sup>. Up until the last days of gestation, the mammary epithelium penetrates the prospective fat pad to create the branching trees of the early gland<sup>5</sup>. In fact, the mammary gland of the 19-day fetus contains the fundamental structures present in the adult virgin mammary gland<sup>6</sup>.

In rodents, the prepubertal mammary gland consists of long, infrequently branched ducts terminated by highly proliferative structures, called terminal end buds (TEBs)<sup>5,7</sup>. The TEB structures in the mammary gland are characterized by their strategic location at the tips of ducts. TEBs are comprised of two main compartments, a single, basally-positioned layer of cap-cells, which stays in contact with the thin layer of basal lamina and differentiate into myoepithelial cells as the duct elongates, and the inner compartment, consisting of a multi-cellular layer around 4-6 cells in thickness which form the bulk of the TEB known as the body-cell layer<sup>8</sup>. It is believed that the processes of ductal elongation and complex branching of the mammary gland originate in mammary stem cells located in the TEB<sup>9</sup>.

Considered the ‘engine’ of ductal elongation, TEBs penetrate and expand into the mammary fat pad and undergo regular bifurcation events to give rise to the tree-like pattern of the



primary mammary ductal tree<sup>10</sup>. This period of ductal expansion is the result of intensive mitotic activity in mammary TEBs<sup>11</sup>. Secondary and tertiary ducts sprout from primary ducts to form the characteristic ductal arborization observed in mature virgins. The bulbous, epithelial structures at the advancing edge of the TEB appear to be specialized to permit rapid penetration of the surrounding fatty stroma. The posterior regions of TEBs provide a supply of differentiating ductal and myoepithelial cells for elongation of subtending ducts<sup>12</sup>. Branching morphogenesis results from the collective advancement of luminal epithelial cells, whereas myoepithelial cells appear to restrain elongating ducts. Duct initiation requires proliferation, Rac, and myosin light-chain kinase, whereas repolarization to a bilayer depends on Rho kinase<sup>13</sup>. In addition to linear growth, mammary TEBs branch dichotomously at regular intervals, thereby generating the rudimentary patterning of the gland<sup>8,14</sup>. By turning to avoid competing tissue, they generate regular spacing between ductal elements. Once the TEBs near the edge of the fat pad, or when scarce gland-free stroma is available for continued growth, TEBs regress into blunt-ended, ductal termini, and their subtending ducts become mitotically inactive<sup>15</sup>. Importantly, these structures do not exhibit the high-degree of proliferation or the histological structures of active TEBs<sup>16</sup>.

Breast tissue morphogenesis in the adult organism is coupled to the periodicity of the mammalian reproductive cycle<sup>7,17,18</sup>. Throughout puberty and pregnancy, unique cell types are responsible for the mammary functions at each developmental phase<sup>19,20</sup>. However, branching morphogenetic processes dominate over those promoting differentiation or apoptosis during the estrous cycle, pregnancy and after parturition<sup>21</sup>. In contrast to the linear growth of ductal elongation, branching morphogenesis in pregnancy is followed by a radial growth and differentiation of ductal cells into lobular alveolar epithelium that produces milk after parturition. It should be noted that luminal cells of the duct also produce milk. After weaning, extensive ECM remodeling occurs concomitantly with tissue involution through the regulated apoptosis of lobular alveolar breast epithelium, and in the proliferation of adipocytes. This pattern of morphogenetic differentiation/involution is repeated throughout the reproductive life span of female mammals, and defines the cyclically regenerative capacity of normal adult breast tissue<sup>21</sup>. This process is currently thought to result from hierarchies of stem/progenitor cells within the luminal epithelial cell population and myoepithelial cells lining the ducts<sup>22</sup>. The regenerative ability of these cell types has been confirmed experimentally<sup>23</sup>. For example, when transplanted into cleared mammary

fat pads, these cell types can give rise to entire ‘clonally-derived’ mammary trees<sup>2,24,25</sup>. Thus the mammary gland epithelial compartment contains a mammary epithelial stem cell population<sup>24</sup>.

### *1.2.1 Dynamic Relationship Between Mammary Tissue Structure and Function*

The continuum of secreted factors that make up the acellular fraction of the 3D microenvironment is known as the ECM. The ECM is composed of diverse substances, from macromolecules like collagens, fibronectin, laminins, to polysaccharides such as hyaluronan, and glycosaminoglycan. BM, a form of specialized ECM, surrounds all epithelia. Aside from structural support, the BM forms a mechanical connection between epithelial layers and nearby connective tissue. The BM also prevents epithelial cells from invading the connective tissue, while also preventing the invasion of surrounding stromal cells into the BM compartment. Laminin, a trimeric protein, interacts with itself, other components of the ECM, and proteins on epithelial cells. As such, it is considered the primary organizer of the BM. Type IV collagen provides the tensile strength of the BM through a network of fibers. Nidogen and perlecan link the collagen network to laminin.

While numerous genomic and gene expression arrays can provide evidence of a cell’s status or identity, it is a fallacy to argue that genes alone determine and regulate the pattern of gene expression. It has been postulated that tissue-specific form and function are achieved by the dynamic interactions between the cell and its surrounding ECM. For example, normal organ architecture can act to suppress tumor growth, and prevent malignant phenotypes, despite gross genomic abnormalities<sup>26</sup>. As a result, we now understand that the microenvironmental structure of a tissue or organ is indispensable for its function.

Outside the cell, the ECM functions to maintain the appropriate integrity and strength of the cell network, and the type and amount of cellular connection to the ECM. Inside the cell, cell adhesions serve as anchoring points between cells, and between the cell cytoskeleton and the ECM. Important to our current understanding of ECM in cellular processes is the crosstalk among the individual ‘inside’ and ‘outside’ components within these systems<sup>27</sup>. For example, in response to the presence of laminin, MECs upregulate expression of several connexin gap junction (GJ) proteins, which leads to an enhancement of gap junctional intercellular communications (GJIC)<sup>28</sup>. Thus, components of the ECM can alter aspects of the cell-interior through ‘outside-in’ processes.

Conversely, the cell can secrete and remodel the ECM through ‘inside-out’ processes<sup>29</sup>. Specifically, the nuclear compartment of the cell interacts with the cytoskeletal compartment, which interacts with the membrane compartment, which interacts with the extracellular world. Importantly, instead of a two-way street, where each component is an isolated, one-way traffic flow, the influence of ‘outside-in’ and ‘inside-out’ processes on gene expression are better represented as a traffic circle where both components converge and intersect to influence global traffic flow. The overall process is a dynamic, cross-talk which connects ECM-ECM receptor interactions to the cytoskeleton, to the nuclear matrix, chromatin and back again<sup>1</sup>. This phenomena is commonly dubbed ‘dynamic reciprocity’<sup>30</sup>. Thus, instead of a simple scaffold to host cell growth, the ECM is now viewed as an integral determinant of tissue specificity itself.

### *1.2.2 Cell and Tissue Polarity*

Cells in all tissues and organs are asymmetrically organized. Likewise, the importance of proper maintenance of cell polarity in MECs is essential for their communication with the extracellular world, and the ability to produce and secrete milk proteins. Without correct polarity, fluids would not be transported to the appropriate compartments. Three different intercellular junction complexes function to create a polarized tissue: tight junctions, adherens junctions, and desmosomes<sup>31</sup>. These complexes hold epithelial cells together and attach cells to the BM. Tight junctions regulate the paracellular transport of ions and small molecules and serve to inhibit the mixing of proteins in the apical and basal compartments. Tight junctions are a network of strands that encircle the cell and interact with similar strands on neighboring cells, creating a seal around the cells. Intercellular tight junctions are stabilized by linkage to actin filaments. The two domains of MEC structures, the apical layer of luminal cells, and the basal myoepithelial cells, differ in protein and lipid composition, which is regulated by intercellular junctions and cytoskeletal organization. Even without myoepithelial cells, establishing apicobasal polarity and cell junctions can be achieved if cells are cultivated in the presence of exogenous BM components, such as Matrigel (Geltrex), or on a flexible collagen I gel. In the latter case, as cell-cell contact is increased, the cells generate and deposit endogenous BM and become functionally differentiated<sup>32</sup>.

### 1.2.3 Summary

The concept that cells are modulated by signals from their surrounding microenvironment is not new. How else can 10 trillion cells with the same genetic information make the numerous types of tissues, each with a different form and function? In tissues, multiple cell types serve distinct functions. The information presented here attempts to illustrate the fact that these functions are more dependent on the highly ordered, 3D geometrical context, than their individual genome. Also, as early as the 1960s, chimeric models using the stroma from one type of tissue co-cultured with epithelial cells from a different tissue have indicated the structure of an organ presents signaling information which is distinct from the genomic blueprint of the cell. Thus, a huge challenge for breast cancer research comes from the need to incorporate ‘context’ into research models.

## 1.3 The Use of 3D Culture Systems to Study Epithelial Biology

### 1.3.1 History of 3D Culture Systems

3D culture systems for generating organoid cultures of MECs inside collagen matrices were first introduced over four decades ago<sup>33-35</sup>. Standard 3D culture procedures involve either mixing dispersed MECs with ECM substrates prior to gelling (as described in Protocol 1), or by culturing cells on top of a pre-formed ECM gel. The encapsulated cells will then spontaneously ‘self-assemble’ into organoids. The initial stage of this process is characterized by the ability of the epithelial cells to detect and sense points of contact with ECM surfaces through integrins and dystroglycans, and points of contact with neighboring cells through cadherins and desmosomes<sup>36</sup>. The presence of these initial contacts spontaneously activates a series of cell remodeling events, which results in the polarization of cells, i.e. the formation of basolateral and apical surfaces with an asymmetric distribution of membrane proteins<sup>37</sup>. For the purposes of this and other 3D MEC investigations, the term ‘MEC organoid’ was operationally defined as cell growth and proliferation which resulted in the formation of semi-organized multicellular structures with polarized cells facing an open lumen<sup>31,34,36,38,39</sup>.

### 1.3.2 Effect of Parameters on Cell Behavior in 3D Culture

In 3D culture, multiple parameters operate together to affect both experimental outcomes and interpretation of experimental results. These parameters include cell type, cell-cell interactions, ECM composition, culture media, and an assortment of mechanical properties such as matrix stiffness and cell confinement (porosity)<sup>40-51</sup>. 3D culture models have highlighted the importance of matrix compliance for tissue-specific differentiation<sup>36</sup>. Matrix compliance differs dramatically between 2D and 3D cultures, and normal versus tumor tissues *in vivo*. The normal mammary gland has an elastic modulus of  $167 \pm 31$  (Pa), the average tumor  $4049 \pm 938$  (Pa), and 2D tissue culture plastic (polystyrene)  $2.78 \times 10^9$  (Pa)<sup>52</sup>. Therefore, it is not surprising that successful recapitulation of normal tissue morphogenesis is favored by matrix conditions with an elastic modulus that corresponds to normal tissues *in vivo*<sup>52</sup>. Indeed, cells invariably lose their differentiated phenotypes when grown on 2D tissue culture plastic<sup>33</sup>. However, these cells can regain their differentiated phenotypes if the microenvironment of the culture vessel is designed to mimic the cell's normal, *in vivo* microenvironment<sup>1</sup>. Also, it is widely acknowledged that sources of ECM for 3D cell culture, such as collagen isolated from animal tissues and/or laminin rich extracellular matrix such as Matrigel, are subject to lot-to-lot variability, which has the potential to introduce experimental irregularities in the mechanical properties of 3D cell culture systems<sup>53</sup>. However, Matrigel or collagen can be modified by adjusting the gel thickness, gelling temperature, and concentration.

Recent investigations of mammary ductal morphogenesis indicate collagen fiber density, diameter, and alignment play a key role in determining the shape of *in vitro* cultures of mammary epithelium<sup>54,55</sup>. Upon encapsulation, mammary cells cultured in collagen gels extend processes to 'sense' and reorganize the surrounding meshwork for considerable distances (10-100 $\mu$ m) before pseudopod stabilization and mechanical interaction<sup>54</sup>. Following stable adhesion formation to ECM components, the mechanical interaction between individual cells and ECM results in the transmission of strain patterns which can extend through hundreds of microns of gel<sup>56-58</sup>. This applied mechanical strain leads collagen fibers to orient along the direction of the strain, which results in increased contact guidance<sup>59</sup>. This may explain why early studies found a preference for breast epithelial organoids to develop along tension lines between adjacent organoids within collagen gels<sup>60</sup>. Through what appears to be a positive feedback loop, a small alignment of fibers,

cells, tension, or the resistance to tension can be amplified into a robust, parallel orientation of cells and fibers<sup>54</sup>. Together, these findings suggest the developmental cues that define tissue form and function are derived from physical properties within the surrounding microenvironment and are rarely cell intrinsic. Delineating the role of these organizational features in tissue morphogenesis will lead to a better understanding of the coordinated cellular behaviors responsible for normal tissue formation across local and global spatial scales.

Numerous examples have reported the considerable influence of physical parameters on tissue morphology in 3D cultures. Early work using primary mammary epithelial cells showed that cells plated on plastic or embedded in collagen gels that remain attached to the culture plate, lose the fully differentiated phenotype, along with the ability to produce the milk protein  $\beta$ -casein. However, cells could be induced to make  $\beta$ -casein if the collagen gel was initially detached from the culture dish, known as a ‘floating’ collagen gel<sup>32,33</sup>. Additionally,  $\beta$ -casein production could be rescued in cells embedded in attached gels, if the gels were detached (floated) from the culture surface<sup>33</sup>. Epithelial cell differentiation is not limited to floating gels; differentiated alveolar and ductal structures were found in collagen gels cast in thin-plastic inserts with a porous, flexible membrane bottom<sup>61</sup>. However, the MEC organoid phenotypes from this method were reported to be associated with distinct locations of the collagen gel, which may be related to minute variances in collagen matrix elasticity between the center and periphery of the gel<sup>59,61</sup>. The ability of physical parameters of 3D cultures to influence cellular differentiation has also been supported by experimental evidence linking attached collagen gels to a significant increase in Ki67, a marker of proliferation, when compared to cells in a floating gel of the same density<sup>62</sup>. Thus, the control of epithelial structures cannot be attributed to matrix composition alone.

The ability of MECs to successfully differentiate appears to depend on their ability to contract the collagen gel. ROCK-mediated contractility diminished RHO activity in a floating 3D collagen gel and corresponded to a loss of FAK phosphorylated at Y397 localized to 3D matrix adhesions<sup>62</sup>. Further, when cells are cultured in high-concentration, floating collagen gels, Rho activity remains high, FAK phosphorylation is promoted, and differentiation/organoid formation is disrupted. These data suggest that increased ECM rigidity increases Rho activity which promotes epithelial proliferation, motility, and alters focal adhesion formation, all of which lead to a loss of the functional, differentiated organization required for proper organoid formation<sup>62</sup>. Together, these data suggest that the physical forces, such as the fibrillar organization of collagen

fiber reorganization, and the external influences of cell culture conditions can influence the development and maintenance of structural and functional differentiation of normal mammary epithelia.

### 1.3.3 Summary

The development and remodeling of the mammary gland is dependent on dynamic molecular, and mechanical pathways. Importantly, tissue architecture itself is a key component of the regulatory mechanisms that dictate cell growth and function<sup>35,63</sup>. To accurately recreate the *in vivo* environment, every individual component of *in vitro* models must be tuned for the system under study. The development of cancer is characterized by a loss of tissue architecture, loss of differentiation, and dysregulation of growth control, all of which result in the invasive and proliferative phenotype. Similarly, when the spatiotemporal coordination between extracellular cues and intracellular processes is disturbed, normal cellular behavior becomes deregulated, which often leads to malignant transformations. Therefore, *in vitro*, 3D models must accurately reflect the local microenvironment and cellular behaviors in normal tissues.

## 1.4 Bioprinting Platforms in Biological Research

### 1.4.1 3D Bioprinting

3D bioprinting has gained recent attention as an investigative tool to alleviate some of the experimental inconsistencies and limitations frequently associated with manual methods of 3D cell culture<sup>64</sup>. The use of CAD technology to fabricate complex organs and materials of biological origin defines the core goal behind bioprinting technology. Current bio dispensing processes in 3D biofabrication utilize inkjet, microextrusion and laser-assisted printing<sup>65</sup>. However, commercially available bioprinting devices are not readily optimized for the unique research demands of individual labs, which have limited their widespread adoption into routine assays and procedures.

The greatest features when considering different bioprinting technologies are the print resolution, materials used during the printing process, the cell signaling pathways affected by the printing process, and the culture methods used. While inkjet and laser-based transfer are well suited to manipulate picoliter to nanoliter droplets at microscale resolution, they are not simple to use or maintain. For example, inkjet deposition techniques typically employ thermal or piezoelectric actuators. The nozzles in these actuators are cylindrically shaped with diameters around 50 $\mu$ m. It is also the case that traditional inkjet printers are only capable of printing liquids. That is to say, to form solid 3D structures, the printed liquid must be crosslinked after deposition. Crosslinking adds additional environmental stresses to the conditions that the cells must endure (pH changes, temperature changes etc.)<sup>66</sup>. Numerous variables must be controlled to maintain the high resolution of laser-based printers. These factors include the surface tension and wettability of the substrate, in addition to the air gap between the prepared solution and the collector substrate<sup>67</sup>. Additionally, each donor transport support or ‘ribbon’ must be prepared for each printed cell or hydrogel type. This equates to a time-consuming, preparatory sequence that is not ideal for routine experimentation in most research labs.

#### *1.4.2 Adapting Bioprinters to Meet Specific Research Demands*

Tissue engineering research requires custom materials and tailor-made fabrication methods, which are not easily addressed in closed-source systems. The bioprinting device and associated protocols described here were designed, manufactured, and tested to investigate our unique requirements to generate controlled-arrays of cells in 3D environments. This process involved investigating the potential use of ‘off-the-shelf’ 3D manufacturing systems for routine 3D cell culture. First, the need to extrude microscopic sized particles through a small orifice is not just a problem for biologists using 3D bioprinters, but also for all living cells in cell-based printing. For this reason, the duration and amount of mechanical forces experienced by cells should be minimized during flow.

Second, if the specified tolerance among the parts is appropriately maintained within a set standard, extrusion-based printing technologies can achieve resolutions way beyond that of routine, handheld pipetting. Ensuring the intended amount gets to the intended spatial region of the construct is paramount. For obvious reasons, these are intimately related to advances in



manufacturing technologies used in 3D printing devices. However, they are also related to matching the machine parameters to the desired experimental scale. That is to say, if a 50 ml syringe and a 1 ml syringe were placed on identical extrusion-based bioprinters, and both given an identical travel distance in the linear actuator located on the extrusion head, a greater amount of material will be extruded from the 50 ml syringe. Thus, the performance of extrusion-based systems is intimately related to the size and volume of material inside the syringe.

Third, common 3D bioprinting operations fabricate tissue constructs using a layer-by-layer process. Yet, because they are mostly water, when gel components come out of a printer nozzle they do not always stay in their specified location. This severely limits the spatial resolution of cell-deposits in 3D constructs due to the inability to accurately control the location of cells during gel polymerization. Furthermore, the rheological properties of any given substrate can affect printing operation. For example, shearing effects during the deposition process can impart destructive forces on the structural integrity of gel components.

The physical properties of a substrate can also affect printability. For example, many 3D MEC cultures employ collagen or other mesh-forming materials as a primary scaffold. Yet, fibrous materials spontaneously ‘self-assemble’ to form aggregates, including those which function *in vivo* to form a plug, like the role of fibronectin and fibrin to prevent further blood loss during wound healing. Thus, it would only take a few collagen aggregates to occlude the narrow tip of a 10 $\mu$ m nozzle. Additionally, reliably patterning cells suspended inside highly-viscous ‘ink’ would require more extrusion force than extruding cells suspended in liquid cell-culture ‘media’.

Some of the limitations of layer-by-layer manufacturing could be overcome if bioprinting operation were able to insert cells into a pre-formed, bio-scaffold that contained some self-healing properties. Using this method, one could easily see how layer-by-layer bioprinting operations could be complemented with a high-resolution injection device<sup>68,69</sup>.

### 1.4.3 Importance of the Tissue Microenvironment

Despite significant increases and improvements in cancer research, nearly 95% of oncology drugs in clinical trials fail to receive Food and Drug Administration approval<sup>70</sup>. Additionally, despite the availability of potent chemotherapeutics against a wide variety of cancer types, some patients never achieve a long-lasting cure. The complete therapeutic elimination of tumor cells remains complicated due to the phenomena of tumor heterogeneity<sup>71,72</sup>. Part of this issue stems from the inability of preclinical models to accurately recapitulate the complexity of the disease state. These complexities originate from cancer cell-intrinsic signaling/cross talk, extrinsic interactions with other cell types, and multiple components of the tumor microenvironment<sup>73</sup>. In addition, the dynamic regulatory networks generated within these diverse cell populations are also influenced by unique zones within the tumor environment, each with various physical and chemical parameters<sup>71,74-76</sup>.

Thus, in addition to matching matrix stiffness to comply with *in vivo* conditions, the maintenance and differentiation of the numerous mammary gland cell types is also dependent on the properties and features of the local tissue microenvironment. Biological phenomena observed during development require interactions among different components of a tissue; and the clear majority of these are seldom explained without addressing the contextual cues from the tissue-level to the cell-level of organization<sup>77,78</sup>. Therefore, while they are generally informative, *in vivo* xenotransplantation assays of human cancers, and monoculture models of 3D tumor biology, such as tumor spheroids and tumor organoids, are incapable of incorporating the microenvironmental cues associated with the human cancer ecosystem.

Ohne musik wäre das Leben ein Irrtum.

Friedrich Nietzsche

## CHAPTER 2

### DESIGN RATIONALE, DEVELOPMENT, AND UTILIZATION OF A 3D BIOPRINTING DEVICE

#### 2.1 Overview

The precision and repeatability offered by computer-aided design and computer-numerically controlled techniques in biofabrication processes is quickly becoming an industry standard. However, many hurdles still exist before these techniques can be used in research laboratories for cellular and molecular biology applications. To circumvent the high-price barrier to entry of conventional bioprinters, 3D printed components were created for the adaptation of an 'off-the-shelf' 3D printer. Extrusion-based bioprinting systems have been characterized by high development costs, injector clogging, difficulty achieving small cell number deposits, decreased cell viability, and altered cell function post-printing. To address these performance limitations, several microneedle geometries were developed to optimize 'bio-ink' flow. Goal-based, computer simulations indicated the needle geometries of conventional, commercially standardized, 'luer-lock' syringe-needle systems cause many of the resolution issues plaguing conventional bioprinters. Among these, a short-tapered injector design with minimal cylindrical needle length was ideal to minimize cell strain and accretion. These geometries were experimentally quantified using pulled glass microcapillary pipettes and the modified, low-cost 3D printer.

This systems performance validated computer-simulation models exhibiting: reduced clogging, single cell print resolution, and maintenance of cell viability without the use of a sacrificial vehicle. This system maintained the pluripotency of human induced pluripotent stem cells (hiPSCs) 7 days post-printing in Geltrex. We also show embryoid body differentiation of hiPSC by injection into differentiation-conducive environments, wherein we observed continuous

growth, emergence of various evaginations, and post-printing gene expression indicative of the presence of all three germ layers. These data demonstrate the benefits of using accessible, open-sourced, 3D bioprinters to serve the individual needs of any laboratory interested in 3D cellular interactions and tissue engineering.

## 2.2 Introduction

Bioprinting enables the high-precision, high-accuracy, and high-throughput generation of biological constructs that can contain: ECM scaffolds, cells, and biochemical factors in 3D. Due to these advantages, bioprinters hold the promise of establishing culture conditions that more closely mimic the human *in vivo* microenvironment than animal models, and current 2D cell culture environments<sup>79,80</sup>. Specifically, great progress has been made in the field of tissue engineering and regenerative medicine due to the emergence of a wide range of 3D multifunctional devices which employ extrusion-based technologies to further the development of advanced materials that require proper pre/post-processing for the fabrication of 3D structures<sup>81-84</sup>. While capable of generating high-throughput experimental designs to answer difficult biological questions, the technology has remained inaccessible to most research labs due to the initial investment and routine, operational costs. Furthermore, the design and implementation of custom-built 3D bioprinters yields high lab-to-lab variability resulting in unpredictable experimental outcomes, generating some unease surrounding their implementation.

The dominant techniques in microextrusion bioprinting use valve-based pneumatic or gear-driven actuator extrusion systems to drive cell suspensions out of a micro-needle tip. Numerous studies have noted needle diameters under 150 $\mu$ m are not ideal because they are prone to frequent needle clogging<sup>85,86</sup>. Naturally, the print resolutions of these systems are largely dependent on the diameter and flow rate at the needle tip. Therefore, despite having highly accurate/precise single- $\mu$ m positioning features, the majority of microextrusion bioprinters are limited to 150 $\mu$ m wide print resolutions. In addition to clogging, previous reports indicate process-induced damage can lead to a significant source of cell death and unexpected post-printing phenotypes<sup>87-93</sup>. Therefore, any design that alleviates clogging and process-induced damage, while simultaneously increasing print resolution to the sub-150 $\mu$ m level, would be highly advantageous.

Furthermore, the impact of these systems on more sensitive cell types has been understudied. One extremely promising cell type prone to defects upon physical manipulation is the induced pluripotent stem cell (iPSC). iPSCs are advantageous in both disease modeling and tissue engineering as they have the ability to self-renew indefinitely or differentiate into any cell type of all three germ layers<sup>94</sup>. A significant challenge for the implementation of iPSCs into bioprinting is the multivariate nature of the differentiation process. When culture conditions permit differentiation, iPSC clumps will initially form spheroids, which then differentiate into embryoid bodies (EBs) that resemble early stages of embryogenesis. It has been shown that the initial size of the EB aggregate is a critical factor in controlling differentiation<sup>95</sup>. However, few existing technologies are capable of reliably controlling the quantity of individual cells in a target location, and the overwhelming majority of current investigations rely on handheld pipetting. Additionally, mechanically induced stem cell differentiation has been attained through application of mechanical forces including stretch, strain, compression, and shear stress<sup>96</sup>. This awareness has led to the development of methods to encapsulate cells through the use of hydrogel-vehicle systems to alter the distribution of damaging mechanical forces experienced during flow. Yet, recent studies indicate these systems do not offer complete protection from damaging forces, and cell-vehicle interactions could ultimately lead to unwanted cell-fate determination post-printing<sup>66,97</sup>. Therefore, the successful use of iPSCs requires biofabrication techniques that not only minimize harmful forces and exposure to stress, but also concurrently select the appropriate culture conditions to achieve the desired, differentiated cellular product.

Here we demonstrate the adaptation of a commercially available, 'off the shelf' extrusion-based, 3D printer (Felix 3.0) into a functional, high-resolution, extrusion based bioprinter/bioplotted. Furthermore, we report a goal-based, computational modeling approach to optimize the biofabrication of high resolution, fragile cell transfer without the use of encapsulating hydrogels to maintain the pluripotency of printed hiPSCs. We experimentally quantified the functional limitations of micro-extrusion based bioprinting by exploring relationships among parameters such as micro-needle geometry, infusion flow rate, printed cell resolution, cell viability and the retention of a functional differentiation capacity. We show via both finite element method (FEM) and physical cell-extrusion bioprinting experiments that the use of deposition systems with a sharp reduction in inlet diameter coupled to a long, narrow microneedle (such as those found in 'luer-lock' syringe systems) generate greater amounts of detrimental forces than those with a gently

tapered, conical needle geometry. We also demonstrate the ability of our system to print sensitive hiPSCs without affecting their pluripotency. With new maker movements taking hold<sup>98</sup>, the use of printable components for accessible bioprinting holds the possibility of making truly transparent, and transportable scientific advancements in this field a reality. By lowering the barrier of entry for these complex tools, research in laboratories across the world will be able to design studies to not only improve the engineering of tissues, but also improve the *in vitro* study of biological processes such as development and tumorigenesis.

## 2.3 Materials and Methods

### 2.3.1 Cell Culture

Green fluorescent protein (GFP) labeled rat epithelial cells and GFP labeled MDA-MB-468 mammary epithelial cells were cultured in a 75 cm<sup>2</sup> flask in a mixture of Dulbecco's modified Eagle's medium and Ham's F12 medium (DMEM/F12), 10% FBS and 1% ABAM (ThermoFisher). MCF-12A cells were purchased from ATCC and cultured in 75 cm<sup>2</sup> flask in DMEM/F12, supplemented with 20 ng ml<sup>-1</sup> hEGF, 0.01 mg ml<sup>-1</sup> bovine insulin, 500 ng ml<sup>-1</sup> hydrocortisone, 5% Horse Serum, 0.01 mg ml<sup>-1</sup> bovine insulin and 1% ABAM. Established human induced pluripotent stem cells lines (hiPSC) were generated from BJ fibroblasts through sendai virus reprogramming<sup>99</sup> and cultured on Geltrex matrix (ThermoFisher) with Essential 8 medium (ThermoFisher) and passaged manually with a pulled glass 'knife' to avoid culture induced genomic instability. All cells were cultured at 37.0 °C, and 5.0% CO<sub>2</sub>.

### 2.3.2 Bioprinting System

We have developed a microextrusion based bioprinting system that is capable of extruding biopolymer solutions and living cells for freeform construction of 3D tissue scaffolds. This was achieved by modifying a consumer-based 3D printer, Felix 3.0 (FELIXrobotics, NL). The machine has listed print resolutions of 13μm, 13μm, and 0.39μm for the *x*, *y*, and *z* axes, respectively. All

3D printed components of the deposition system were designed in-house using Solidworks CAD software and printed in PLA or ABS using the 3D printer. The deposition apparatus, designed to replace the plastic-extruding print head, mounts to the stock printer's x-axis mounting bracket. The apparatus is capable of housing a variety of tools through a library of part specific, 3D printed inserts. The system is powered by a NEMA 17 hybrid bipolar stepping motor with an integrated threaded rod (Pololu, USA, item no. 2268). The traveling nut moved  $40\mu\text{m}$  per full step. The stepper motor has a  $1.8^\circ$  step angle (200 steps/revolution) and each phase draws 1.7 A at 2.8 V, allowing for a holding torque of 3.7 kg cm (51 oz-in). Therefore, 1 revolution equaled  $8000\mu\text{m}$  of linear travel. The Felix 3.0's motor driver is capable of using 1/16th microstepping routines, which provided resolutions of 2.5nl. The internal backlash of the motor is  $\leq 3^\circ$ . An 8mm Simplicity® linear plain bearing (PCB Linear) and an 8-mm stainless steel rod (McMaster Car) provide support during linear displacements. Experiments were defined by user inputs in a custom Python and Matlab graphical user interface. The software allows the user to manually or automatically populate the wells of a specific plate with specific droplet properties in 3D. The program would also correct user operations that would place the needle tip outside the boundaries of the available print areas. The plotting locations and printing information was automatically converted into g-code, loaded into the open-sourced 3D printer controller Repetier Host, v.1.0 and sent to the three-axis microcontroller.

### *2.3.3 Computational Modeling*

To quantify the relationship between fluid flows as a function of microneedle geometry, idealized needle geometry profiles were created in Solidworks Flow Simulation (Dassault Systems, FR) and Comsol Multiphysics. A goal-driven, computational analysis was solved iteratively until flow parameters converged to a certain solution/goal. The flow simulation utilized solution-adaptive mesh refinement by splitting the mesh cells in the high-gradient flow regions and merging cells in the low-gradient flow regions. The mesh was set to provide advanced, narrow-channel refinement and optimized thin wall resolutions. The model was given conditions of steady, non-Newtonian flow. The fluid used in our experiments was given properties similar to blood. Three classes of needle geometries were created representative of the cylindrical needle geometry seen in stainless steel 'luer-lock' needles, a straight sided cone, or tapered profiles modeled as

hyperbolas, parabolas or ellipses in a similar manner to those seen in Martanto *et al.*<sup>100</sup>. The inlet diameter for all needle conditions equaled 1mm. The inlet volume boundary condition was based on a constant volumetric flow rate of  $0.1\text{mm}^3\text{ s}^{-1}$  ( $0.1\ \mu\text{l s}^{-1}$ ). The diameter of the flow outlet for all simulated conditions equaled  $60\mu\text{m}$ . The flow outlet boundary condition was set to standard atmospheric pressure, (101325 Pa). Our model conditions accounted for the effects of gravity on cell settling during needle inversion. We were able to specify wall conditions by specifying values for accretion rates and the normal and tangential coefficient of restitution. The model features from three idealized needle geometries that met our goal criteria (minimum shear rate, pressure, and needle diameter while maximizing flow rates) were then fabricated using a Sutter P97 programmable pipette puller and experimentally quantified using our 3D printed, 3D bioprinter. An optical encoder provided measurement scales to confirm needle profiles by visual analysis using Matlab and ImageJ.

#### 2.3.4 Cell Viability Assay

MCF-12A cells were suspended in media to a concentration of  $1 \times 10^6$  cells  $\text{ml}^{-1}$ . For all conditions, approximately  $25\mu\text{l}$  of media was loaded into the needle at a rate of  $10\ \mu\text{l min}^{-1}$  and dispensed into wells of a 96 well plate at one of four rates: 100, 400, 600, and  $1000\ \mu\text{l min}^{-1}$ . All four rates were repeated in three separate wells for a total of 12 wells per condition. Four needle conditions; no-tip (control), 28-gauge needle, straight cone, and long tapered needle were tested, giving a total of 48 wells. Post-printing, cells were maintained in a laboratory incubator at  $37.0\ ^\circ\text{C}$ , 5.0%  $\text{CO}_2$ . Viability was assessed 1 and 96 hours post-printing with AlamarBlue (ThermoFisher) by measuring absorbance at 570 nm on a UV–Vis spectrophotometer with SoftMax Pro 6.3. The sample mean viability was calculated and normalized to the initial viability of the no-tip control. Statistical significance was determined using one-way ANOVA with Dunnett's post hoc test ( $p < 0.05$ ). Error bars on all figures represent the standard deviation of the sample mean.



### 2.3.5 hiPSC Bioprinting and TRA-1-81 Staining of hiPSCs

Twenty-four hours prior to printing, 50 $\mu$ l of a 1:1 mixture of growth factor reduced Geltrex and differentiation suppressive media (Essential 8) was added to 12 wells of a standard 96 well plate and stored in a laboratory incubator at 37.0 °C, 5.0% CO<sub>2</sub>. Before cell plotting, the plate was removed from the incubator and placed on the heated print bed (37.0 °C). Single cell suspensions of hiPSCs were obtained by rinsing pre-established, hiPSC containing wells with DMEM, followed by a 5-min incubation with Accutase (Sigma-Aldrich). Cells were then centrifuged at 300 x g for 3 min; and the resulting pellet was diluted with essential 8 media to a concentration of 4.5  $\times$  10<sup>6</sup> cells per ml. Single cell suspensions of hiPSCs were then loaded into a pulled glass needle with a 40 $\mu$ m tip diameter at 10  $\mu$ l min<sup>-1</sup>. The plotting routine was set to dispense a number of 100nl droplets 200 $\mu$ m (*X*, *Y*) apart and 250 $\mu$ m (*Z*) from the bottom of the plate. Post-printing, 150 $\mu$ l of essential 8 media was overlaid on the gel, and the plate was incubated at 37.0 °C, 5.0% CO<sub>2</sub> for 7 days. The overlaid media was changed every 24 hours for 7 days. After 7 days in culture, StainAlive TRA-1-81 antibody (Stemgent) was diluted to a concentration of 5  $\mu$ g ml<sup>-1</sup> in fresh cell culture medium. The antibody containing media was added to the wells containing hiPSC printed aggregates and incubated for 30 min in a laboratory incubator at 37.0 °C, 5.0% CO<sub>2</sub>. The medium was aspirated, and the wells were gently washed two times with cell culture medium. Fresh cell culture medium was added to the wells and staining was examined using a Zeiss axio-observer Z1 fluorescent microscope.

### 2.3.6 Automated Formation hiPSCs Aggregates

Twenty-four hours prior to printing, 50 $\mu$ l of a 1:1 mixture of growth factor reduced Geltrex and differentiation supportive media (10% FBS, 1% ABAM, DMEM/F12) was added to 12 wells of a standard 96 well plate and stored in a laboratory incubator at 37.0 °C, 5.0% CO<sub>2</sub>. Before cell plotting, the plate was removed from the incubator and placed on the heated print bed (37.0 °C). Single cell suspensions of hiPSCs were obtained by rinsing hiPSC containing wells with DMEM, followed by a 5-min incubation with Accutase (Sigma-Aldrich). Cells were then centrifuged at 300 x g for 3 min; the resulting pellet was diluted with differentiation-supportive media to a concentration of  $4.5 \times 10^6$  cells per ml. These single cell suspensions of hiPSCs were then loaded into a pulled glass needle with a 40 $\mu$ m tip diameter at 10  $\mu$ l min<sup>-1</sup>. The plotting routine was set to dispense a number of 100nl droplets 200 $\mu$ m (*X, Y*) apart and 250 $\mu$ m (*Z*) from the plate bottom into wells of a 96 well plate containing 50 $\mu$ l of a 1:1 mixture of growth factor reduced Geltrex and differentiation supportive media. Immediately following the plotting routine, the plate containing fabricated hiPSC aggregates was incubated at 37.0 °C, 5.0% CO<sub>2</sub> for 7 days. 150  $\mu$ l of differentiation supportive media was overlaid on the gel post-printing and changed every 24 hours for 7 days. Post-plotting, wells containing gel-embedded hiPSC aggregates were monitored using brightfield imaging every 30 min for 5 days using a Lumascope 620 microscope.

### 2.3.7 Formation of hiPSC EBs Using Hanging Drop Method

The hiPSC single cell suspension used in the automated plotting experiment was diluted to  $5 \times 10^5$  cells ml<sup>-1</sup>. 1  $\mu$ l samples of the diluted hiPSC single cell suspension were then manually added to 20  $\mu$ l of differentiation-supportive media which had been previously pipetted onto the inside surface of a Petri dish lid. The lid was then inverted to force cells to aggregate due to the effect of gravity. The dish bottom was filled with the same media to prevent drying and stored in a laboratory incubator for 7 days at 37.0 C, 5.0% CO<sub>2</sub>.

### 2.3.8 Gene Expression Assay of Printed and Hanging Drop hiPSC Aggregates

Total cellular RNA was isolated from 7 day old, 3D printed hiPSC aggregates and hanging drop hiPSC EBs with Trizol (Life-Technologies) according to manufacturer's protocol. RNA quantification was determined by UV absorbance at 260 nm (A<sub>260</sub> nm) on a NanoDrop 2000 (Thermo Scientific). 5 µg of each RNA sample was reverse transcribed into cDNA using the High-Capacity cDNA Reverse Transcription Kit (Thermo Fisher) according to manufacturer's instructions. cDNA samples from established hiPSCs (control), printed hiPSCs and hanging drop EBs were amplified and detected using TaqMan Gene Expression Assays for markers, HAND1 (Hs02330376\_s1), SOX17 (Hs00751752\_s1), PAX3 (Hs00240950\_m1), NANOG (Hs04260366\_g1), and the endogenous housekeeping gene ACTB (Hs99999903\_m1). Quantitative Reverse Transcription PCR experiments were conducted with a StepOnePlus Real-Time PCR System (Applied Biosystems). TaqMan Fast Advanced Master Mix was used in conjunction with TaqMan Gene Expression assays per manufacturer's protocol. All experimental reactions were completed in triplicate and the relative quantity was calculated using the  $2^{-(\Delta\Delta ct)}$  method. All statistical comparisons were made with ANOVA (\* $p < 0.01$ ).

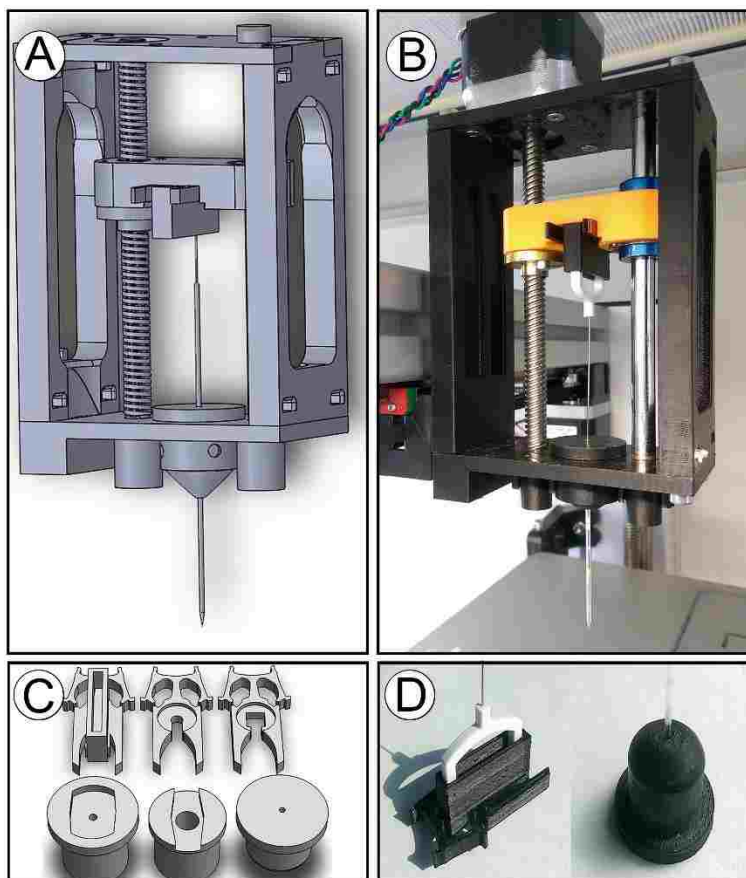


Fig. 1. CAD design and 3D printing of bioprinter modifications to the Felix 3.0. (a) CAD model of x-axis bioprinting adapter with lead screw and syringe adapter for injector depression. (b) Resultant 3D-printed bioprinter injector adaptor mounted to the X-axis of 3D printer with stepper motor installed for injector actuation. (c) CAD models for syringe adapter inserts for securing the body of the injector (bottom row) and clips for holding the plunger (top row). (d) Example of a 3D printed insert and clip used with the pulled glass-microcapillary pipette injector and teflon plunger.

## 2.4 Results

### 2.4.1 Bioprinter Fabrication

Most well-appointed commercial 3D bioprinters cost well above the budget limits of many biological laboratories wishing to use these tools for cell-based experimentation. To address this, we aimed to use readily available parts to adapt an 'off the shelf' extrusion-based, 3D printer into a high-precision, open-sourced bioprinter. The unmodified Felix has a positional resolution within a reasonable range for single cell deposition. We used CAD software to design a microextrusion apparatus to replace the plastic extruding print head, (Fig. 1a). These prototype parts were then 3D printed using the standard extrusion system on the unmodified Felix system, (Fig. 1b). To better serve our experimental requirements, the system was designed to be interchangeable with more than one type of plunger-driven syringe system (several sizes of luer-lock syringe, microcapillary pipettes, etc.), (Fig. 1c). Our 3D printed parts were highly accurate with regard to matching specified part dimensions (Fig. 1d). Furthermore, no measurable differences among printed components were observed confirming the Felix's stated precision and accuracy. Additionally, we are not aware of any other current bioprinting systems that have the capability to be utilized as both a bioprinter and a standard 3D printing system. As such, this is the first report of a device with these properties.

Needle type	Avg. pressure (kPa)	Max. pressure (kPa)	Avg. velocity (mm s <sup>-1</sup> )	Max. velocity (mm s <sup>-1</sup> )	Applied force (N)
7.0 mm T <sup>a</sup>	107.679	107.712	17.109	719.010	0.001 017 152
7.0 mm C <sup>b</sup>	103.505	103.526	15.339	711.593	0.000 352 58
1.0 mm T <sup>a</sup>	103.109	103.124	17.569	1271.699	0.000 283 929
1.0 mm C <sup>b</sup>	102.862	102.870	11.146	1249.325	0.000 139 728
0.75 mm T <sup>a</sup>	102.200	102.227	17.176	837.077	0.000 139 728
0.75 mm C <sup>b</sup>	101.683	101.691	11.157	746.944	0.000 056 1757

<sup>a</sup> Needle tips with a straight-sided, triangular appearance.

<sup>b</sup> Needle tips with curved geometries.

Table 1: Analytical solutions to CFD simulations of the bioprinting process using various microneedle geometries. Needle tips with a straight-sided, triangular appearance are labeled T. Needle tips with curved geometries are labeled C. Simulations were given conditions of steady, non-Newtonian flow of a constant mass flow of  $6 \times 10^{-5}$  kg/s. The inlet and exit diameter for all needle conditions equaled 1 mm and  $60 \mu\text{m}$ , respectively. The flow outlet boundary condition equaled standard atmospheric pressure, (101325 Pa). Numerical results indicated increasing needle length results in an increase in both total pressure and required force across all conditions. Results also indicated T needle types generate more internal pressure than C needle types of the same length. The average velocity for all T needle types was greater than C needle types. The maximum velocity was highest in the 1 mm long T needle type. Interestingly this needle type represents a 1:1 geometry near that of a straight-sided cone.

### 2.4.2 Needle Optimization Through Computational Modeling

As we intended to use our 3D bioprinter to print liquids containing both biomolecules and sensitive cell types, we recognized the need to model various needle variants to determine the flow characteristics, including shear rates in the needle tip. To do this, we designed several permutations of needle types using 3D CAD software. The needle types of our initial simulations included a model of a conventional, syringe-needle system, and needles with various lengths and internal slopes with a straight-sided triangular, T, or parabolic curved, C, geometry. The straight triangular needle is characterized by having a linear change in needle diameter, whereas the curved needle types resemble more of a parabolic curve with a slope that is greater than one<sup>100</sup>. We then measured the impact of needle geometry on fluid dynamics during the bioprinting process using computer generated, multiphysics simulations. To provide a better understanding of needle clogging due to cell accretion, we traced particle streamlines of 10 $\mu$ m wide particles, the typical diameter of cells, through our needle models under conditions that favored aggregation. The aggregation of cells within the needle tip occurred by increasing particle accretion rates and lowering the normal and tangential coefficients of restitution at the needle wall. Particle studies then indicated a large population of cells with velocities near zero in the narrowest region of the conventional needle configuration, (Fig. 2a). These populations were not observed in triangular needle configurations, (Fig. 2b). This indicated the conventional needle type leads to a higher rate of cell aggregation and needle clogging when compared to a tapered, triangular needle. Furthermore, the results from the flow simulations also indicated cells traveling through the center of the conventional configuration have a higher velocity than those in the center of the straight triangular configuration, 75 mm s<sup>-1</sup> versus 55 mm s<sup>-1</sup>, respectively.

The velocity profile established in a given flow situation strongly influences the mass transfer process. For our method of bioprinting, the mass transfer process is primarily dependent on the ability of the ejected droplet to remain inside the surrounding material. Furthermore, the needle tip should also impart minimal damage to the gel during the plotting procedures. Therefore, the best needle type should be narrow enough to penetrate the gel without disturbing surrounding material, limit unfavorable processing conditions for fragile cell types, and perform the printing process without clogging. To examine this concept a comparison between triangular, T, and curved, C, needles of increasing length was performed. The resulting data indicated all T type

needles have a higher average velocity than C type needles. Interestingly, we found the maximum velocity was greatest in the 1mm long needle type (Table 1). Yet, the 1 mm long T type requires lower force and results in a lower maximum pressure than both 7 mm long needle types. Given the inlet diameter for these simulations equaled 1 mm, the 1 mm long straight needle represents a 1:1 geometry near that of a straight-sided cone. We also found conically shaped needles generate less internal pressure than straight-sided triangular needles of the same length. Numerical results indicate needle length has a significant effect on total pressure. Interestingly, the 7 mm C needle type, showed a sharp reduction in total pressure when compared to a straight-triangular needle type of the same length, 7 mm T. We found this relationship to suggest needle length and needle type has an effect on total pressure. While longer needle lengths resulted in higher total pressures, the C type needles were always lower in total pressure than the straight-triangular type of the same length. Overall, the results show that as the cross-sectional area of the microneedle decreases, the maximum fluid velocity increases and the pressure decrease.

Results from our flow simulations also found the shear rate generated in conventional systems is greater than shear rates observed in needles with tapered geometries. These simulations suggest, as the extent and shape of the flow passages change, the cells within the fluids are subjected to stretching in one or more dimensions. It should be noted the shear rate in the conventional system was highest in the region immediately after the abrupt reduction in needle diameter, and also in the region nearest the needle tip, suggestive of elongational flow, (Fig. 3a). On the other hand, the shear rate observed in needles with a straight triangular taper is greatest in the region of the tip, (Fig. 3b). Furthermore, we were able to generate this post-constriction increase in shear rate in tapered needle types by increasing the length of the narrowest section of the needle (data not shown).



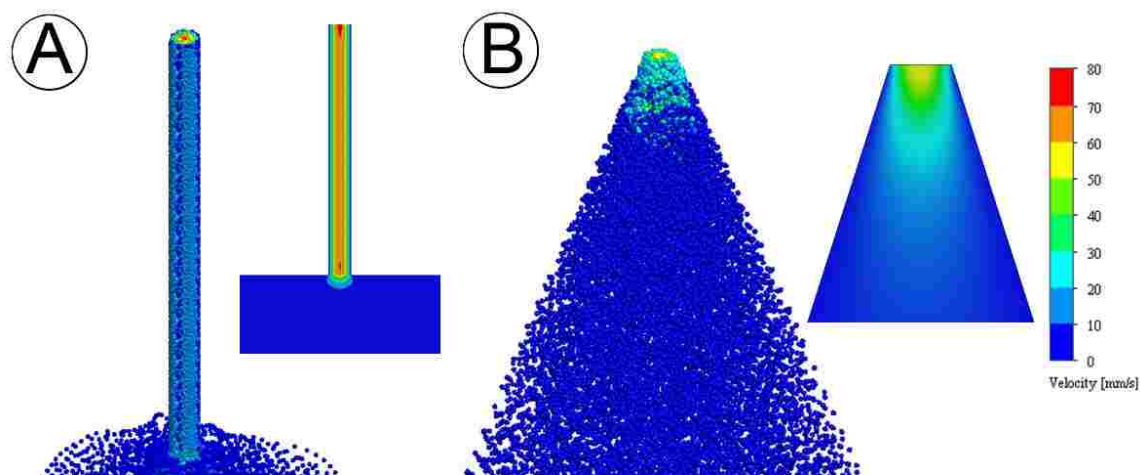


Fig. 2. CFD particle studies of the bio-deposition process under conditions that favor aggregation. Heat map graphical representations of particle velocities of  $10\mu\text{m}$  wide particles, the typical diameter of cells, traveling through idealized microneedle geometries representing: (a) conventional ‘luer-lock’ needle type and (b) triangular needle configurations under conditions of steady, non-Newtonian flow with a constant mass flow of  $6 \times 10^{-5} \text{ kg/s}$ . The inlet and exit diameter for all needle conditions equaled  $1 \text{ mm}$  and  $60\mu\text{m}$ , respectively. The flow outlet boundary condition equaled standard atmospheric pressure ( $101325 \text{ Pa}$ ). Our model conditions accounted for the effects of gravity. The exit velocity for the conventional ‘luer-lock’ condition (a) was  $72 \text{ mm/s}$ , whereas the triangular needle (b) was  $55 \text{ mm/s}$ . The aggregation of cells within the needle tip was encouraged by increasing particle accretion rates and lowering the normal and tangential coefficients of restitution at the needle wall. Under these conditions, particles near the exit of the microneedle with zero velocity (shown in blue) were only observed in the conventional ‘luer-lock’ geometry types.

Using the results from our simulations, three microneedle geometry types were fabricated using a programmable pipette puller. The programmable pipette puller and our glass pipettes provided the ideal process to fabricate of many custom needle configurations. To provide a comparison to the standard 28-gauge stainless steel needle, these three types are shown in (Fig. 3c). The three needle types shown in (Fig. 3c), from left to right, are examples of a 3 mm long straight-triangular needle with a 150 $\mu$ m tip diameter, a 5 mm long curved needle with 150 $\mu$ m diameter, and a 6 mm long curved needle with a 75 $\mu$ m diameter. One notable difference between the conventional needle and our pulled needles is the length of the narrow channel.

The narrowest section of the conventional, stainless-steel needle is typically 30 mm long, which is five times longer than the typical length of our fabricated needles (~5 mm). Using needles with geometric features that minimize the amount of time cells travel through these narrow channels presents fewer opportunities for cells to aggregate, with a concurrent reduction in detrimental forces, both of which are a significant process improvement. Furthermore, by fabricating the needle from borosilicate glass tubes we were able to retain a high degree of structural rigidity without the need to increase the thickness of the needle wall. That is to say, the ratio of the outer-diameter to the inner-diameter is substantially lower for the glass needles than the conventional steel needle (Fig. 3c). This provided a substantial increase to the print resolution of our system. The conventional needle was not capable of the same degree of positional precision and repeatability as the glass needle. When compared to glass, the thin stainless-steel needle has more elastic material properties, which made it prone to bending during the printing process. The nonlinearity across the needle meant the needle tip was not always precisely above the target site. This also negatively impacted the plotting process by introducing insertion angles that were not always perpendicular to the target site, which resulted in increased disruption of the gelled material surrounding the target site.

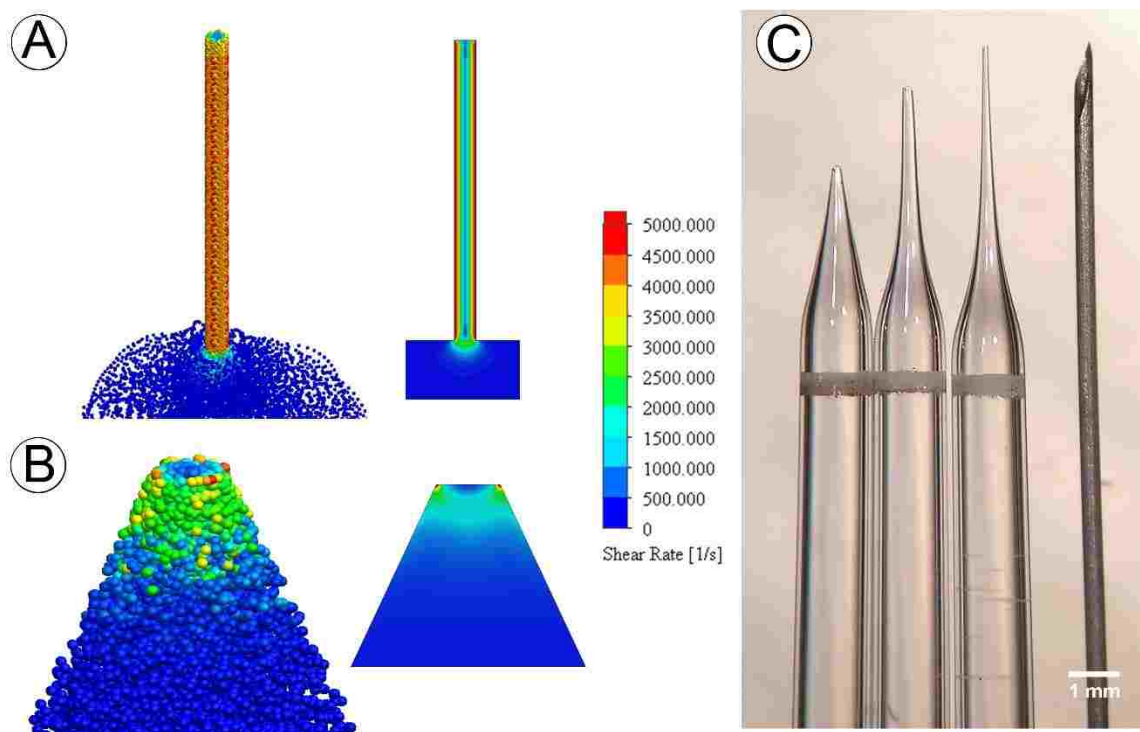


Fig. 3. Shear Rate results from CFD particle studies of the bio-deposition process using various microneedle geometries.  $10\mu\text{m}$  wide particles, the typical diameter of cells, traveling through idealized microneedle geometries representing: (a) Conventional 'luer-lock' needle geometry, (b) triangular needle geometry under conditions of steady, non-Newtonian flow with a constant mass flow of  $6 \times 10^{-5}$  kg/s. The inlet and exit diameter for all needle conditions equaled 1 mm and  $60\mu\text{m}$ , respectively. The flow outlet boundary condition equaled standard atmospheric pressure (101325 Pa). Our model conditions accounted for the effects of gravity. Simulated results indicated cell sized particles travel through areas with greater amounts of shear in conventional 'luer-lock' needles than straight-sided triangular needles. (c) Examples of pulled-glass microcapillary tubes with tapered geometries (left to right): 3mm long straight-triangular needle with a  $150\mu\text{m}$  tip diameter, 5 mm long curved needle with  $150\mu\text{m}$  diameter, 6mm long curved needle with a  $75\mu\text{m}$  diameter, and 28-gauge stainless steel needle.

While we initially began our experimentation with a narrower 30-gauge needle, the high concentration of cells required for the printing process made printing through such long narrow needles unreliable due to frequent clogging. Through further experimentation, we found a 28-gauge needle provided the required performance for our experiments. Despite the 25  $\mu\text{m}$  increase in interior needle diameter than a 30-gauge needle, using 28-gauge needles did not completely alleviate the clogging issue. It should also be noted that the 28-gauge needle has an inner diameter four times larger than the pulled glass microneedles. Overall, borosilicate glass tubes which combine the needle and syringe into a single, rigid part with geometry optimized for fragile cell transfer are superior to conventional, stainless-steel needles.

#### *2.4.3 Cell Viability Assay*

To further study the effects of microneedle geometry on the dynamic process of bioprinting, we sought to determine if there was an appreciable real-world impact seen when applying the various needle permutations. To accomplish this we used an immortalized, non-tumorigenic, adult MEC line, MCF-12A. Following injection into 96-well plates, the cells were assayed for metabolic activity 1 hour post-printing and then again 96 hours post-printing. Results from the AlamarBlue assay indicated a significant reduction in the number of viable cells 1 hour post-printing for the syringe 28-gauge needle condition compared to control (no-tip) for two printing speeds, 600  $\mu\text{l min}^{-1}$ , 1000  $\mu\text{l min}^{-1}$  (Fig. 4a,  $*p < 0.05$ ). This experimental data supports results from our simulations. A significant increase in viability was also observed 96 hour post-printing for the 1000  $\mu\text{l min}^{-1}$ , straight-cone or triangular condition, compared to control, (Fig. 4b,  $*p < 0.05$ ). These data confirmed that while survival was comparable amongst many of our needle designs, when print speeds increase, a corresponding reduction in viability is observed in needles that were previously shown to have a greater shear rate. This is likely due to the initial stress placed upon the cells resulting in a lack of cellular division during the 96 hour post-print.

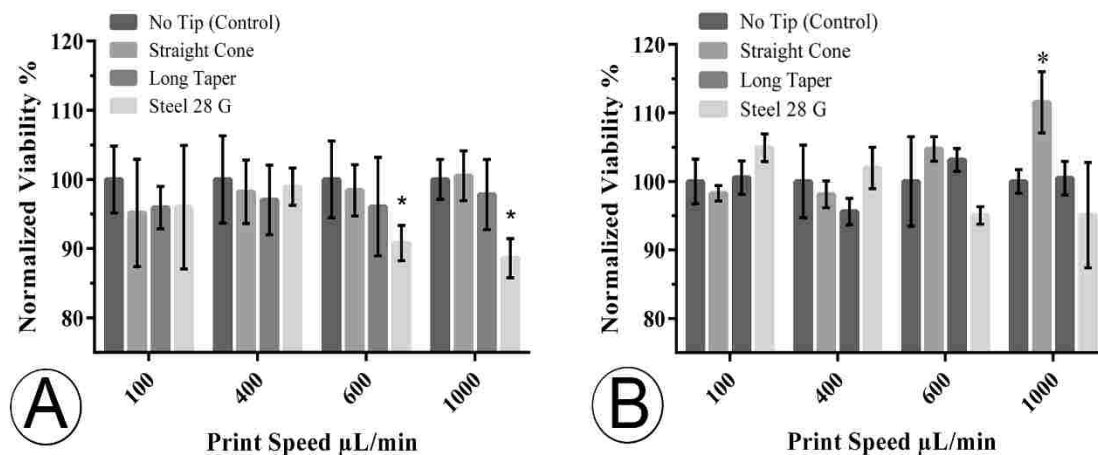


Fig. 4. MCF-12A Alamar Blue cell viability studies post-printing. (a) Alamar Blue reduction 1 hour post-printing ( $*p < 0.05$ ), (b) Alamar blue reduction 96 hours post-printing ( $*p < 0.05$ ). MCF-12A cells were suspended in media to a concentration of  $1 \times 10^6$  cells/ml. For all conditions, approximately  $25\mu\text{l}$  of media was loaded into the needle at a rate of  $10\mu\text{l}/\text{min}$  and dispensed into wells of a 96 well plate at one of four rates: 100, 400, 600, and  $1000\mu\text{l}/\text{min}$ . All four rates were repeated in three separate wells for a total of 12 wells per condition. Four needle conditions; no-tip (control), 27-gauge needle, straight cone, and long tapered needle were tested, giving a total of 48 wells. The sample mean viability was calculated and normalized to the initial viability of the no-tip control. Statistical significance was determined using one-way ANOVA with Dunnett's post hoc test ( $*p < 0.05$ ). Error bars, mean  $\pm$  s.d.

#### 2.4.4 Print Resolution Verification

As the diameter of most somatic human cells are between 10–30  $\mu\text{m}$ , and the spacing between injection points is largely determined by the diameter of the needle, we wished to generate a system capable of printing as close to this target range as possible. Precise placement of different cell types or signaling molecules and other various components in as close proximity to a 'cellular' resolution would be highly advantageous. To test the limits of printed cell resolution and the possibility of obtaining single cell extrusion events, we injected 1nl of media containing GFP labeled MDA-MB-468 cells into ~1 mm thick Geltrex, (Fig. 5a). To provide better illustration of this process, (Fig. 5b-d) represent GFP, bright-field, and combined channels of the single cell 'events' our system generates. Analysis of the single-cell extrusion events indicated our system is capable of reliably extruding single cells. To further examine the capacity of our printer, we quantified the distances among printed cell locations using ImageJ software to define positional precision. This analysis found the X and Y resolution to be  $\pm 6.34\mu\text{m}$  and  $\pm 9.71\mu\text{m}$ , respectively, confirming the factory-listed resolutions ( $13\mu\text{m} \times 13\mu\text{m} (\pm 6.5\mu\text{m})$ ). In addition to positional precision, bioprinting techniques also require precise control over the amount of extruded material.

To determine how effective our printer was at controlling the amount of extruded materials, we generated a gradient of GFP labeled rat epithelial cells by decreasing the extrusion amount in each successive row from 70nl, 60nl, 50nl and 10nl, (Fig. 5e). Upon manual counting, the number of cells within each print location, from top to bottom, averaged  $68 \pm 6$ ,  $62 \pm 4$ ,  $51 \pm 4$ , and  $8 \pm 2$ , respectively. The theoretical cell concentration in the media used to generate the gradient study in (Fig. 5c) represented a distribution of 1 cell per nl. Given this information, we observed an overall congruency among the number of counted cells and the directed extrusion amount. The variation in the number of printed cells was greatest in row one, the group with the largest extrusion amount. We expected to observe greater variation in the number of cells in the larger extrusion conditions because our approach is largely based on pairing the probability of a single cell within a specified extrusion amount. The duration of the plotting procedure was less than 3 min. Therefore, it appears printing within this time window prevents confounding variables such as cell settling due to gravity. The results in Fig. 5 provide information on the ability of the system to repeatedly handle volumes from 1 to 100nl. Furthermore, they provide insight into our systems ability to repeatedly extrude a set number of cells within a single target volume

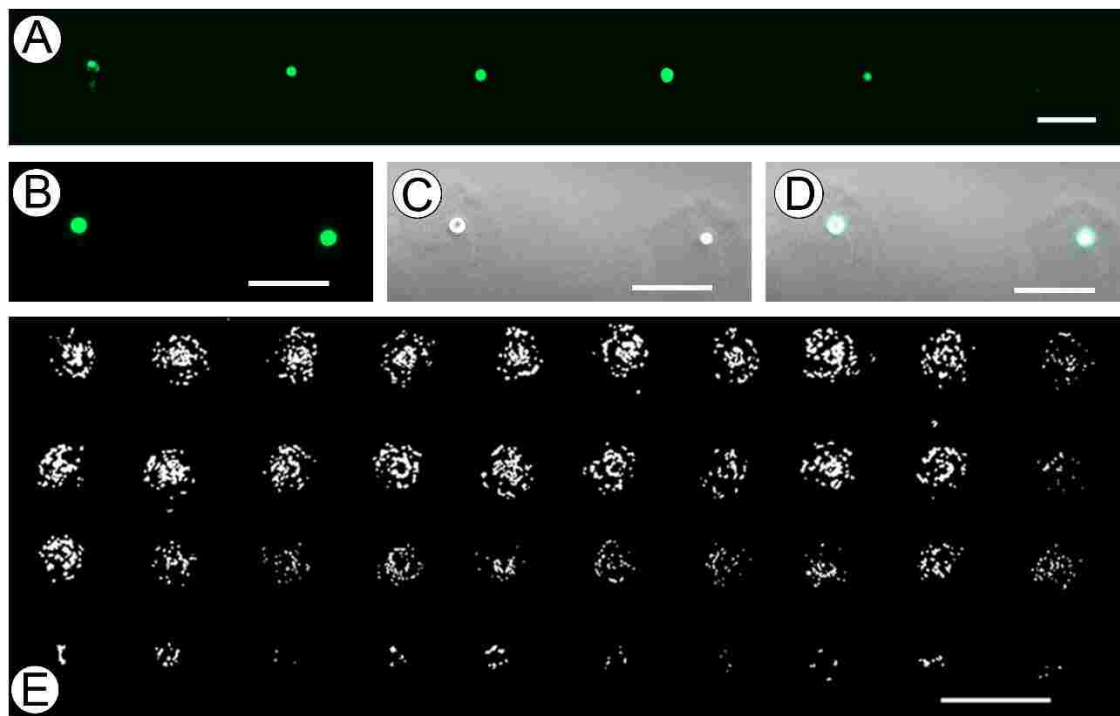


Fig. 5. Printer resolution and functional limitations. (a) 1nl extrusion, each containing a single GFP labeled MDA-MD-468 cell printed into ~ 1mm thick Geltrex. Scale bar 100µm. (b) GFP channel of single-cell extrusion event using MDA-MD-468 cells. Scale bar 100µm. (c) Bright-field channel of the same single-cell extrusion event. Scale bar 100µm. (d) Combined GFP and bright-field. Scale bar 100µm. (e) Decreasing gradient of GFP labeled rat epithelial cells generated by extruding 70µL, 60µL, 50µL, and 10nL. Scale bar 300µm.

#### 2.4.5 Bioprinted hiPSCs

Bioprinting pluripotent cells to generate biomimetic embryonal structures is a crucial step for disease modeling and tissue engineering. However, the printing process can physically alter the cellular structure resulting in unwanted shifts in gene expression and protein function. Having previously determined our extrusion system has minimal shear and pressure related effects on cells, we hypothesized that our system would have no negative impact on hiPSCs printed into either differentiation or pluripotent-conductive environments. We first wanted to determine if our system was capable of printing hiPSCs that retain their pluripotency post-printing. To test this, we used our pulled glass needles to print 3D aggregates of hiPSCs using pluripotency-conductive E8 media into growth factor reduced Geltrex. Following 7 days post-printing of the iPSCs we then stained the aggregates with pluripotency antibody TRA-1-81, a cell surface marker specific for pluripotent cells (Fig. 6a), confirming that our system does not alter the ability of iPSCs to retain a pluripotent state.

We next wanted to test the ability of our system to generate differentiated EBs. To confirm the differentiation of our injected hiPSCs, we compared their gene expression changes to the gold-standard hanging-drop EB method. We therefore printed hiPSC in Geltrex (500 cells per injection) with FBS containing media and in tandem deposited hiPSCs on culture flask lids (500 cells per droplet) and following lid inversion, allowed them to incubate at 5% CO<sub>2</sub>, 37 °C for 7 days. To then evaluate and confirm that the differentiated EBs were similar in nature, mRNA was extracted, and qRT-PCR was performed. The results of our gene expression assays indicated a significant up-regulation of differentiation markers for the endoderm (Sox17), mesoderm (Hand1), and ectodermal (PAX3) lineages in the printed hiPSC group as compared to non-printed, non-differentiated control hiPSCs, (Fig. 6c),  $*p < 0.01$ ). Interestingly, the gene expression was also significantly upregulated as compared to the hanging drop EBs, possibly indicating a more mature differentiation. To observe the motility and growth of our injected hiPSCs we followed the injections with time-lapse imaging. This revealed the initial formation of spheroids followed by the dynamic growth of secondary and tertiary structures similar to budding, elongation, and increased complexity over 7 days, (Fig. 6d, & Sup. Movie 2.1-2.3).



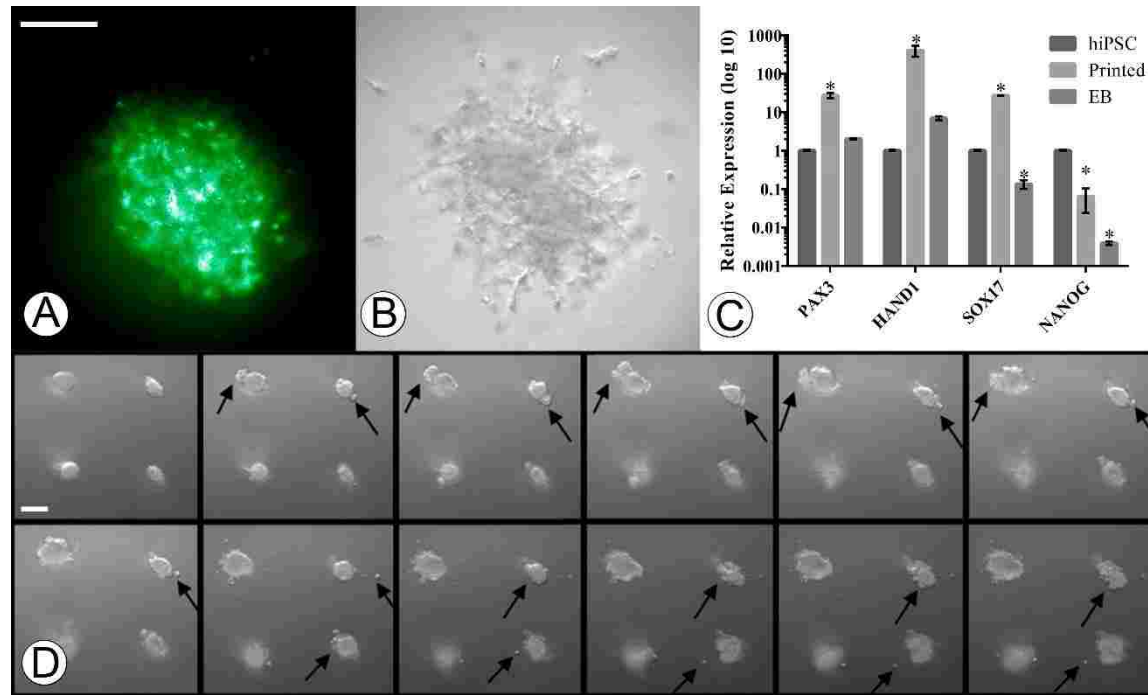


Fig. 6. 3D printed hiPSCs. (a) Presence of green fluorescence due to TRA-1-81 binding to undifferentiated pluripotent cells in 3D printed hiPSC aggregate 7 days post-printing. Scale bar 50 $\mu$ m. (b) Bright-field image of 3D printed hiPSC aggregate. (c) Gene expression profiles of hiPSCs using markers for ectoderm (Pax 3), mesoderm (Hand 1), endoderm (Sox-17), and pluripotent marker (Nanog) ( $*p < 0.01$ ). Error bars, mean  $\pm$  s.d. (d) 7 day-time lapse images of bioprinted hiPSCs in a 1:1 mixture of Geltrex/differentiation supportive media reveal dynamic growth and increased complexity (left to right, top-left taken at t0).

## 2.5 Discussion

Using 3D printed parts and highly accessible hardware, we were able to reliably print at precise XYZ locations within 3D hydrogels cellular aggregates in various concentrations with injection volumes ranging from 1nl to hundreds of microliters with spatial resolution only limited by the diameter of the needle itself. Currently, our system can obtain prints containing 1 cell per injection event. We attribute part of this cellular resolution to the use of stepper motors, which are ideally suited for extrusion-based bioprinting as they offer a unique solution for open-loop position control. Specifically, the output shaft rotates in a series of discrete angular intervals, or steps, each time a command pulse is received, therefore the exact displacement of the shaft is known. This feedback allows the user to modify the acceleration rates and deceleration rates of the fluid while traveling through the needle during 3D printing experiments. This forward/reverse positional control gives an additional level of process control unseen in solenoid valve-based systems that have been previously examined<sup>90,93</sup>. Additionally, the shaft of the motor will remain at a specific step until another step pulse is supplied, which provides exceptional positional control and eliminates leaks from the needle tip.

It is known that the fluid characteristics during syringe needle flow introduce three main types of mechanical forces capable of cell disruption: (i) shearing forces due to linear shear flow, (ii) pressure drop across the cell, and (iii) stretching forces due to extensional flow<sup>66</sup>. Numerous studies have implemented novel hydrogel-vehicle systems as a sacrificial, viscoelastic material to encapsulate cells and alter the distribution of damaging mechanical forces experienced during flow<sup>66,97,101,102</sup>. Yet, despite encapsulation in alginate solution (1.5% w/v), one study found ink-jet dispensing pressure demonstrated a more significant effect on cell viability than nozzle diameter; constructs printed at 40 psi showed a 38.75 % reduction in viability compared to those printed at 5 psi<sup>103</sup>. Recently, Faulkner-Jones et al found an effect of nozzle length and dispensing pressure on human pluripotent stem cell viability; cells printed through an 8.9mm long nozzle showed higher levels of viability than those in a 24.4mm long nozzle<sup>93</sup>. We therefore tested if injection systems which impart the lowest amount of overall shear would be preferable for fragile cell transfer; and if those systems which minimize the amount of time a cell flows through the highest

shear-rate section of the needle (or nozzle) would be preferable to systems in which the cells spend a greater amount of time flowing through high shear-rate sections.

To investigate this, we compared the force distribution of several needle types using FEM to identify features related to cell damaging forces. This approach enabled us to examine the development of these forces throughout the bioprinting process using systems of equations that included boundary conditions with slip along the needle wall. Mathematical models have been developed which indicate tapered needle geometries result in different cell damages due to the conical geometry and changing force distribution in the needle<sup>100</sup>. Billiet et al. found a significant pressure and needle type dependence on cell viability; at low inlet pressure, conically shaped needles are preferred over cylindrically shaped ones<sup>104</sup>. However, they found this advantage disappears at higher inlet pressures, yet they did not vary the length of the needle or the angle of the needle tip in their studies. Our investigation found short, conically shaped needles are preferred over long cylindrically shaped geometries due to a favorable axial pressure gradient that requires less energy to accelerate fluid through the microneedle, and a substantial reduction in the amount of shear in the needle tip. When the cross-section of a pipe gradually narrows, such as the straight-triangular needle in (Fig. 3b), the streamlines follow closely along the contours of the pipe and virtually no extra frictional losses are observed. By generating a more even transition to the narrow diameter needle tip, tapered needles provide a better-suited environment for fragile cell transfer. Furthermore, when this transition is abrupt, such as those of the conventional 'luer-lock' configurations, the inner diameter of the syringe is notably larger than the needle tip, and the cells undergo a correspondingly abrupt increase in linear velocity as they pass into the needle, also known as extensional flow. This convergence to a small point, coupled with the increased shear seen in the long, cylindrical needle appear to be the two components that contribute to unfavorable printing conditions related to fragile cell transfer. With these hypothetical variations in mind, we confirmed that syringe-needle extrusion rates greater than  $600 \mu\text{l min}^{-1}$  influence cell viability when compared to no-tip controls. Additionally, when examining the 96-h post injection viability it was clear that extrusion velocity and the needle geometry had a significant effect on growth.

3D based organogenesis from hiPSCs is one of the most exciting areas of tissue engineering and biofabrication. The approach of self-organizing pluripotent cells into functional differentiated cells not only represents a better model of natural processes, but also serves as a highly efficient method of organogenesis. Our investigation provides essential information on how biofabrication

parameters such as needle geometry and flow rates may affect the post-printing behavior of hiPSCs. Positive TRA-1-81 staining of hiPSC printed aggregates in pluripotent supportive environments, indicated our printing device was capable of delivering unaltered pluripotent cells into 3D environments without the need for protective encapsulation strategies. Furthermore, when these same pluripotent cells were injected into differentiation signaling environments, the printed hiPSC aggregates generated small, spherical clusters of cells that then began to depart from the main body and wander through the 3D matrix. Interestingly the gene expression analysis revealed a significant increase in differentiation and pluripotent markers as compared to both the non-differentiated iPSC and the standard EB formation methods. It is known that the physical features of the surrounding structure affect the differentiation of stem cells, therefore, one way to explain the increase in relative expression of these genes in the printed group, when compared to the non-printed control, may be due to an interaction among the hiPSCs and 3D gel-matrix. Instead of directly mixing these highly sensitive cell types with the scaffold materials required to generate 3D structures, our approach sought to prevent these types of cell-structure interactions by placing cells into specific 3D locations inside a pre-formed, 3D architecture. Because these cells are not directly included in the fabrication process, which often requires the structural change of the scaffold from a liquid to a gel post-printing, this method attempts to eliminate these types of extraneous variables to better understand the differentiation pathways that iPSCs follow when placed in a 3D environment. This feature could expose many future advantages that would establish a better understanding of normal tissue and organ development. This holds many benefits for developing models that better mimic human disease as well as affording us the capability to design and construct accurate replacement cellular constructs.

Here, we have described a simple process for development of an accessible and high precision 3D bioprinter through modification of an inexpensive 'off the shelf' 3D printer. The bioprinter uses a pulled-glass capillary pipette to minimize shear stress and optimize positional control and precision. This minimal cellular impact enabled our system to successfully print hiPSCs while maintaining their pluripotency. Additionally, we were able to print hiPSCs into differentiation-conductive environments that generated cells of all three developmental germ-layers. To the best of our knowledge, our system is the first 3D printed, bioprinting system to reliably achieve single cell print resolutions within 50 $\mu$ m resolution, while also exerting minimal unwanted impact on the cells viability and post-printing fate. Furthermore, our system is highly

modifiable and can be fabricated for use on any 3D printer. This type of system is ideal for adaptation by both basic and clinical research laboratories for the study of cellular interactions and/or tissue engineering applications.

We would like to note that our bioprinting system upgrade cost less than \$200 (not including the off-the-shelf printer, which could be substituted for other models). Our hope is our system, or similar systems will lower the technical and financial hurdle of 3D bioprinting to any laboratory with an interest in furthering the developments of 3D cellular biology. As open-sourced projects have developed advanced software systems such as Unix, and hardware solutions such as Arduino and Raspberry Pi, here we institute similar initiatives within the field of biofabrication. Overall, these results indicate we successfully achieved our first objective of designing and manufacturing an accessible, 3D bioprinting device capable of reliably printing cell aggregates and other biological materials.

All you behold, tho' it appears without,  
it is within—in your imagination,  
of which this world of mortality is but a shadow.

William Blake

## CHAPTER 3

### 3D BIOPRINTING MAMMARY EPITHELIAL ORGANOID

#### 3.1 Overview

While capable of generating high-throughput experimental designs to answer today's 'big data' biological questions, bioprinting technology has remained inaccessible to most research labs due to the uncertainty as to whether the research benefits will outweigh the operational cost. In this study, we set out to incorporate our bioprinting technology into 3D cultures of human MECs. First, we hypothesize that MEC organoid formation is determined and regulated by the amount of local cell-cell interactions. To test this, attention was given to the ability to control the amount of 'bio-ink' deposited in a specified location to promote MEC 'self-assembly' into cell-organoid structures. Second, it was hypothesized that the orientation of *in vitro* mammary organoid formation is determined by neighboring cell activity that imparts directional cues during the initial stages of MEC cell-organoid structure formation. This hypothesis was tested by determining the spatial distribution required to direct individual organoids to undergo coordinated, organoid fusion events along the entire length of the bioprinted array. Finally, this chapter concludes with a review of current work to develop and employ new methods to incorporate additional 'bio-inks,' cell types, and other biologically active materials into 3D cultures.

Standard 3D *in vitro* culture techniques, such as those used for MECs, rely on random distribution of cells through hydrogels. While these systems offer advantages over traditional 2D models, limitations persist owing to the lack of control over cellular placement within the hydrogel. This results in experimental inconsistencies and random organoid morphology. Robust, high-throughput experimentation requires greater standardization of 3D epithelial culture techniques. Here, I detail the use of a 3D bioprinting platform as an investigative tool to control the 3D-

formation of organoids, through the ‘self-assembly’ of human MECs. Experimental bioprinting procedures were optimized to enable the formation of controlled arrays of individual mammary organoids. I define the distance and cell number parameters necessary to print individual organoids that do not interact between print locations, as well as those required to generate large, contiguous organoids connected through multiple print locations. Results indicate that as few as 10 cells can be used to form 3D MEC structures in a single print location. Furthermore, spacing print locations up to 500 $\mu$ m apart can be used to guide the development of large organoids with directed shapes and sizes. Using these fusion parameters, both linear and non-linear (contiguous circles) can be generated with sizes based on the available material inside the culture area. Results confirm cells from individual print locations interact to form structures with a contiguous lumen. This platform is adaptable to different culturing protocols and is superior to traditional, random 3D culture techniques in efficiency, reproducibility, and scalability. Importantly, due to the low-cost accessibility and CNC driven processes of our 3D bioprinter, we have the ability to disseminate our experiments with absolute precision to interested laboratories.

### **3.2 Introduction**

3D culture systems for generating organoid cultures of MECs inside collagen matrices were first introduced over four decades ago<sup>33</sup>. In 3D culture, multiple parameters operate together to affect both experimental outcomes and interpretation of experimental results. These parameters include cell type, cell-cell interactions, ECM composition, culture media, and mechanical properties such as matrix stiffness and cell confinement<sup>40-50</sup>. Standard 3D culture procedures involve either mixing dispersed mammary epithelial cells within ECM substrates prior to gelling, or by culturing cells on top of a pre-formed ECM gel. Once polymerized, the ECM gel can be left attached to the culture dish or floated. The encapsulated cells will then randomly organize into organoids which remodel and reorganize the substrate matrix to generate structures composed of morphologically polarized cells facing an open lumen<sup>31,34,36-39</sup>. However, the size and morphology of resulting organoids varies greatly, even within the same ECM gel substrate. While some variability inevitably results from disparities in local environmental conditions, such as collagen fiber anisotropy within specific regions of a gel, a major source of potentially controllable

variability results from the random distribution of cells within the gel<sup>57,59,61,62,105,106</sup>. This variability leads to difficulty in interpreting and reproducing results, especially laboratory to laboratory. As inter-laboratory reproducibility is a major concern in modern biomedical research, platforms that will allow for better control and reproduction of results are highly desired<sup>107</sup>.

We have recently described the adaptation of an off the shelf 3D printer for the purposes of bioprinting cells in 3D substrates<sup>108</sup>. Our goal was to design an accessible, open-access bioprinter that would not be cost prohibitive to research laboratories. Because of the precision afforded by the CNC system, and the ability to share the G-CODE underlying the printing process, the use of bioprinting in basic research laboratories offers promise for new standards designed to increase internal and intra-laboratory experimental reproducibility. Specifically, the use of CNC systems to control the spatial deposition of cells in 3D structures appears well suited to recreate the tissue-specific, contextual cues needed to overcome the limitations of manual pipette-patterning<sup>108,109</sup>. Here, I describe the adaptation and validation of an accessible bioprinter to produce high-fidelity, spatially-controlled arrays of human mammary organoids inside 3D collagen matrices. We demonstrate the superiority of our printing process over manual matrix embedding techniques in efficiency and consistency in organoid morphology. We further describe parameters necessary to generate large organoids with shapes dictated by print locations (e.g. linear or circular). These data lay the groundwork for adapting 3D bioprinting methods using additional cell types and 3D matrices, thereby providing an ideal method to derive empirical standards aimed to improve the *in vitro* culture of biological processes such as development and tumorigenesis.



### 3.3 Materials and Methods

#### 3.3.1 Cell Culture

Immortalized non-tumorigenic human breast epithelial cell line, MCF-12A was purchased from ATCC. MCF-12A cells were initially cultured in 2D on tissue culture plastic in a 75 cm<sup>2</sup> flask supplemented with a 1:1 mixture of Dulbecco's modified Eagle's medium and Ham's F12 medium (DMEM/F12), 5% Horse Serum, 20 ng ml<sup>-1</sup> hEGF, 0.01 mg ml<sup>-1</sup> bovine insulin, 500 ng ml<sup>-1</sup> hydrocortisone and 1% ABAM (ThermoFisher). MCF-12A cells were cultured at 37.0 °C and 5.0% CO<sub>2</sub>. After confluence, the cells were dissociated using TrypleE (ThermoFisher) and collected by centrifugation.

#### 3.3.2 Preparation of Collagen ECMs and Manual Cell-Matrix Embedding

For manual cell-matrix embedding studies, single cell suspensions of MCF-12A cells were mixed with neutralizing solution and acidified rat tail collagen I (Corning) as specified by the manufacture, unless noted otherwise, to a final concentration of 1.5 mg/ml. Immediately after mixing, 500µl of neutralized collagen I gel material, containing approximately 5000 cells, was dispensed into a 24 well plate and allowed to solidify and adhere to the surfaces of the well for 1 hour in a laboratory incubator at 37.0°C and 5.0% CO<sub>2</sub>. After gelation (solidification), 500µl of cell media was added to the wells. Subsequent media changes were performed every 3 days. VitroCol, human collagen I solution (Advanced BioMatrix), was prepared according to manufacturer's recommendation to a final concentration of 1.0 mg/ml. For all printing experiments, a minimum of 500µl of collagen gel was dispensed into individual wells of a 24 well plate and allowed to solidify for 1 hour in a laboratory incubator at 37.0°C and 5.0% CO<sub>2</sub>. For all experiments, cells were monitored using a combination of brightfield imaging/fluorescent imaging using a Zeiss axio-observer Z1 fluorescent microscope, or time-lapse imaging using a Lumascope 620 microscope.

### 3.3.3 Bioprinting System

A previously developed bioprinting system was used to robotically insert a microneedle into specified 3D locations of a polymerized collagen gel<sup>108</sup>. Immediately before printing, 2D cultures of MCF-12A cells were dissociated into single cells using TrypleE (ThermoFisher), centrifuged at 300×g, and re-suspended in media to obtain a final ‘ink’ concentration of  $60 \times 10^4$  cells ml<sup>-1</sup>. Shortly thereafter, 50µl of cell-containing ‘ink’ was loaded into a sterile needle. Printing operations were initiated after the ‘ink’ containing needle was attached to the print head. The number of cells deposited in a target location was manipulated by varying the volume of cell-containing ‘bio-ink’ extruded from the needle tip, or to equalize volumes, by increasing or decreasing initial cell concentration. Printing operations were optimized to extrude specified numbers of cells inside the collagen I gel via a CNC insertion routine which deposited cell containing media at a specified ‘target’ location inside the polymerized collagen I gel. Users specified intended wells of commercially available tissue culture plates, printing locations, distances among printing locations, and the number of cells per target location. The experiment information was automatically converted into G-code, loaded into Repetier Host, and sent to the three-axis microcontroller of the bioprinter. The bioprinting system was located inside a benchtop biosafety cabinet during all printing operations. The heated print bed was set to 37° for all printing operations. Needles used by the bioprinting device were fabricated using a Sutter P97 programmable pipette puller to have tip diameters of 50µm. All printing equipment was sterilized using steam autoclave prior to printing procedures. After printing routines were complete, plates were covered with 500µl of media and placed inside a laboratory incubator at 37°C, 5% CO<sub>2</sub>. Post-printing, cells were monitored using a combination of brightfield imaging/fluorescent imaging using a Zeiss axio-observer Z1 fluorescent microscope, or time-lapse imaging using a Lumascope 620 microscope. Cell-specific media exchange was performed every 3 days. All experimental conditions were performed in triplicate.

### 3.3.4 Characterization of Organoid Growth and Morphology

Immediately after printing, the initial quantity of printed cells was verified using manual counting and image analysis using ImageJ and Matlab. Post-printing, cells were monitored up to

21 days using a Zeiss axio-observer Z1 fluorescent microscope. The size of organoids was determined by analyzing bright-field images taken daily for each experimental condition using ImageJ. Within this investigation, organoids were operationally defined as a cluster of cells with no clear cell-cell boundaries, or the inability to discern individual cells from neighboring cells.

### *3.3.5 Immunofluorescence Staining*

Gels were fixed in 10% neutral buffered formalin, paraffin embedded and sectioned. Sections were prepared for staining by deparaffinizing in a xylene substitute, rehydration, and heat-mediated antigen retrieval using pH 9 tris-EDTA with 0.05% tween 20. Sections were blocked in 10% goat serum and incubated with primary antibodies in a humidified chamber at 4°C overnight. Secondary antibodies were added for 1 hour at room temperature. Sections were counterstained with DAPI. Antibodies were used at the following concentrations: mouse monoclonal antibody to BetaCatenin [12F7] (1:50; ab22656, Abcam), anti-green fluorescent protein rabbit IgG Alexafluor 488 conjugated (1:75; Invitrogen A21311); rabbit monoclonal antibody to cytokeratin 5 [EP1601Y] (1:75; ab52635, Abcam), mouse monoclonal antibody to cytokeratin 8 [C-51] (1:35; ab2531, Abcam), rabbit anti-pan-cadherin (1:75; 71-7100, ThermoFisher), rabbit polyclonal antibody to GJB6 [Cx30] (1:25; HPA014846, Sigma-Aldrich), and rabbit polyclonal antibody to GJB1 [Cx32] (1:25; HPA010663, Sigma-Aldrich). Appropriate Alexafluor 488 and 568 conjugated goat antibodies (1:1000; ThermoFisher) were used for secondary antibody labeling. All sections were counterstained with DAPI and imaged using a Zeiss axio-observer Z1 fluorescent microscope.

### *3.3.6 Statistical Analysis*

Statistical analyses were performed using the software GraphPad Prism. Results were assessed for statistical significance using Student's *t* test. Differences were considered statistically significant at  $*p < 0.05$ .

## 3.4 Results

### 3.4.1 Manual Matrix Embedding Culture Technique

As the main aim of this work was to validate experimental bioprinting methods for investigating mammary epithelial biology in 3D culture, we first established baseline behaviors of MCF-12A cells using manual cell-matrix embedding techniques. Furthermore, to determine the effect of physical parameters on MEC behaviors in 3D cultures, we compared the growth patterns of MCF-12A organoid formation in attached and floating 3D collagen I gels. Similar to previous findings<sup>61,110</sup>, these results found an extremely high level of inter and intra experimental variability.

Heuristically speaking, organoid growth patterns during the first 5 days under these two conditions were similar. Day 1 following the manual embedding of cells within collagen gels, the cells were similar in morphology, with cells either remaining dispersed individually or forming small clusters (Fig. 7a,b). This activity seemed to correspond with the random nature in which the cells were embedded in the gel—i.e. the distance among cells in the 3D matrix.

In both conditions, noticeable structures emerge by day 5 (Fig. 7a,b). However, by day 8 the attached and floating conditions resulted in prominent structural variations, which, by day 14, presented distinguishable organoid morphologies (Fig. 7a,b). An average organoid size of  $(509 \pm 169\mu\text{m})$  and  $(302 \pm 114\mu\text{m})$  were obtained after 14 days of culture in attached and floating collagen I gels, respectively. Overall, three common organoid morphologies were observed: sphere like (Fig. 7c), duct like (Fig. 7d), and star like (Fig 7e,f) which ranged in size from 190-1235 $\mu\text{m}$ .

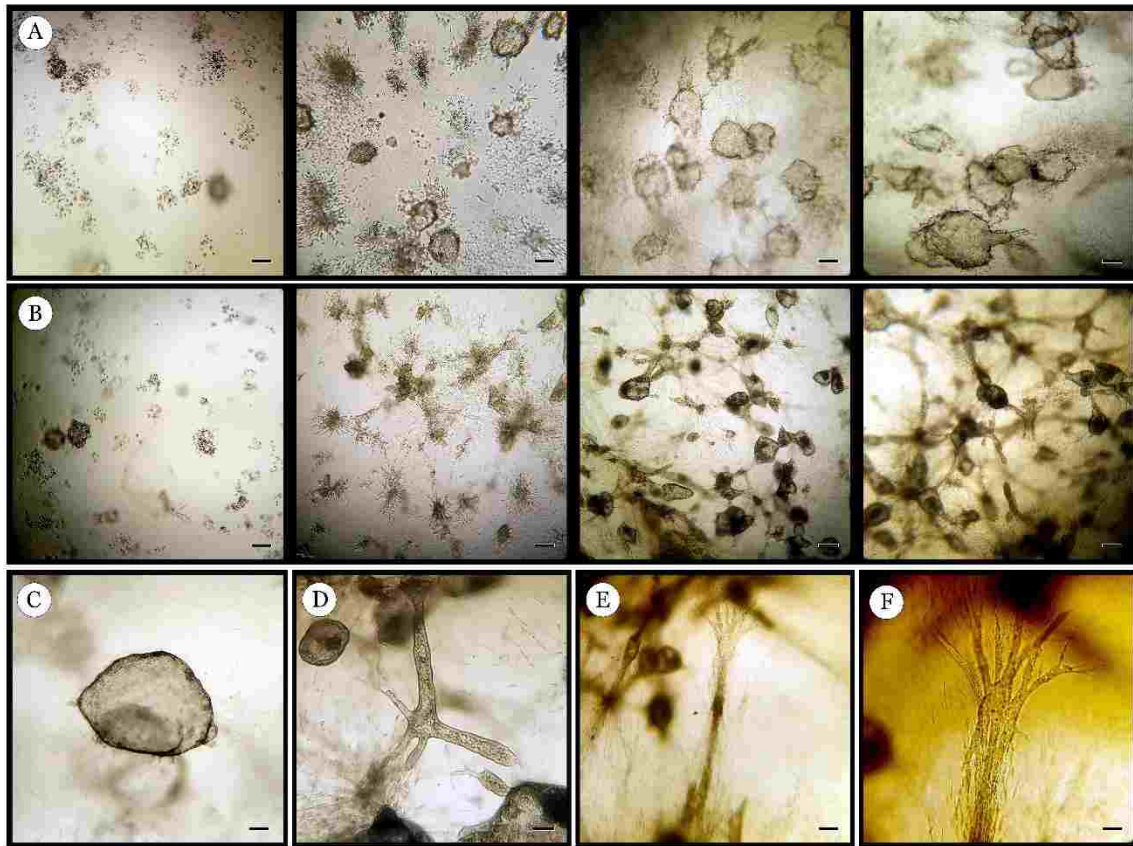


Fig.7. Manual method of MCF-12A Organoid Formation. Example of random organoid dispersion and morphology of MCF-12A cells following manual matrix embedding in collagen gels either (a) attached to the culture plate or (b) floating, at 5, 8, 10, and 14 days (left to right). Scale bar: 200 $\mu$ m. (c) Single phenotypic organoid observed in attached gels. Scale bar 50 $\mu$ m. (d) Organoid linking multiple organoids in floating gels. Scale bar 50 $\mu$ m. (e) Image showing organoid with protrusions extending into floating gel. Scale bar 100 $\mu$ m. (f) Additional organoid type found only in floating gel. Scale bar 100 $\mu$ m.

Interestingly, MCF-12A organoids in attached gels only formed hollow, single-cell thick, ‘sphere-like’ organoids ranging from 190-1235 $\mu$ m in diameter (Fig. 7a,c). However, the ‘sphere-like’ organoids in floating gels ranged from 100-618 $\mu$ m, displayed more complex morphologies, and contained a dark, inner cell-mass (Fig. 1d). Additionally, the cell structures produced in attached gels continue to grow into the boundaries of neighboring structures (Fig. 7a). In addition to the presence of organoid phenotypes not observed in the attached condition, floating collagen gel cultures resulted in networked arrays of organoid structures. (Fig. 7b). It appears that the ‘duct-like’ organoid phenotype is associated with directional growth patterns, which form networked structures among the ‘sphere-like’ acini (Fig. 7e). These ‘duct-like’ organoids were frequently preceded by and associated with cells exhibiting elongated morphologies with visible processes, likely demonstrating cell-matrix interactions (Fig. 7f). In agreement with previous reports<sup>62</sup>, these results indicated the floating collagen gels underwent gel shrinkage of several millimeters throughout the culture period.

Within 14 days in a standard 24 well plate, the initial mixtures of 5000 cells/well resulted in average of  $(439 \pm 59)$  and  $(1060 \pm 209)$  organoids/well for attached and floating conditions, respectively. Thus, attached gels require an average of 11.39 cells per organoid, whereas floating gels required about 4.72 cells per organoid. As can be seen from the images in (Fig. 7a,b), the matrix embedding technique resulted in random organoid distributions for both culture conditions, which further illustrates the difficulty in interpreting experimental findings using traditional embedding techniques. However, statistical analysis of experimental data indicated the effect of culture conditions was significant ( $*p < 0.001$ , two-tailed). These data support the idea that the increased rigidity of the culture environment has a negative effect on the ability of breast epithelial cells to form organoids. This implies that a biophysical component is involved in regulating breast epithelial differentiation. This observation is noteworthy because women with dense breast tissue have a four to six-fold increased risk of developing breast cancer<sup>111</sup>.

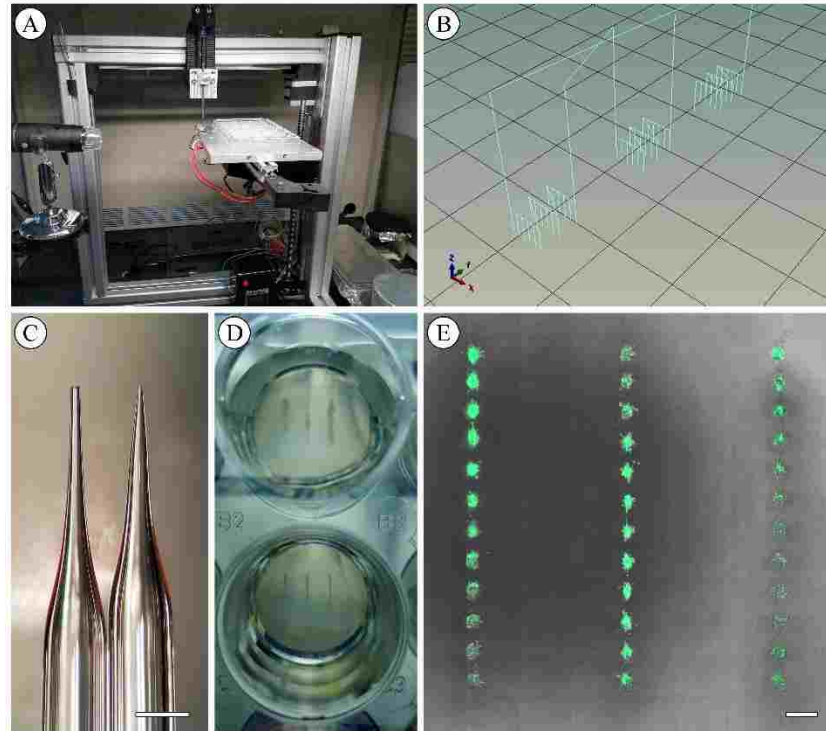


Fig. 8. Design of the 3D bioprinting platform. (a) Adapted commercially available 3D printer. (b) Example of machine path during insertion routine. (c) Pulled-glass microneedle. Scale bar 1mm. (d) 24 well plate containing 3D bioprinted mammary epithelial organoids 14 days post-printing. (e) Bioprinted MCF-12A organoids 7 days post-printing. Scale bar 500 $\mu$ m.

### 3.4.2 Generation of Consistent Individual Mammary Epithelial Organoids

Using this baseline as our comparator, we next sought to identify the core parameters to reliably generate and guide the formation of organoids using our low-cost bioprinting system (Fig. 8a)<sup>108</sup>. Our bioprinting method uses CNC processes to guide microneedles to directly insert cells into 3D locations of polymerized collagen I gels (Fig. 8b,c). Importantly, previous studies have established that multiple needle insertions into a polymerized collagen gel did not disrupt neighboring cell-deposits<sup>108</sup>. This bioprinting technique eliminated the random cell distribution commonly observed in layer-by-layer processes and manual cell-matrix embedding procedures by confining cell aggregates in specified locations (Fig. 8d,e).

We initially assessed if the formation frequency of individual human mammary epithelial organoids could be increased by controlling the initial number of singly-dissociated cells in a specified location. Using our bioprinting device, we dispensed cell-laden media at equivalent volumes in equally spaced, linear arrays inside collagen I gels and tracked them daily for 14 days (Fig. 9). Results indicated initial cell injections of  $\leq 5$  cells formed individual organoids at frequency of 1/50 and 28/50 at 7 and 14 days, respectively. However, when the initial printed cell number equaled 10 cells, our system achieved 37/50 and 49/50 organoid efficiency at 7 and 14 days, respectively. Using 40 and 60 cells resulted in consistent (50/50) organoid formation for both 7 and 14 days. These results indicate reliable generation of individual organoids can be achieved by increasing the initial number of cells ( $\geq 10$ ) in specified locations with a spacing of 500 $\mu$ m. We also found printed cell clusters containing cell numbers ( $\geq 10$ ) cells consistently develop branched processes, exclusively pointed towards neighboring organoids, which, by day 10, had formed a contiguous structure (Fig. 9). Furthermore, the temporal nature of this branching process increased correlative to the addition of more cells within the initial printing event. These results suggest MEC organoid formation is directly related to the quantity of cells within a local environment.



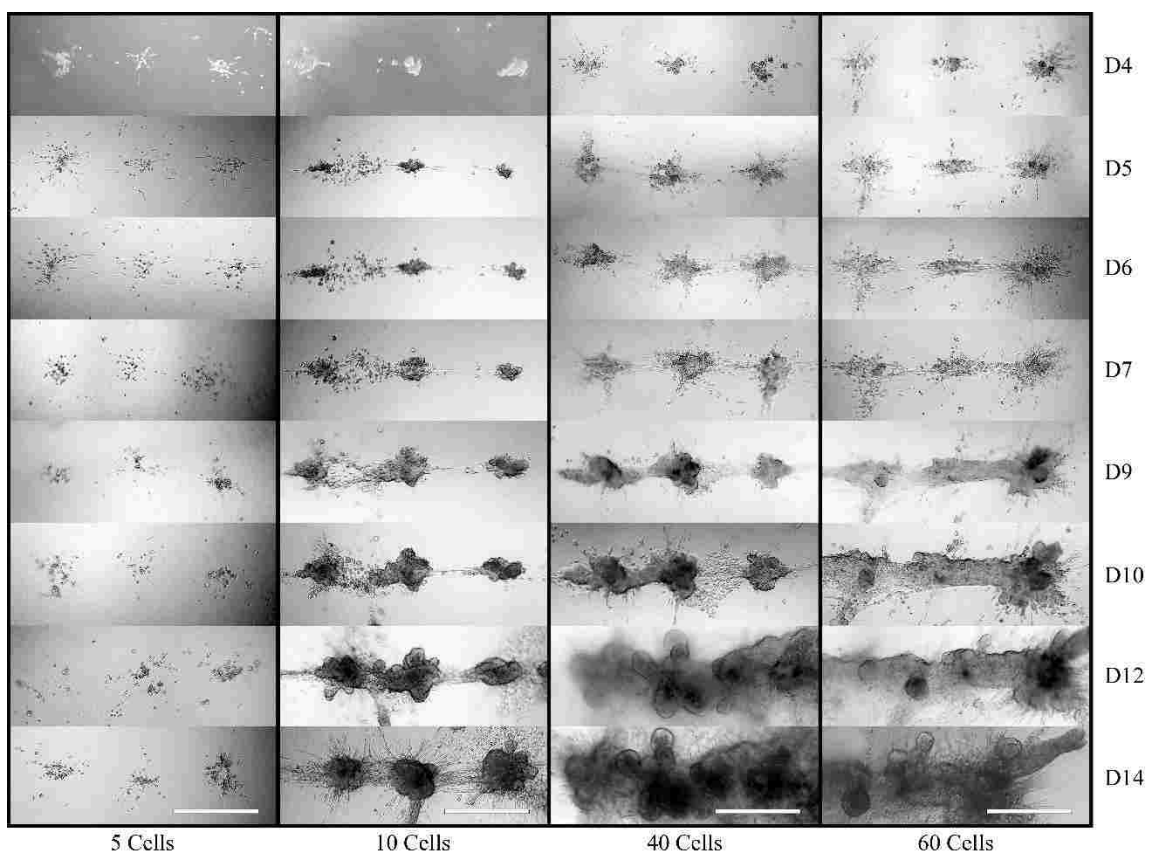


Fig. 9. Bioprinting results in consistent organoid formation. MCF-12A cells were printed at  $500\mu\text{m}$  between print locations using initial cell concentration of 5, 10, 40, or 60 cells (columns, left to right, respectively). Images were taken at Days 4, 5, 6, 7, 9, 10, 12 and 14 (rows top to bottom, respectively). Initial injections of 10 or more cells resulted in consistent organoid formation. Consistent fusion of multiple print locations was seen by day 14 when  $\geq 10$  cells were printed per injection site. Scale bar  $500\mu\text{m}$ .

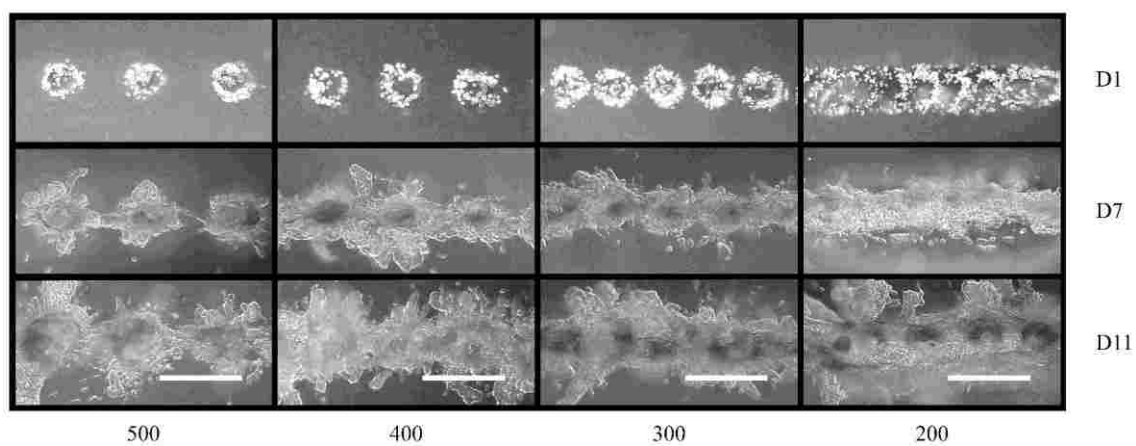


Fig. 10. Organoid fusion occurs between organoids printed up to 500 $\mu$ m apart. MCF-12A cells were printed (40 cells per deposit) at distances of 500 $\mu$ m, 400 $\mu$ m, 300 $\mu$ m, and 200 $\mu$ m (columns, left to right, respectively). Consistent fusion was seen by day 11 in all cases, with contiguous organoids forming between prints spaced  $\leq$  400 $\mu$ m apart. Scale bar 500 $\mu$ m.

### *3.4.3 Directing the Generation of Large, Contiguous, Mammary Epithelial Organoids*

As the consistent nature of individual organoid formation changed with the variation of cell number, we next sought to determine if varying the inter-organoid distances could evoke a similar impact on the bridged-contiguous organoid formation that we observed in our linear arrays. To this end, we monitored the effect of organoid spacing on growth behavior by printing MCF-12A cells along linear arrays of cell-deposits containing  $40 (\pm 6)$  cells in collagen gels (Fig. 10). Data indicated inter-organoid spacing ( $\leq 300\mu\text{m}$ ) directed collective cell growth of all (36/36) organoids into duct-like patterns along the entire length of the linear array ( $\sim 4\text{mm}$ ) within 7 days post-printing (Fig. 10). At  $400\mu\text{m}$ , 34/36 organoids fused within 7 days post-printing (Fig. 10). Twenty-three of the 36 organoids spaced  $500\mu\text{m}$  apart achieved organoid fusion within 7 days, however, 35/36 of these organoids achieved fusion by day 11 (Fig. 10).

Closer examination of the  $500\mu\text{m}$  print conditions indicated cell numbers increased during the first 3 days post-printing (Fig. 11a). Between day 3 and day 5, MCF-12A cell clusters began to form branched extensions, radiating from the initial print location (Fig. 11b). By day 7, these extensions matured and formed connections among neighboring organoids (Fig. 11c). Time-lapse imaging confirmed the branched extensions were directed toward neighboring organoids (Sup. Movie 3.1). Time-lapse imaging data also indicated global MCF-12A cell migration appears to follow the routes established by these initial extensions (Sup. Movie 3.2). It was noted that decreasing organoid spacing appears to promote the initial formation of a central structure corresponding to the directional-axis of the printed array.

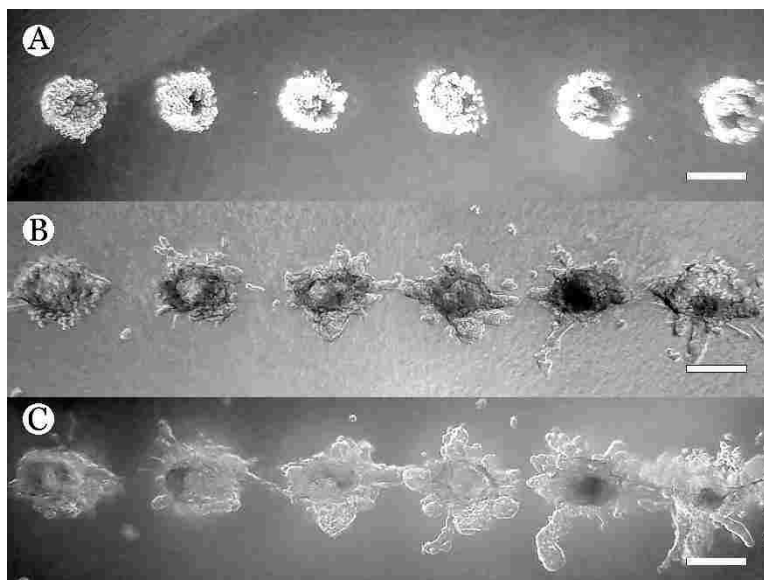


Fig. 11. Maturation and formation of MCF-12A organoids. Images of bioprinted, MCF-12A cell-deposits at 500µm spacing (a) 3 days post-printing, (b) 5 days post-printing, (c) 7 days post-printing. Scale bar 200µm.

Thus, by manipulating the spacing we can predictably increase the formation of a contiguous structure. Of note was the propensity of individual organoids to maintain the prescribed nature of the initial printed pattern throughout this fusion process. However, the importance of spacing distance on the degree of inter-organoid interactions was particularly highlighted when neighboring linear arrays printed  $\geq 700\mu\text{m}$  apart failed to achieve robust interaction (data not shown). We believe these results provide substantial evidence of the superior ability of 3D bioprinting platforms to direct and control the formation of MEC organoids than manual matrix embedding methods.

#### *3.4.4 Generating Additional Shapes Through 3D Bioprinting*

Next, we examined the possibility of directing contiguous luminal structures to conform to alternative shapes. We printed 40 cell clusters in a radial pattern in rat tail collagen gels with spacing patterns similar to our linear arrays at 500 $\mu$ m, 400 $\mu$ m, and 300 $\mu$ m (Fig. 12a). After 7 days, all of the print locations had formed individual organoids (Fig. 12a), and obvious processes and connections were actively forming among the 300 $\mu$ m spaced injections (Fig. 12a). By day 7, similar again to our linear arrays, all groups with at least 30 cells formed contiguous structures, which reflected the intended circular geometry (Fig. 12b,c). Furthermore, our ability to direct MEC structures was maintained throughout 24 days of culture, wherein the cells reacted similarly to the linear arrays by maintaining the initial print pattern, and eventually formed a contiguous, luminal circle  $\sim$  4mm in diameter (Fig. 12d). These findings indicate mammary epithelial migration patterns are not random, rather, the MCF-12A cells actively seek neighboring organoid structures to participate in the formation of large structures. Furthermore, when these structures were deformed using forceps, they quickly returned to their original shape. Overall, these data clearly highlight the tunable nature of our system, where initial cell number and spacing can consistently influence the formation of individual MEC organoids. This data also highlights the importance of defining and optimizing printing parameters for successful fabrication of large contiguous luminal organoids and structures.

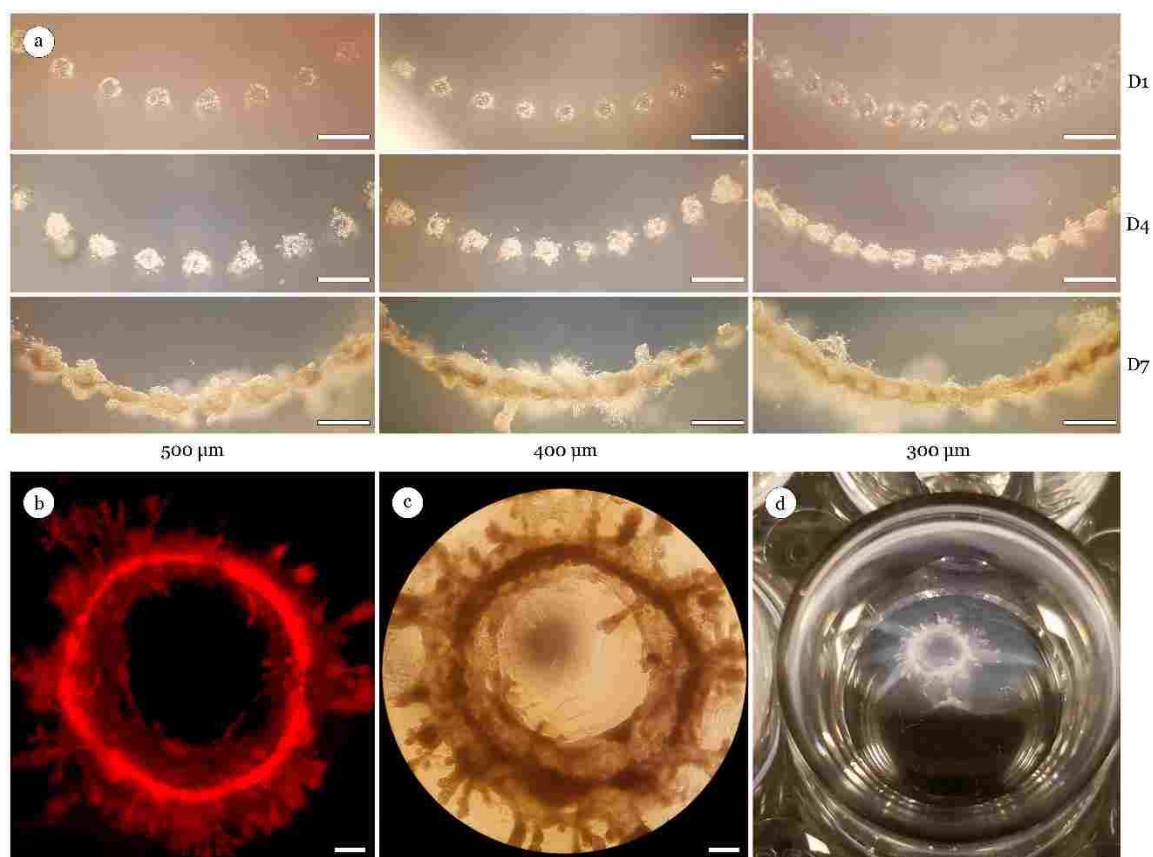


Fig. 12. Directed printing of non-linear organoids. (a) MCF-12A cells (40 cells per deposit) printed in a radial pattern with print spacings of (a) 500 $\mu$ m, 400 $\mu$ m, or 300 $\mu$ m. Images of cell clusters illustrate the ability to direct large scale mammary structures within 7 days using additional geometric configurations. (b) Fluorescent image of bioprinted, RFP MCF-12A cell clusters 14 days post-print demonstrating fusion of individual organoids into a contiguous circular organoid. (c) Brightfield image of large circular organoid 14 days post-print. (d) Example of a large circular organoid inside 24 well culture plate 24 days post-print measuring ~4mm in diameter. Scale bar 500 $\mu$ m.

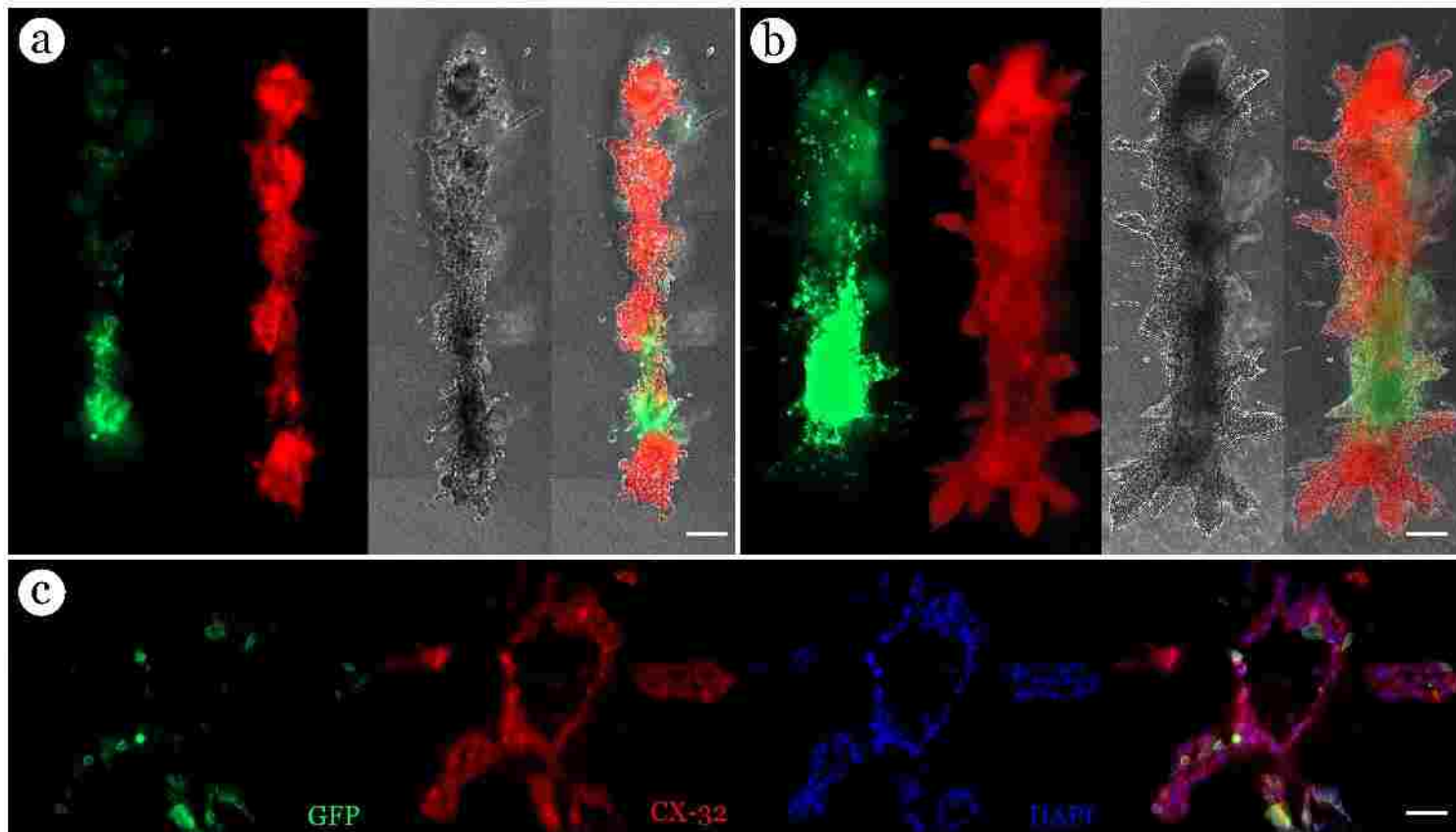


Fig. 13. Alternating RFP/GFP MCF-12A cell deposits to form contiguous organoids. (a) Day 7, and (b) day 9 organoids resulting from alternating RFP+ and GFP+ MCF12A cells using a 200 $\mu$ m spacing. Scale bar 200 $\mu$ m. (c) Immunofluorescence staining of Cx32 (red) and GFP (green) in cross-section of an organoid formed as described in a and b. The presence of GFP+ cells along the same lumen as RFP cells along with expression of Cx32 along RFP/GFP cell boundaries indicates the cells from adjacent print sites intermingled and formed cellular junctions. Scale bar 50 $\mu$ m.

### *3.4.5 Organoids Cooperate to Form Gap Junctions with Neighboring Organoids*

Having established the cell number and individual organoid spacing necessary to form contiguous organoids, we next sought to determine if our custom 3D bioprinting device could introduce multiple cell types within the same linear array. Specifically, we wished to determine if we could generate contiguous, luminal structures composed of alternating cell types. To this end, we printed equally-spaced 200 $\mu$ m linear arrays of alternating red fluorescent protein (RFP) labeled and GFP labeled MCF-12A cells in collagen gels. The RFP and GFP printed cells formed contiguous organoids with a central structure and branched extensions with mixed GFP and RFP cells by day 7 (Fig. 13a). Separating the fluorescent channels of these structures revealed the presence of RFP and GFP labeled cells intermingling with one another within regions of the larger structure and branched processes at Day 9 (Fig. 13b). Indication of coordinated cellular behavior was further supported by positive staining of gap junction protein connexin-32 (Cx32) between RFP and GFP MCF-12A cells along the same lumen (Fig. 13c). This suggests MCF-12A organoid formation does not result from one single founder cell, rather, local MCF-12A cell populations actively participate in the formation of organoid structures. These results also provide evidence of our ability to place more than one cell type (RFP and GFP labeled MCF-12A cells) within close proximity.

### *3.4.6 Bio-Printing in Additional Sources of Collagen ECM*

While rodent derived collagen models recapitulate many features of human mammary gland biology, interspecies variations in ECM composition, organization, density, and function exist<sup>112</sup>. Furthermore, the use of substrata derived from EHS tumors, commercial preparations, or other synthetic scaffolds can suffer from batch to batch variability. Given the ability to standardize the quantity and spatial distribution of MECs in 3D scaffolds, we set to investigate the ability to direct MEC organoid formation in additional sources of ECM using human-derived collagen gels.



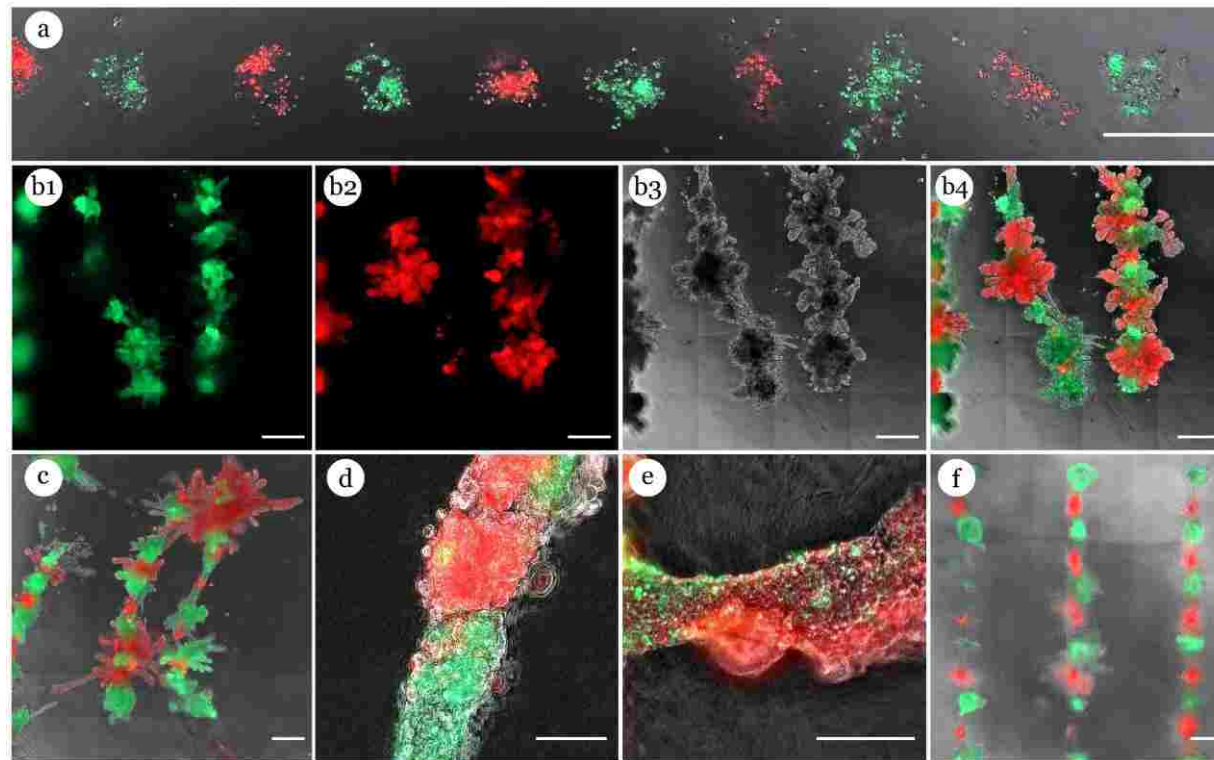


Fig. 14. Alternating RFP/GFP MCF-12A cell deposits in human collagen. (a) 2 days post-printing. Scale bar 250 $\mu$ m. (b) Images of breast epithelial organoids (250 $\mu$ m initial spacing) 7 days post-printing indicating mix of GFP+ and RFP+ cells in the same structure: GFP (b1), RFP (b2), brightfield (b3), and merged (b4). Scale bar 500 $\mu$ m. (c) RFP/GFP structure at 7 days using 500 $\mu$ m initial spacing. Scale bar 500 $\mu$ m. (d) Higher magnification image of RFP/GFP fusion site. Scale bar 50 $\mu$ m. (e) Higher magnification image demonstrating RFP+/GFP+ cells in same 'lobular' structure. Scale bar 100 $\mu$ m. (f) Alternating RFP/GFP cell deposits at 500 $\mu$ m in attached, rat tail collagen gels failed to result in organoid fusion within 14 days. Scale bar 500 $\mu$ m.

To this end, we again printed RFP and GFP labeled MCF-12A cells in 200-500 $\mu$ m linear arrays in human-derived collagen gels (Fig. 14a). After 7 days in culture, RFP and GFP cells within this spacing window were observed to contribute to the formation of large, branched structures (Fig. 14b1-b4). Again, upon closer examination *in situ*, RFP and GFP cells printed at a 500 $\mu$ m spacing were observed intermingling to form a contiguous organoid structure (Fig. 14c,d,e). Data from 9 wells, each containing 60 target locations, indicated a total of 528/540 neighboring organoid fusion events within 7 days post-printing. Further, as a direct comparison, alternating RFP/GFP MCF-12A cells printed 500 $\mu$ m apart in attached rat tail collagen remained isolated and failed to form branched processes (Fig. 14f). These results highlight the ability of 3D bioprinting systems to standardize 3D cell culture assays. Moreover, this standardization process can be used to increase the validity of investigations aiming to determine the effect of various 3D gel-components on cell behavior.

Histological staining of MCF-12A cells printed in human collagen confirmed the presence of GFP and RFP labeled cells within the same lumen (Fig. 15a1-a4). The presence of luminal and basal cell populations was confirmed by positive staining of Ck5 and Ck8 in the bioprinted MCF-12A organoids (Fig. 15b1-b4). Full adhesive function in cell-cell adhesion processes were supported by noting positive expression of cadherins and  $\beta$ -catenin (Fig. 15c1-c4).

Importantly, these results illustrate our bioprinting technique can investigate additional ECM preparations while maintaining consistent cell-deposit numbers and spatial distribution of printed MECs. Additionally, this data suggests our bioprinting platform and associated methods can re-create the unique morphologies observed in attached vs floating gel conditions from manual embedding experiments. Also, these results confirmed the phenomena of MCF-12A organoid fusion is conserved across additional sources of 3D ECM. Together, we believe these results validated our bioprinting methods, and provided valuable insights into the process of MEC organoid formation. Furthermore, given our ability to controllably-deposit multiple cell types in 3D, we believe our bioprinting method possess a greater ability to reproduce a ‘tissue-like’ organization than those found in 3D matrix embedding.

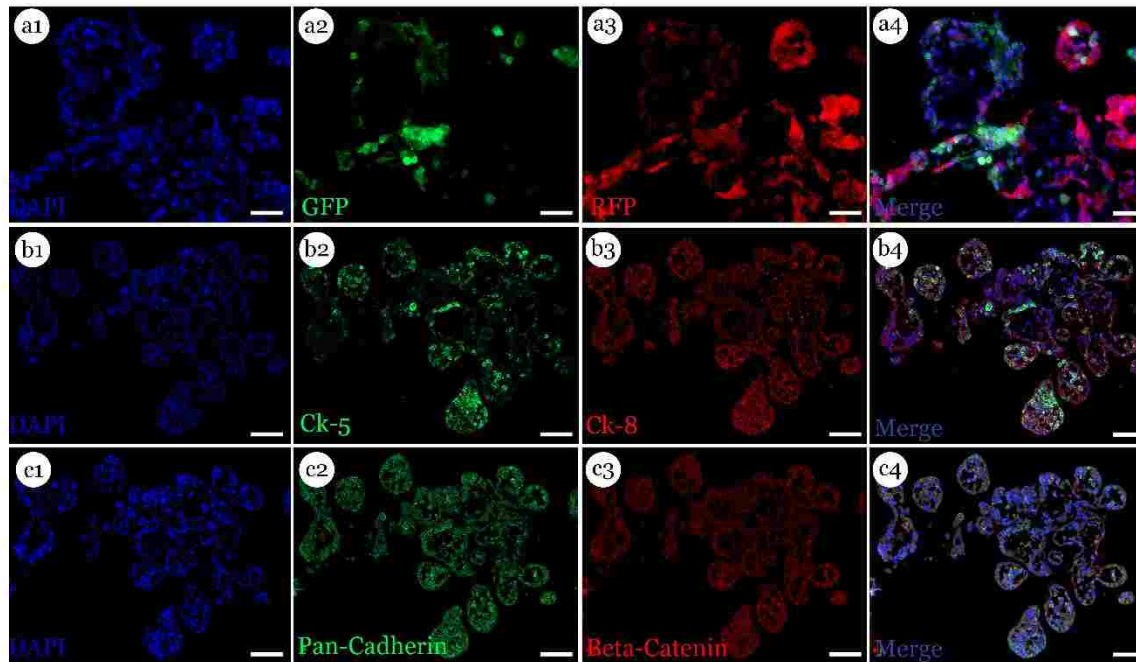


Fig. 15. Immunofluorescent staining of MCF-12A cell organoids in human collagen. DAPI (a1, blue) indicating total cell nuclei, GFP+ cells (a2, green), RFP+ cells (a3, red). Merged image (a4) demonstrates presence of both cell types in the same organoid structure. The presence of Ck-5 (b2, green) and Ck-8 (b3, red) indicate the distribution of ‘luminal’ and ‘basal’ cell populations. Expression of Cadherins and  $\beta$ -Catenin indicate functional cell-cell adhesion throughout the organoid structure. Scale bar 100 $\mu$ m.

### 3.5 Discussion

The quest for understanding development and disease in higher organisms has been hindered by a lack of investigative tools to accurately and repeatedly control the many variables that impact 3D *in vitro* model systems. A profound example of this is evidenced from the disparate results among laboratory-to-laboratory, despite the use of biochemically identical ECM matrices and cell types<sup>55,59,61,62</sup>. In the experiments reported herein, we describe a technique to systematically investigate the extent to which cell-cell and cell-ECM interactions act as regulators of normal epithelial cell differentiation into well-organized structures. By standardizing the number and position of cells inside pre-formed gels, we have developed a method to help standardize the analysis of 3D cultures.

It has been noted that organoids resulting from single, primary epithelial cells vary in morphology and formation efficiency compared to organoids derived from primary epithelial cell clusters<sup>113</sup>. Indeed, we expect the increase in efficiency of our system was due in large part to the ability to define the initial proximity of printed cells. This observation is a likely cause of the high variability in organoid formation rates seen using manual cell-matrix techniques, where individual cell migration within the gel occurs in a random, disorganized manner. In contrast, printed cell aggregates were prone to quickly begin internal organization into cell clusters, which then function as a group to seek out neighboring organoids (Sup. Movie 3.1,3.2). Our quantitative data bolstered this idea as the formation frequency of organoids increased significantly when we crossed a critical cell number threshold. Furthermore, our data suggest reliable control over both initial cell number and organoid spacing permits experimenter directed fabrication of large scale, branched, tubular structures of epithelial origin. These data frame the idea that the quantity of inter-cellular communications, propagated when cells are initially introduced into a foreign 3D environment, can impact the initiation of specific sets of response cascades in developing MEC cell aggregates.

It has been shown that following stable adhesion to ECM components, the mechanical interaction between individual cells and ECM results in the transmission of strain patterns which can extend through hundreds of microns of gel<sup>56-58</sup>. This applied mechanical strain leads collagen fibers to orient along the direction of the strain<sup>59</sup>, which results in increased contact guidance. Furthermore, early studies found a preference for MEC organoids to develop along tension lines between adjacent organoids within collagen gels<sup>60</sup>. In a similar manner to which MECs actively

seek neighboring organoids in 3D gels, we find morphological patterns appear to be associated with the relative position of an individual organoid within the printed array. This may explain our observations that organoids seemed to “sense” neighboring organoids; extending processes preferentially toward neighboring organoids that ultimately lead to organoid fusion and the formation of larger, contiguous structures. Therefore, the ability of this bioprinting method to direct organoid growth by manipulating the distances among initial cell-deposits may be directly related to this phenomenon.

Throughout the past decade, testing and controlling microenvironmental aspects of 3D culture systems has enabled researchers to bridge the gap between traditional 2D cell culture systems and animal models for studying development and tumorigenesis. We used our bioprinting device to derive a set of guidelines to enable reliable formation of large-scale, human mammary epithelial organoids in 3D collagen I gels. These results demonstrate epithelial organoid morphology can be directed by initial cell-deposit number, spacing, and overall print geometry. However, the development of actual tissues cannot be reduced to cellular events alone. ECM synthesis and assembly in the mammary gland is a dynamic and reciprocal relationship between multiple epithelial cell types, myoepithelial cells, adipocytes, endothelial cells, immune cells, and fibroblasts. Where the ECM serves to support and instruct cell behavior, cells also continuously modify and synthesize ECM<sup>112</sup>. Therefore, each breast tumor should be seen as a unique, and complex organ, which continuously evolves as a result of not only specific mutations and genomic instability in individual cancer cells, but also dynamic changes in tumor cell interactions.

The methods described here demonstrate the capability to accurately deposit multiple cell types as neighboring aggregates, which can communicate and synchronize their structure-forming activities. Our approach allows direct control over the generation of *in vitro* constructs large enough for *in vivo* implantation. More importantly, using this system to investigate co-cultures of two or more cell types in a defined microenvironment would greatly increase the ability to develop reliable 3D surrogate models for breast development and carcinogenesis. This is of interest to our group, as we have great interest in understanding how the microenvironment controls differentiation of stem and cancer cells<sup>114-122</sup>. We plan to adapt these protocols for the development of chimeric structures containing cancer and normal epithelial cells as *in vitro* models that mimic our previous *in vivo* findings. Since *in vivo* model systems are costly and complex, our 3D bioprinting technology stands as the obvious choice for developing physiological, 3D model

systems using human cells to create the appropriate contextual cues. Furthermore, we expect the processes outlined here to be easily adaptable to other epithelial cell types, including endothelial cells, to study vascularization and development in other tissue types.

### **3.6 Conclusion**

These data demonstrate that our CNC driven, 3D bioprinter is capable of repeatable and reliable printing of MEC structures. Furthermore, through coordinated cluster placement, our system can generate consistent, large contiguous luminal structures containing more than one cell type. Furthermore, due to the digital transfer of instructional GCODE files, the results of these 3D bioprinting experiments could easily be replicated in other laboratories with a similar 3D bioprinting platform. This paradigm could engender a digitization of biological experimentation that would lead to consistent laboratory-to-laboratory research, improving the ability to progress cancer research-to-cures. Thus, these results indicate we successfully achieved our second objective.

To me life consists simply in this, in the fluctuation between two poles, in the hither and thither between the two foundation pillars of the world.

Hermann Hesse

## CHAPTER 4

### 3D BIOPRINTING CHIMERIC MEC ORGANOIDS

#### 4.1 OVERVIEW

A mounting body of evidence suggests the context and status of cellular interactions within the microenvironment are a key determinant of whether cells within a tissue retain their normal architecture or undergo tumor progression<sup>26,123,124</sup>. This conclusion was largely made evident through co-culturing stroma from one type of tissue with epithelial cells from a different tissue, frequently known as chimeric models<sup>26,125-127</sup>. *In vivo*, chimeric-recombination models first identified the unique ability of tissue stroma to influence the developing epithelium<sup>128</sup>. For example, when mammary epithelium was recombined with salivary gland mesenchyme, structures that resembled salivary gland epithelium were generated<sup>129</sup>. Additionally, salivary epithelium outgrowths in contact with mammary mesenchyme resembled a mammary gland ductal tree, became competent for lactation, and responded to hormonal stimuli<sup>130</sup>. Astonishingly, it has been demonstrated that the regenerating mouse mammary gland can reprogram testicular cells, neural progenitors, bone marrow and breast cancer cells to adopt a normal mammary progenitor cell fate<sup>114,116,128,131,132</sup>. These studies revealed the highly malleable status of the epithelial component and the importance of the *in vivo* components of the gland for tissue function and cell fate.

While the accrual of these results highlights the need to investigate the identities and molecular mechanisms involved in this process, it is much more challenging to directly and non-invasively image tumor-cell interactions as they begin to occur *in vivo*. Furthermore, identifying aspects of these mechanisms has been problematic because it is difficult to isolate the effects of an individual stimulus on cell behavior *in vivo*. Additionally, it should be noted that while gland reconstitution studies have been able to identify the regenerative capacity of the mammary stem

cell, gland reconstruction likely involves injection site wounding, which may induce different fate decisions than those occurring during normal gland development<sup>3</sup>. Also, these investigations lack sufficient methods for maintaining cells in close proximity once implanted *in vivo*<sup>22,24,133,134</sup>.

In an effort to study these systems in a more definable space, *in vitro* 2D cell culture has traditionally been employed. Yet, 2D cell cultures are largely non-biomimetic, and as a result, cell-signaling networks are altered in 2D environments. Many investigations have illustrated 3D architectures are necessary to elicit the functional organization and cellular relationships of the *in vivo* environment<sup>51</sup>. For these reasons, 3D *in vitro* and *ex vivo* cell culture systems represent an indispensable tool to investigate the processes related to tissue and tumor formation. However, previous models of 3D tumor biology, such as tumor organoids, are incapable of fully addressing the developmental cues associated with the human cancer ecosystem. Therefore, these systems are becoming increasingly complex by the incorporation of additional cell types. Co-cultures of stromal and tumor cells, and even tri-cultures of MECs, human fibroblasts and adipocytes have been developed to elicit a physiologically relevant, 3D culture surrogate of complex human breast tissue<sup>135-137</sup>.

3D *in vitro* co-cultures of stromal and tumor cells, and even tri-cultures of MECs, human fibroblasts and adipocytes have been developed to elicit a physiologically relevant, 3D culture surrogate of complex human breast tissue<sup>61,135-138</sup>. Importantly, these *in vitro* investigations have been able to show that restoring the correct level of microenvironmental signaling can ‘revert’ the malignant phenotype of breast tumor cells, despite the complete retention of the malignant genome<sup>63,139-142</sup>. For example, by screening seven BRAF<sup>V600E</sup> mutant melanoma cell lines with 18 stromal cell lines, researchers uncovered a novel mechanism of vemurafenib resistance mediated by secretion of hepatocyte growth factor by six of the co-cultured stromal cell lines<sup>143</sup>. Thus, there exists a growing need to develop advanced 3D cell culture models comprised of multiple cell types to decrypt aspects of intra- and intercellular signaling, and the context-driven contributions of nongenetic sources of the *in vivo* environment.



## 4.2 Introduction

Despite the incorporation of additional cell types in 3D culture models, many components of the *in vivo* microenvironment remain a mystery. This shortcoming may be related to the limited availability of suitable technological and analytical methods to investigate these<sup>144</sup>. For example, the standard 3D culture procedures utilized by many of these investigations rely on randomly mixing ratios of cells with ECM substrates prior to gelling, or by seeding cell mixtures on top of a pre-formed ECM gel. Therefore, the size and morphology of resulting organoids vary greatly, which leads to difficulty in interpreting and reproducing experimental results<sup>145</sup>.

One potentially controllable, yet major source of the variability of current 3D culture systems stems from the manual cell-matrix embedding methods that yield a random distribution of cells in the gel. Advances in 3D cell culture technologies, especially accessible 3D bioprinting devices, have recently demonstrated the ability to reliably, and repeatedly generate arrays of small-volume, cell-deposits containing user-specified cell numbers ranging from 1 to hundreds, with spatial resolutions below  $50\mu\text{m}$ <sup>108</sup>. Furthermore, these devices have demonstrated the ability to fabricate, large-scale epithelial organoid-structures. Herein, we describe the first example of 3D bioprinting technology to facilitate chimeric structure formation between non-tumorigenic human MECs (MCF12A) and either of two human tumorigenic cell lines: luminal epithelial mammary cell line MCF-7 and metastatic adenocarcinoma mammary breast cancer cell line MDA-MB-468 in a 3D collagen gel system.

We demonstrate how this technology not only promises to standardize 3D culture assays, but also provides an efficient method to introduce additional cell types into developing and previously-established MEC organoid structures. Principal findings indicated a significantly enhanced ability to generate chimeric organoids as compared to matrix embedding methods. Both MCF-7 and MDA-MB-468 cells survived and incorporated into MCF-12A organoids to form chimeric structures. Additionally, the morphological behaviors of both tumorigenic cell lines inside chimeric structures was unlike those in control (tumor-only) structures. Histological staining indicated tumor cells expressed cadherin and connexin proteins on borders with MCF-12A cells in chimeric structures, suggesting the two cell types formed adherens junctions and gap junctions under these conditions. Interestingly, by immunofluorescence, both tumorigenic cell lines in chimeric structures exhibited  $\beta$ -catenin staining similar to adjacent MCF-12A cells. Furthermore,

by using human derived ECM substrates, our 3D bioprinting system offers an innovative platform for generating a fully human, *in vitro* model to dissect cell-cell interactions, the effects of microenvironment on cell function, and the effects of different genetic or non-genetic modifications on mammary cell transformation. These findings are, to the best of our knowledge, the first demonstrations of the capacity of 3D bioprinting devices to mediate and direct the formation of chimeric MEC organoid-structures in fully human, 3D culture environment.

### 4.3 Materials and Methods

#### 4.3.1 Cell Culture

Immortalized non-tumorigenic human breast epithelial cell line, MCF-12A, and MCF-7 and MDA-MB-468 breast carcinoma cell lines were purchased from ATCC. All cells were maintained on 2D tissue culture plastic. MCF-12A cells were initially cultured in 2D on tissue culture plastic in a 75 cm<sup>2</sup> flask supplemented with a 1:1 mixture of Dulbecco's modified Eagle's medium and Ham's F12 medium (DMEM/F12), 5% Horse Serum, 20 ng ml<sup>-1</sup> hEGF, 0.01 mg ml<sup>-1</sup> bovine insulin, 500 ng ml<sup>-1</sup> hydrocortisone and 1% ABAM (all purchased from ThermoFisher). MCF-7 and MDA-MB-468 cells were maintained in Dulbecco's Modified Eagle's Medium supplemented with 10% fetal bovine serum (FBS, Life Technologies) and 1% ABAM. All cells were cultured at 37.0°C and 5.0% CO<sub>2</sub>. After confluence, the cells were dissociated using TrypleE (ThermoFisher) and collected by centrifugation. Chimeric organoids were cultured using 1:1 mixture of Dulbecco's modified Eagle's medium and Ham's F12 medium (DMEM/F12), 5% Horse Serum, 20 ng ml<sup>-1</sup> hEGF, 0.01 mg ml<sup>-1</sup> bovine insulin, 500 ng ml<sup>-1</sup> hydrocortisone and 1% ABAM (ThermoFisher).

MCF-12A cells are considered a model for normal human MECs. The MCF-7 cell line represents a rapidly growing, luminal carcinoma cell line that is E-cadherin positive, vimentin negative, estrogen receptor-positive, and non-invasive<sup>146</sup>. MDA-MB-468 cells are EGF receptor rich, estrogen receptor-negative, and due to two shortened  $\alpha$ -catenin transcripts, lack functional  $\alpha$ -catenin<sup>147,148</sup>.

### 4.3.2 Preparation of 3D Collagen ECMs for Bioprinting and Manual Cell-Matrix Embedding

For manual cell-matrix embedding studies, single cell suspensions of MCF-12A cells were mixed with neutralizing solution and acidified rat tail collagen I (Corning) as specified by the manufacturer, to a final concentration of 1.3 mg/ml. For chimeric studies, MCF-12A cells were mixed with one of the two tumorigenic cell lines at a 1:5 ratio. Immediately after mixing, 500 $\mu$ l of neutralized collagen I gel material containing approximately 5000 cells (6000 cells for chimeric studies) was dispensed into a 24 well plate and allowed to solidify and adhere to the surfaces of the well for 1 hour in a laboratory incubator at 37.0°C and 5.0% CO<sub>2</sub>. After gelation (solidification), 500 $\mu$ l of cell appropriate cell media was added to the wells. MCF-12A media was used for all chimeric studies. Subsequent media changes were performed every 3 days.

VitroCol, human collagen I solution (Advanced BioMatrix), was prepared according to manufacturer's recommendation to a final concentration of 1.0 mg/ml. For all printing experiments, a minimum of 500 $\mu$ l of collagen gel was dispensed into individual wells of a 24 well plate and allowed to solidify for 1 hour in a laboratory incubator at 37.0°C and 5.0% CO<sub>2</sub>.

### 4.3.3 Bioprinting System

A previously developed bioprinting system was used to robotically dispense cells into specified 3D locations of a polymerized collagen gel<sup>108</sup>. Briefly, neutralized collagen I gel material was dispensed into a 24 well plate and allowed to solidify and adhere to the surfaces of the well in a laboratory incubator at 37.0°C and 5.0% CO<sub>2</sub>. Before printing operations, 2D cultures of MCF-12A, MCF-7 and MDA-MB-468 cells were dissociated into single cells using TrypleE (ThermoFisher), centrifuged at 300 $\times$ g, and re-suspended in media to obtain a final 'ink' concentration of 60 $\times$ 10<sup>4</sup> cells ml<sup>-1</sup>. For chimeric experiments, printing operations were optimized to extrude specified numbers of cells inside the collagen I gel via a CNC insertion routine which deposited cell containing media at a specified 'target' location inside the polymerized collagen I gel. Users specified intended wells of commercially available tissue culture plates, printing locations, distances among printing locations, and the number of cells per target location. The experiment information was automatically converted into G-code, loaded into Repetier Host, and sent to the three-axis microcontroller of the bioprinter. The bioprinting system was located inside

a benchtop biosafety cabinet during all printing operations. The heated print bed was set to 37° for all printing operations.

#### *4.3.4 Characterization of Organoid Growth and Morphology*

Immediately after printing, the initial quantity of printed cells was verified using manual counting and image analysis using ImageJ and Matlab. Post-printing, cells were monitored up to 21 days using a combination of bright field imaging/fluorescent imaging using a Zeiss axio-observer Z1 fluorescent microscope, or time-lapse imaging using a Lumascope 620 microscope. The size of organoids was determined by analyzing bright-field images taken daily for each experimental condition using ImageJ. Within this investigation, organoids were operationally defined as a cluster of cells with no clear cell-cell boundaries, or the inability to discern individual cells from neighboring cells. The organoid formation rate for manual matrix embedding was calculated using the following equation: (number of organoids per well / number of cells seeded per well) ×100%. The organoid formation rate for bioprinted organoids was calculated using the following equation: (number of organoids per well / number of printed target sites) ×100%.

#### *4.3.5 Immunofluorescence Staining*

Gels were fixed in 10% neutral buffered formalin, paraffin embedded and sectioned. Sections were prepared for staining by deparaffinizing in a xylene substitute, rehydration, and heat-mediated antigen retrieval using pH 9 tris-edta with 0.05% tween 20. Sections were blocked in 10% goat serum and incubated with primary antibodies in a humidified chamber at 4°C overnight. Secondary antibodies were added for 1 hour at room temperature. Sections were counterstained with DAPI.

Antibodies were used at the following concentrations: mouse monoclonal antibody to BetaCatenin [12F7] (1:50; ab22656, Abcam), anti-green fluorescent protein rabbit IgG Alexafluor 488 conjugated ( 1:75; Invitrogen A21311); rabbit monoclonal antibody to cytokeratin 5 [EP1601Y] (1:75; ab52635, Abcam), mouse monoclonal antibody to cytokeratin 8 [C-51] (1:35; ab2531, Abcam), rabbit anti-pan-cadherin (1:75; 71-7100, ThermoFisher), rabbit polyclonal antibody to GJB6 [Cx30] (1:25; HPA014846, Sigma-Aldrich), and rabbit polyclonal antibody to

GJB1 [Cx32] (1:25; HPA010663, Sigma-Aldrich). Appropriate Alexafluor 488 and 568 conjugated goat antibodies (1:1000; ThermoFisher) were used for secondary antibody labeling. All sections were counterstained with DAPI and imaged using a Zeiss axio-observer Z1 fluorescent microscope.

#### *4.3.6 Statistical Analysis*

Values represent mean  $\pm$ standard deviation of samples measured in triplicate. Data represent more than three independent experiments. Results were assessed for statistical significance using Student's *t* test. Differences were considered statistically significant at  $*p < 0.05$ .

## **4.4 Results**

### *4.4.1 Reliable Generation of Mammary Epithelial Tumor Organoids*

To establish baseline behaviors of MCF-7 and MDA-MB-468 cells in 3D collagen cultures, we first employed our bioprinting device to generate arrays of tumor cells in polymerized collagen gels. Our bioprinting method utilized CNC processes to controllably-deposit cells in 3D locations of polymerized collagen I gels (Fig. 16a1,b1). Results indicated both tumor cell lines proliferated and formed structures post-printing (Fig. 16a1-a4,b1-b3). Our bioprinting assay identified a discrepancy between the growth morphologies of the two tumor cell lines throughout the 21-day culture period. MCF-7 tumor cells formed compact, sphere-like structures with little evidence of coordinated growth among neighboring organoids, indicative of their previously known, non-invasive character (Fig. 16c). On the other hand, MDA-MB-468 cell growth illustrated the opposite effect, where invasive tumor cells equally dispersed into all radial directions of the Collagen I matrix, which resulted in a large, disordered structure lacking defined boundaries (Fig. 16d). H&E sectioning of bioprinted arrays confirmed cell free regions between MCF-7 print locations, which supports the notion that MCF-7 cells do not readily migrate through collagen I

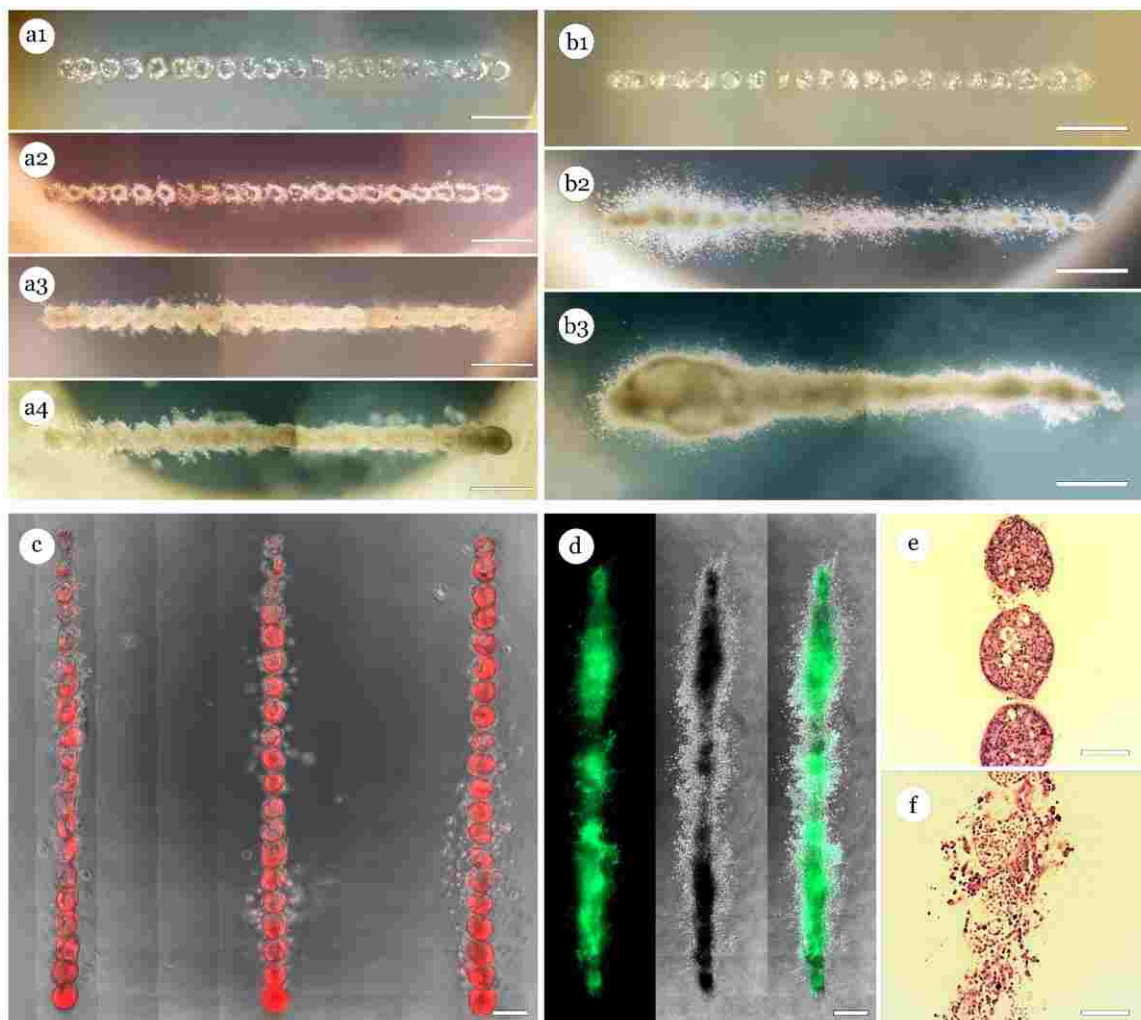


Fig. 16. 3D Bioprinting consistent breast tumor organoids. (a1-4) MCF-7 cell deposits (40 cells/deposit) spaced  $300\mu\text{m}$  apart at 1, 7, 14, and 21 days post-printing. Scale bar 1 mm. (b1-b3) MDA-MB-468 cell deposits (40 cells/deposit) spaced  $300\mu\text{m}$  apart at 1, 14, and 21 days post-printing. Scale bar 1 mm. Reliable formation of (c) MCF-7 and (d) MDA-MB-468 tumor organoids at 21 days. Scale bar  $500\mu\text{m}$ . H&E stain of (e) MCF-7 and (f) MDA-MB-468 tumor organoids at 21 days. Scale bar  $150\mu\text{m}$ .

(Fig. 16c,e). The opposite effect was confirmed in sections of arrays containing MDA-MB-468 cells, where cells and small cell clusters appear dispersed throughout the gel (Fig. 16d,f).

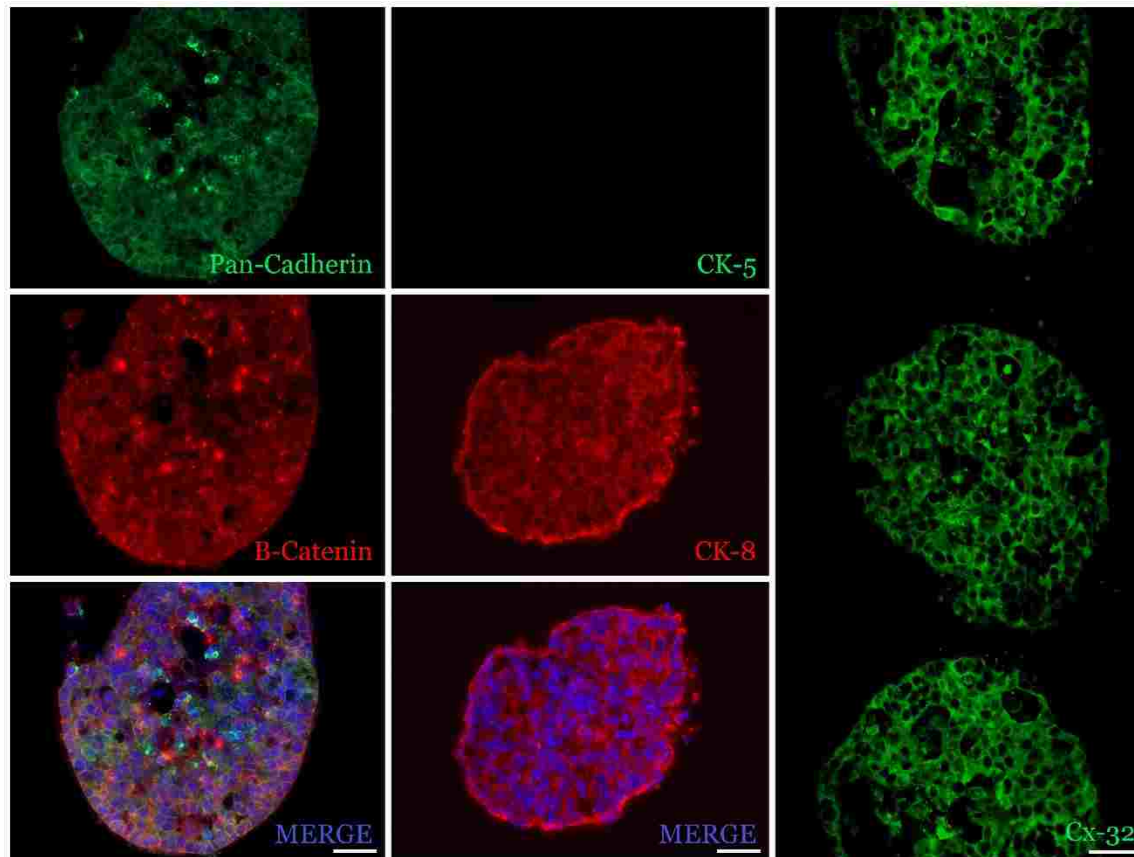


Fig. 17. Histological analysis of bioprinted MCF-7 breast tumor organoids. MCF-7 cell organoids exhibited weak cadherin, and  $\beta$ -catenin staining. Ck-5 was not detected among MCF-7 cells, however MCF-7 cells were Ck-8 positive. Expression of Cx-32 was observed. Scale bar 50 $\mu$ m.

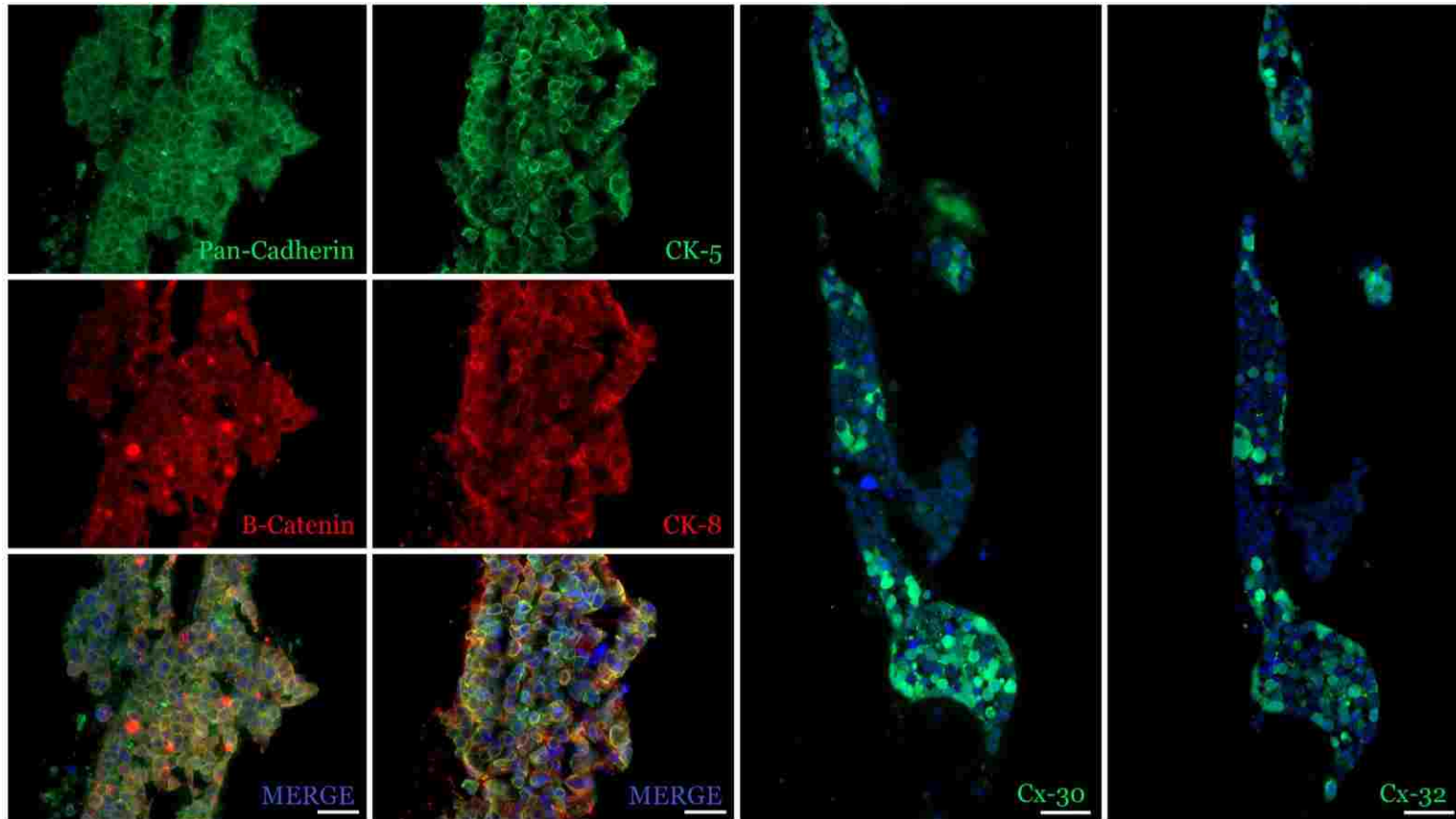


Fig. 18. Histological analysis of bioprinted MDA-MB-468 breast tumor organoids. Cadherin and  $\beta$ -catenin staining in MDA-MB-468 tumor cell organoids. MDA-MB-468 tumor organoids were Ck-5 and Ck-8 positive. Variable expression of Cx-30 and Cx-32 was observed. Scale bar 50 $\mu$ m.



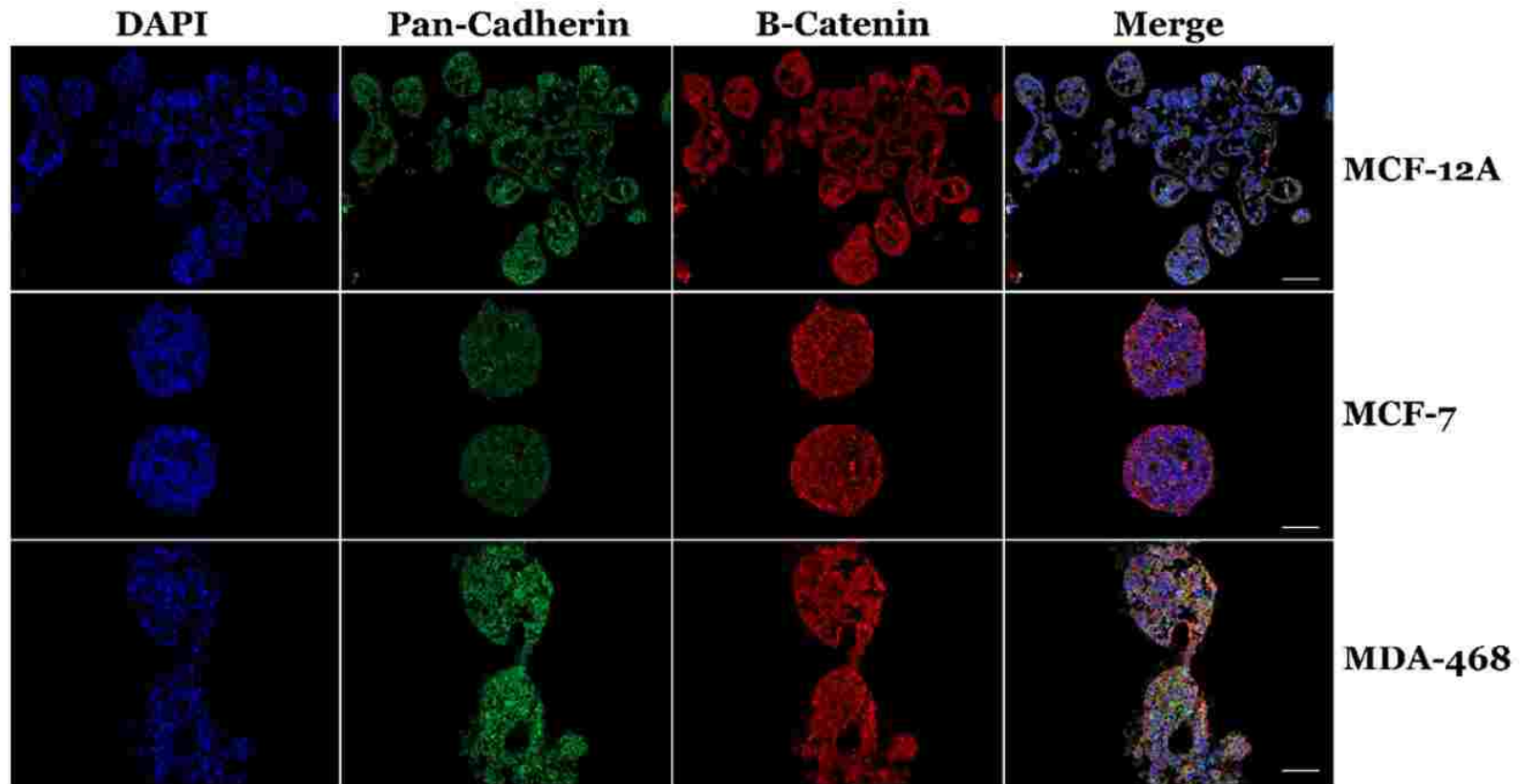


Fig. 19. Comparison of 3D bioprinted, epithelial organoid-structures. MCF-12A cells form epithelial organoids with a luminal cavity, express Pan-Cadherin, and express  $\beta$ -Catenin. Tumorigenic cell-organoids from MCF-7 cells displayed less intense Pan-Cadherin signal and were  $\beta$ -Catenin positive. Tumorigenic cell-organoids from MDA-MB-468 cells express cadherin and  $\beta$ -Catenin. Scale bar 100 $\mu$ m.

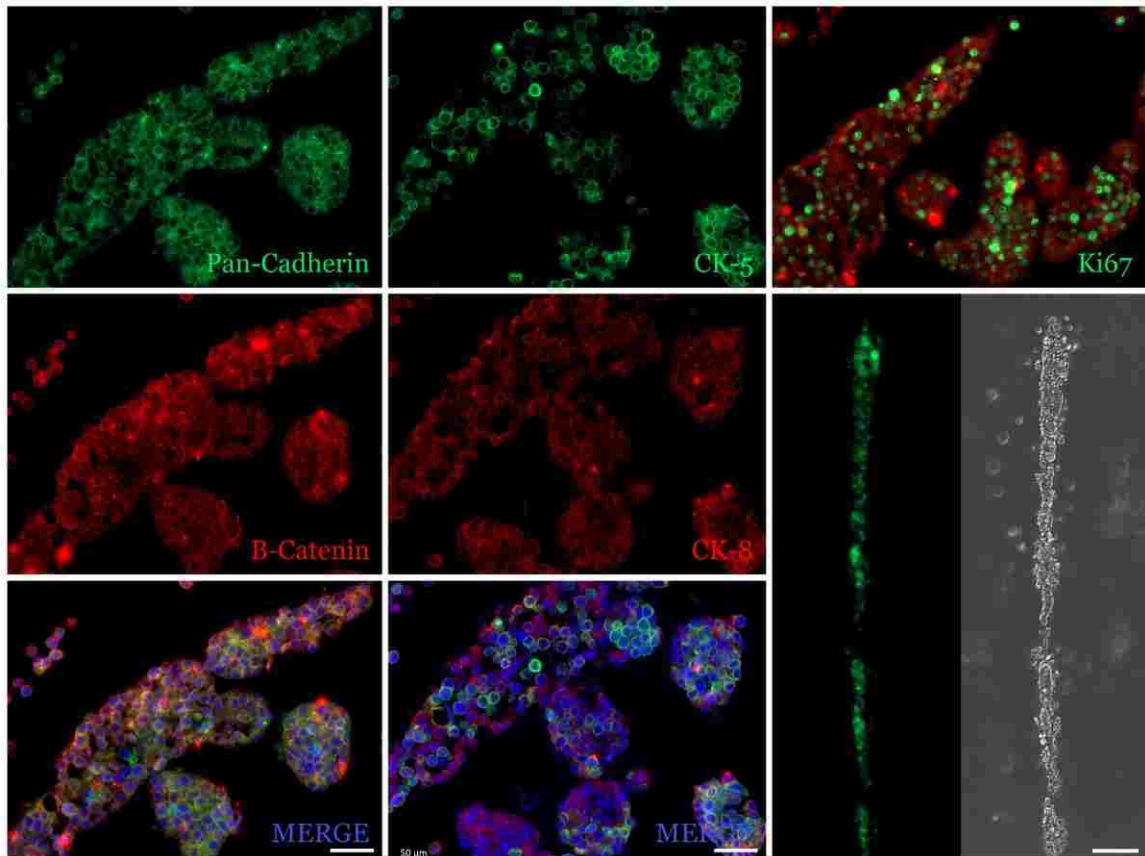


Fig. 20. Collagen density affects morphology of MCF-7 organoid structures. Immunohistochemical analysis of 3D bioprinted, MCF-7 tumor organoids in 0.5 mg/ml collagen gel indicated MCF-7 organoid-structures under these conditions were cadherin and  $\beta$ -Catenin positive, and express both Ck-5 and Ck-8. Lower density collagen gels increased the ability of 3D bioprinting to direct MCF-7 organoid fusion. Scale bar 50 $\mu$ m.

To further illustrate the ability of our bioprinting device to standardize 3D culture assays, we printed MCF-7 cells in 0.5 mg/ml collagen gels (Fig. 20). In the 0.5 mg/ml collagen gel, around MCF-7 cells expressed myoepithelial marker Ck5 (Fig. 20), whereas no staining was observed in 1.0 mg/ml gels (Fig. 17), suggesting that luminal and basal specific markers were co-expressed in the cells grown in the less dense collagen. However, MCF-7 cells were still Ki67 positive in 0.5 mg/ml collagen gels, which suggests the cells still retained a highly proliferative phenotype (Fig. 20). However, reducing the density of the collagen matrix resulted in the opposite growth morphology seen in (Fig. 16c). While MCF-7 cell organoids in 1.0 mg/ml collagen were unable to reliably undergo coordinated organoid fusion within 7 or 14 days, individual MCF-7 cell-organoids were able to fuse within 5 days post-printing in the less dense 0.5 mg/ml collagen gel (Fig. 20). These data suggest that MCF-7 cell behavior differs among different culture conditions and highlights the ability of bioprinting devices to standardize the comparison of experimental results through the reliable patterning of cell quantities.

#### *4.4.2 Proliferation in MCF-12A, MCF-7, and MDA-MB-468 Cells.*

To provide a better understanding of the differences between MCF-12A cells and tumorigenic cell lines in collagen gels, we used manual scoring methods to assess for differences in levels of proliferation by immunostaining for a proliferating-cell antigen, Ki67. Compared to normal MCF-12A cell structures (Fig. 21a), the number of proliferating epithelial cells was significantly higher in tumorigenic MCF-7 ( $*p < 0.01$ ) (Fig. 21b,d) and MDA-MB-468 cell structures ( $**p < 0.005$ ) (Fig. 21c,d). This confirmed the highly proliferative status of both tumorigenic cell lines as compared to normal MCF-12A cells.

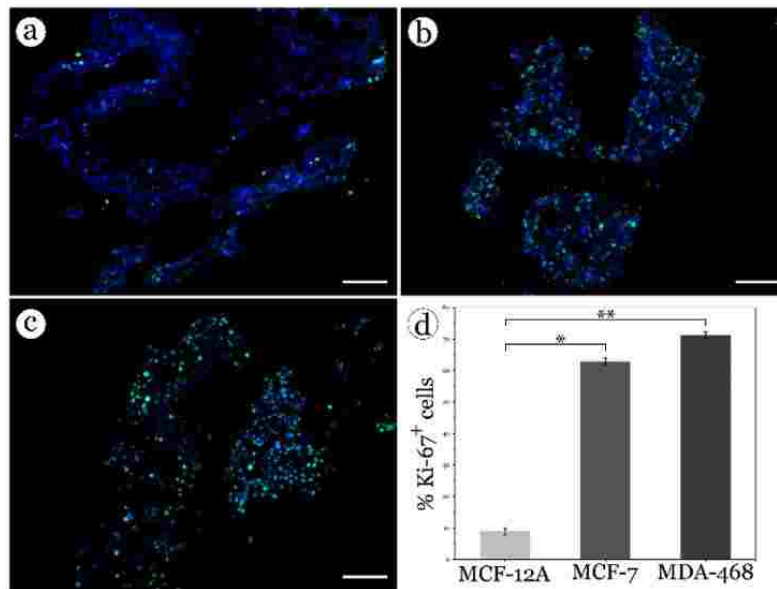


Fig. 21. Quantitative analysis of Ki-67 positive epithelial cells grown in 1.0 mg/ml collagen gel. (a) MCF-12A, (b) MCF-7, (c) MDA-MB-468 stained for Ki-67 (GFP) and nuclear stain DAPI. Scale bar 100 $\mu$ m. (d) Compared to MCF-12A cell-organoids, tumor-organoids contain significantly higher numbers of proliferating cells in collagen gels. \* $p < 0.01$ ; \*\* $p < 0.005$ .

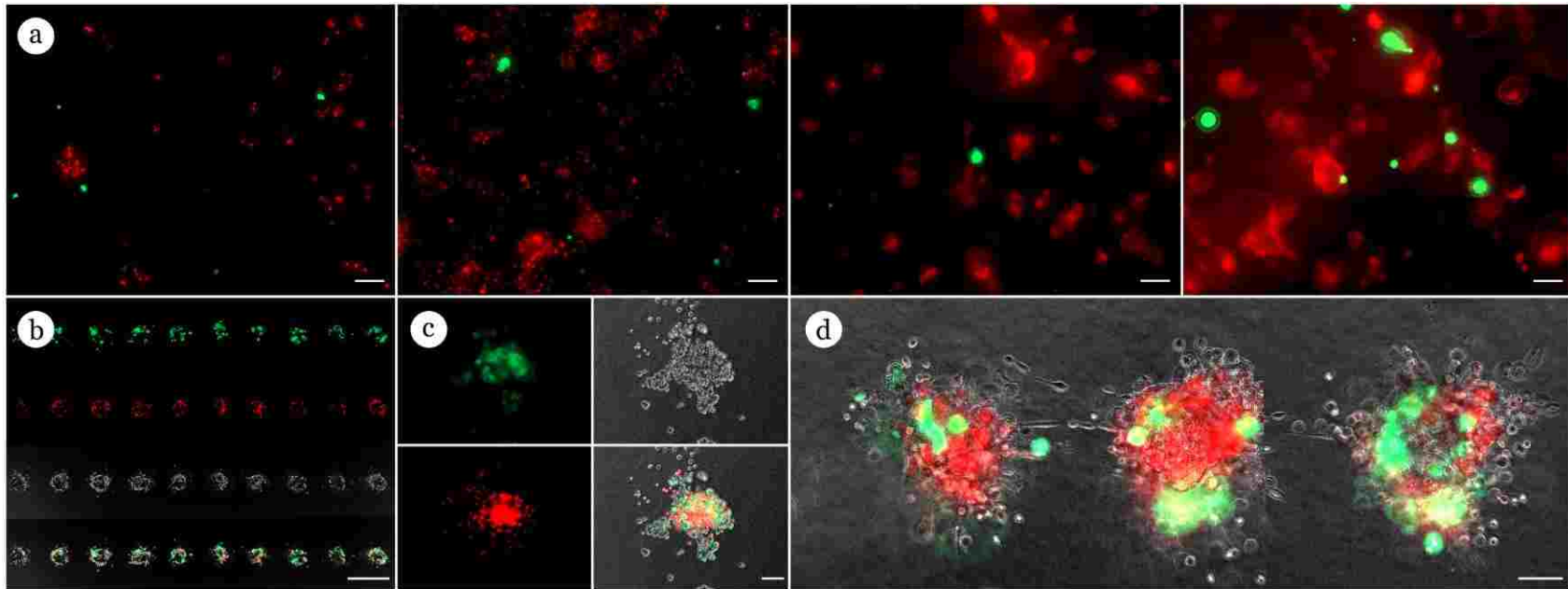


Fig. 22. Bioprinted multicellular assays are more efficient than manual method. (a) Results from manual method at 1, 3, 7, and 14 days in culture. Scale bar 200 $\mu$ m. Unlike the random cell distribution in manual methods, 3D bioprinted tumorigenic cells are immediately exposed to normal MECs. (b) Day 1 result of bioprinted mixture of GFP labeled, tumorigenic cells (MDA-MB-468) and RFP labeled MCF-12A cells. Scale bar 100 $\mu$ m. (c) Day 3 results of bioprinted tumorigenic (GFP) and normal (RFP) MEC cells. Scale bar 50 $\mu$ m. (d) By day 5, tumorigenic cells were exposed to neighboring MCF-12A cell-organoid interactions. Scale bar 50 $\mu$ m.

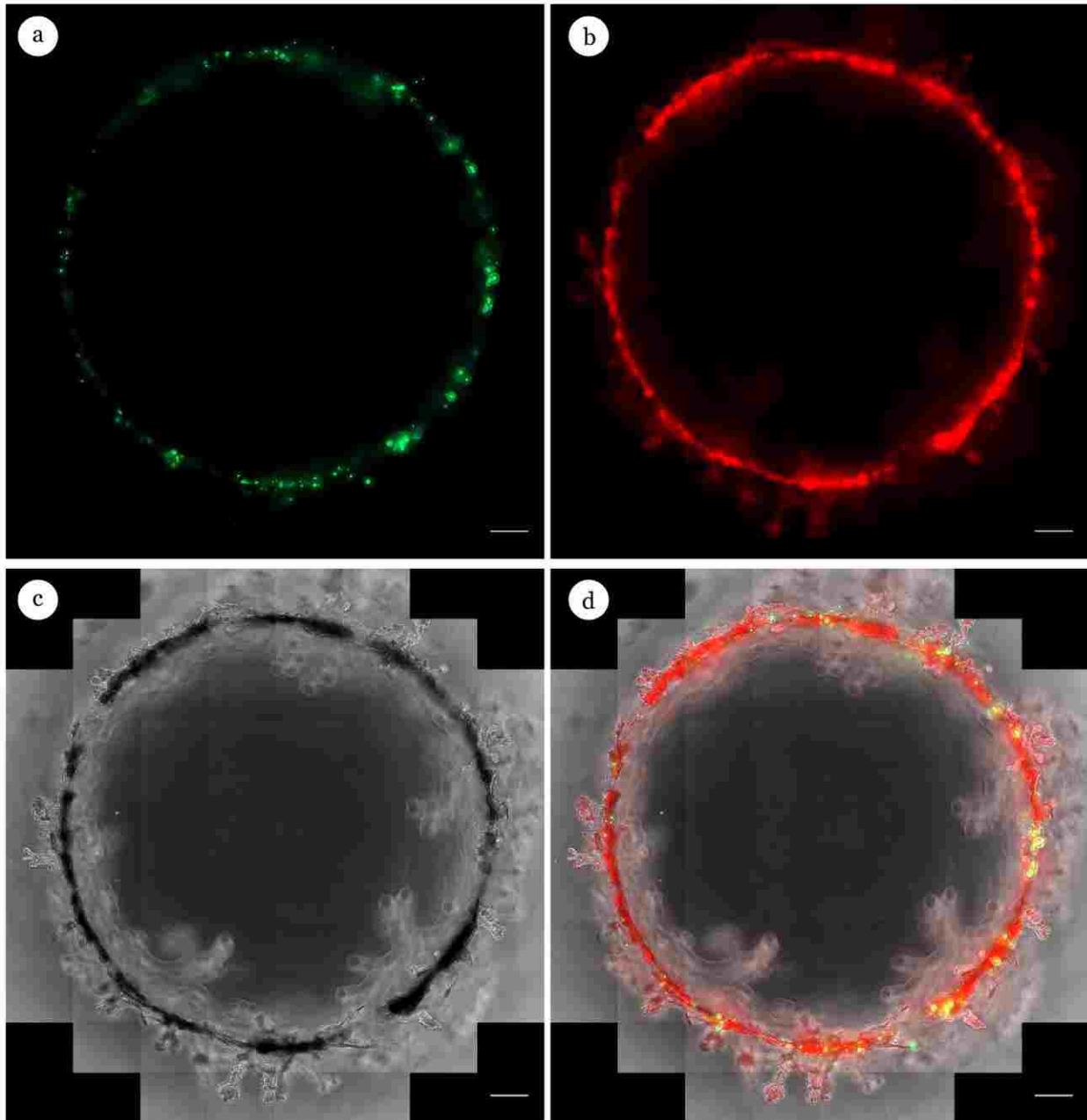


Fig. 23. Within 7 days, 3D bioprinting enabled the reliable formation of large chimeric mammary epithelial organoid-structure containing (a) tumorigenic cells (MDA-MB-468) and (b) 'normal' MCF-12A cells. (c) Organoid -structure illuminated with brightfield. (d) Merged image demonstrating the presence of both cell types in organoid-structure. Scale bar 500 $\mu$ m.

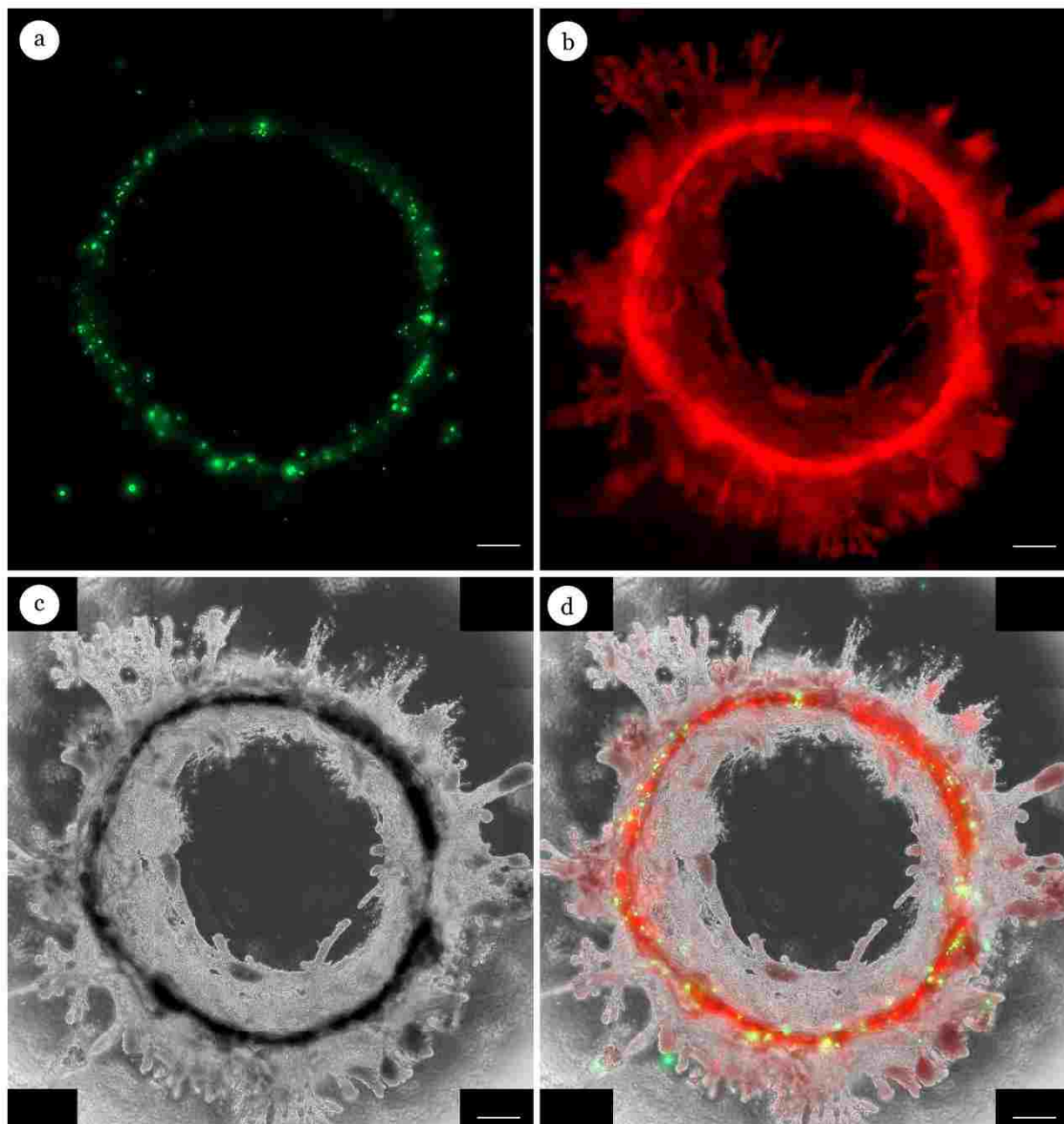


Fig. 24. Within 21 days, initial mixtures of ‘normal’ MCF-12A cells and tumorigenic cells MDA-MB-468 undergo coordinated organoid fusion events to generate a large chimeric epithelial organoid-structure. Example of (a) tumorigenic cells (MDA-MB-468) located among (b) ‘normal’ MCF-12A cells. (c) Organoid -structure illuminated with brightfield. (d) Merged image demonstrating the presence of both cell types in organoid-structure. Scale bar 500 $\mu$ m.

#### 4.4.3 Generation of Chimeric Structures in a 3D Gel

Given the need to develop high-throughput, *in-vitro* models to investigate the role of the microenvironment on epithelial biology in 3D, we began by determining the effectiveness of manual cell-matrix embedding to generate chimeric cell-organoids (Fig. 22a). Consistent with previous *in vivo* demonstrations, our *in vitro* chimera studies used a 5:1 ratio of normal to tumorigenic cells<sup>128</sup>. Thus, 1000 cells from a single tumorigenic cell line were mixed with 5000 MCF-12A cells, added to unpolymerized collagen I gels and pipetted into wells of a 24 well plate. Under these conditions, MECs and tumorigenic cell lines were able to generate chimeric organoid structures during the 21-day culture period (Fig. 22a). However, there were severely limiting quantities of chimeric organoids, further complicated by the excessive number and random distribution of MCF-12A organoid-structures.

Having visually identified chimeric tumorigenic cells in MCF-12A organoids, we next sought to guide the formation of chimeric organoids using our custom bioprinting system. We previously described our ability to standardize the frequency of organoid formation through control of the initial cell quantities within bioprinted cell-deposits; cell-deposits containing at least 40 cells formed organoids within 7 days post-printing (Fig. 9). Using this 40-cell standard, we dispensed a 5:1, MCF12A to cancer cell mixture at volumes equivalent to 40 cells in equally-spaced linear arrays inside collagen I gels. Unlike the random cell distribution of manual embedding, our bioprinting method maintained GFP-labeled tumorigenic cells within the immediate vicinity of RFP-labeled MCF12A cells post-printing (Fig. 22b). After 3 days, both GFP-labeled tumorigenic cell lines showed signs of initial cell-cell clustering associated with developing MCF-12A organoid structures (Fig. 22c). Within 5 days, we observed behavioral discrepancies between the two tumor types in the RFP-MCF-12A organoids. GFP-labeled MDA-MB-468 tumorigenic cells were often found equally dispersed, in single cell quantities throughout RFP-MCF12A organoid-structures (Fig. 22d).

After 1 week in collagen gels, bioprinted cell clusters containing normal and tumorigenic cell types fused with neighboring organoids into large-epithelial organoid-structures with branched extensions directed into unoccupied areas of the gel (Fig. 23a-d). Interestingly, time-lapse imaging indicated both MCF-7 and MDA-MB-468 tumorigenic cell lines interact with MCF-12A cells, and actively migrate inside MCF-12A organoids (Sup. Movie 4.1, 4.2). After 3 weeks in culture, the



cell clusters formed into large, contiguous epithelial- structures, containing chimeric constituents from both cancer cell lines (Fig. 24a-d). Importantly, as these structures began to generate branched extensions, tumor cells remained equally dispersed within the networked structures (Fig. 24a). Together, these results indicate our bioprinting process effectively generates chimeric structures, which holds the potential to mimic the incorporation of cancer cells within normal mammary structures previously described *in vivo*. These findings indicate our bioprinted chimeric structures represent the state of the art system for studying not only cancer cell redirection, but also studies of MEC tissue morphology, and the developmental processes associated with generating the hollow structures similar to ducts seen *in vivo*.

#### 4.4.4 Quantification of Chimeric Organoid Formation

Surveys of manually-embedded gels indicated the initial 5000 MCF-12A cell-quantity resulted in a total of  $929 \pm 265$  and  $1060 \pm 209$  MCF-12A organoids at 7 and 14 days. Given the 1:5 ratio of tumorigenic cells in the initial cell mixtures of chimeric experiments, we expected to observe tumorigenic cells among 200 of the 1000 MCF-12A organoids in the embedded gels. Yet, among these organoids, only  $2.3 \pm 0.5$  and  $5.5 \pm 1.3$  chimeric organoids were observed at 7 and 14 days, respectively (Table 2). Thus, generating chimeric organoids using manual embedding equaled a success rate of 1.15% and 2.75% at 7 and 14 days, respectively (Table 2).

Chimera Organoid Formation		
	Cells/Well	Expected
Manual	5000	166
Bioprinter	1080	36
	D7	D14
Manual	2.3 ±0.5	5.5 ±1.3
Bioprinter	34.7 ±1.6	32.2 ±3.8
Chimera Formation Frequency		
Manual	1.15±0.5	2.75±1.3
Bioprinter	96.4±1.6**	89.5±3.8*

Table 2. Evaluation of chimeric organoid formation. Compared to manual cell embedding, 3D bioprinted cell mixtures form significantly more chimeric organoid-structures. \*\* $p < 0.001$ ; \* $p < 0.01$ .

Among experiments with 36 bioprinted cell-deposits,  $34.7 \pm 1.6$  and  $32.2 \pm 3.8$  chimeric cell-organoids formed at 7 and 14 days, respectively (Table 2). Thus, bioprinted cell mixtures corresponded to a 96.4 % and 89.5 % chimeric organoid formation frequency at 7 and 14 days. When compared to manual methods, the number of bioprinted chimeric organoids increased significantly after both 1 week (\*\* $p < 0.001$ ) and 2 weeks (\* $p < 0.01$ ) (Table 2). Overall, this data highlights the increased efficiency of our 3D bioprinter to generate chimeric organoid-structures compared to manual matrix embedding procedures.

#### *4.4.5 Distribution of Junctional Proteins in Chimeric Organoids*

We next aimed to characterize the chimeric structures to determine their behavior when introduced into mammary epithelial organoids. To do this we immunoassayed slides using antibodies for tumorigenic cells (anti-GFP) confirming the presence of tumorigenic cell types inside MCF-12A organoids (Fig. 25). Cadherin staining indicated both MCF-7 and MDA-MB-468 cells express cadherins in chimeric organoids (Fig. 26).

Positive staining of gap junction proteins Cx30 and Cx32 between tumorigenic and MCF-12A cells in chimeric organoids suggest tumorigenic cells may form gap-junctions with MCF-12A cells in chimeric organoids (Fig. 23). These results indicate maintaining the two cell types in close proximity is effective for generating chimeric organoids, and also provide evidence of cell-cell interactions among both tumorigenic cell lines and MCF-12A cells.

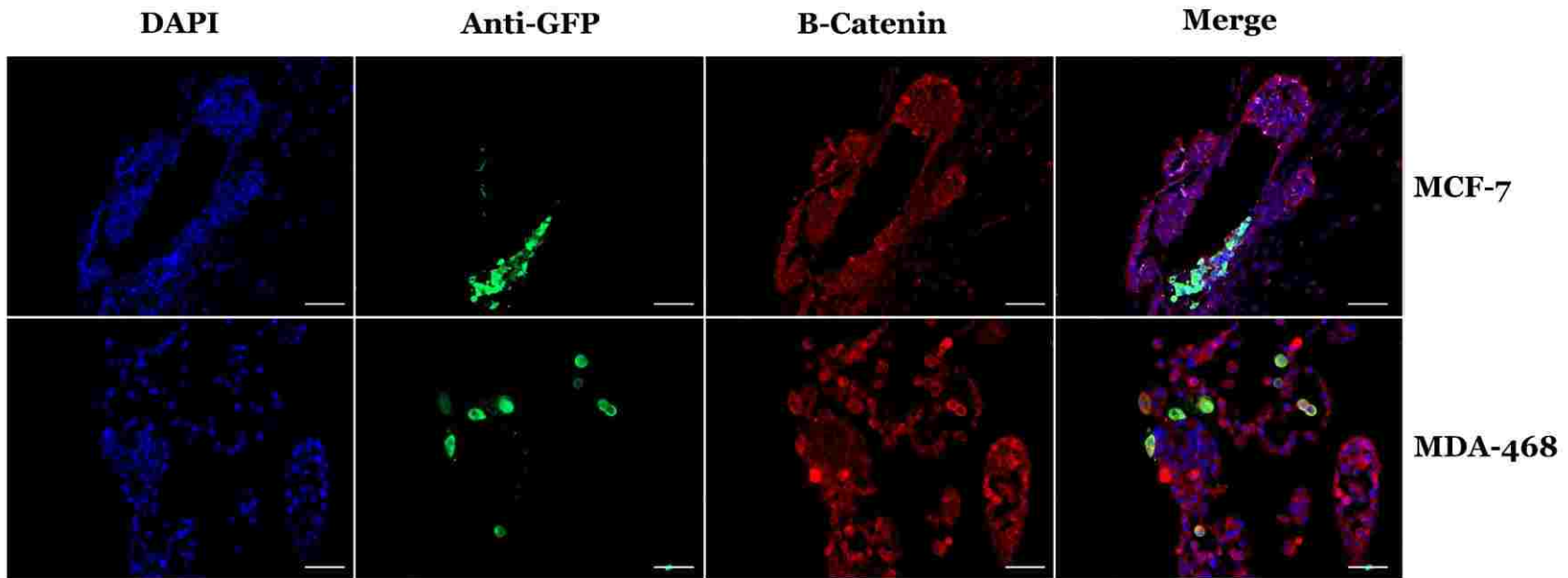


Fig. 25. Distribution of normal and tumorigenic cell types in chimeric organoids. Fluorescent microscopy confirmed the presence of GFP+, tumorigenic cell lines (MCF-7 or MDA-MB-468) inside MCF-12A organoid-structures.  $\beta$ -Catenin staining of MCF-12A and either tumorigenic cell line in chimeric organoids indicated all cell types were  $\beta$ -Catenin positive. Scale bar 100 $\mu$ m.

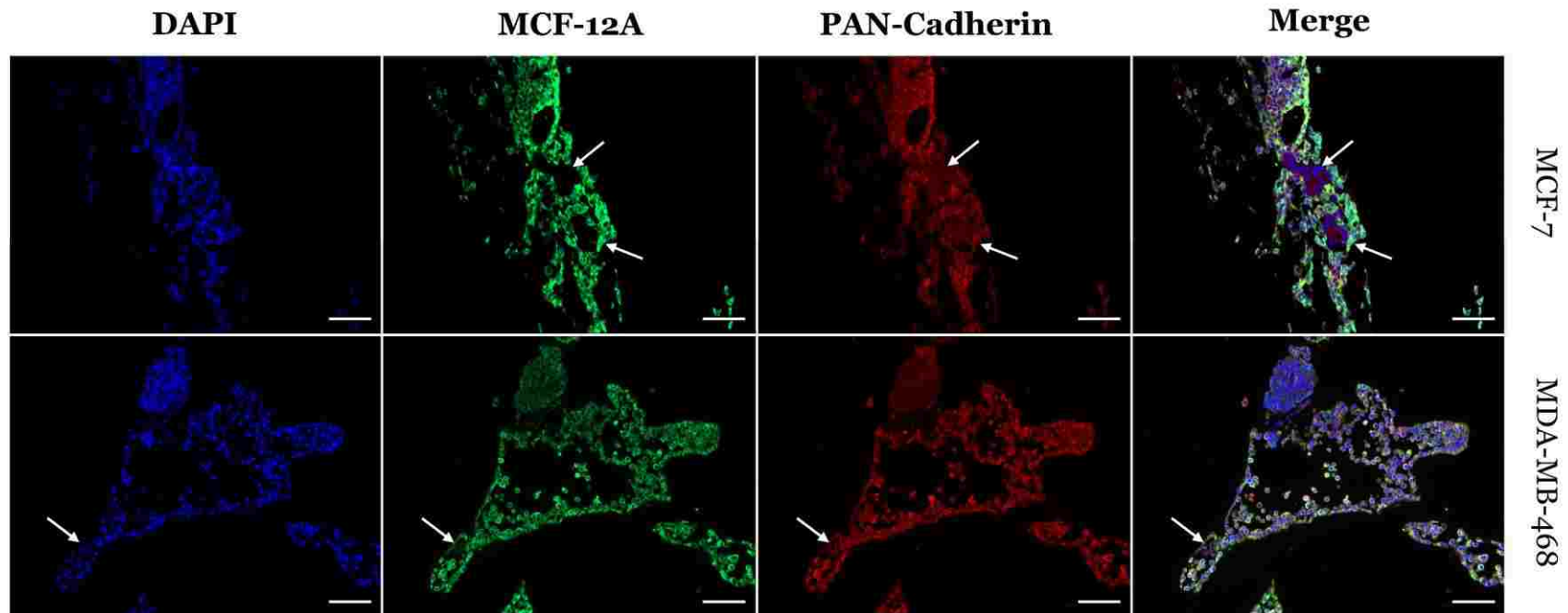


Fig. 26. Immunohistochemical comparison of cadherin expression in chimeric epithelial organoids. Examples of chimeric, epithelial organoid structures containing MCF-12A cells (shown in green) and either tumorigenic cell line (MCF-7 and MDA-MB-468) identified with arrows. Histological observations using pan-cadherin antibodies indicated MCF-7 cells within chimeric structures display less intense staining than neighboring MCF-12A cells. Pan-Cadherin staining in MDA-MB-468 cells exhibited more variable intensities. Scale bar 100 $\mu$ m.

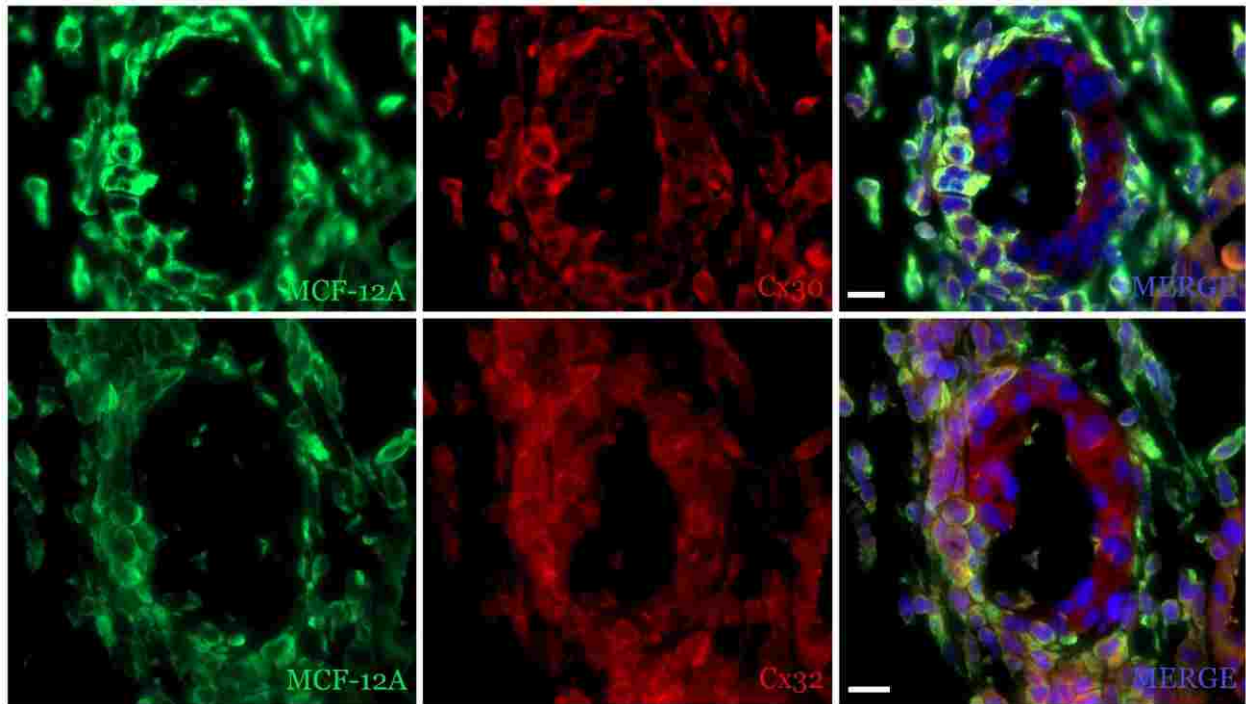


Fig. 27. Immunohistochemical comparison of connexin expression in chimeric epithelial organoids containing MCF-7 and MCF-12A cells. MCF-7 cells appear to display a decreased level of Cx-30 compared to neighboring MCF-12A cells. Cx-32 staining appears more variable in MCF-7 cells, however both MCF-7 and MCF-12A cells appear to express Cx-32. Scale bar 25 $\mu$ m.

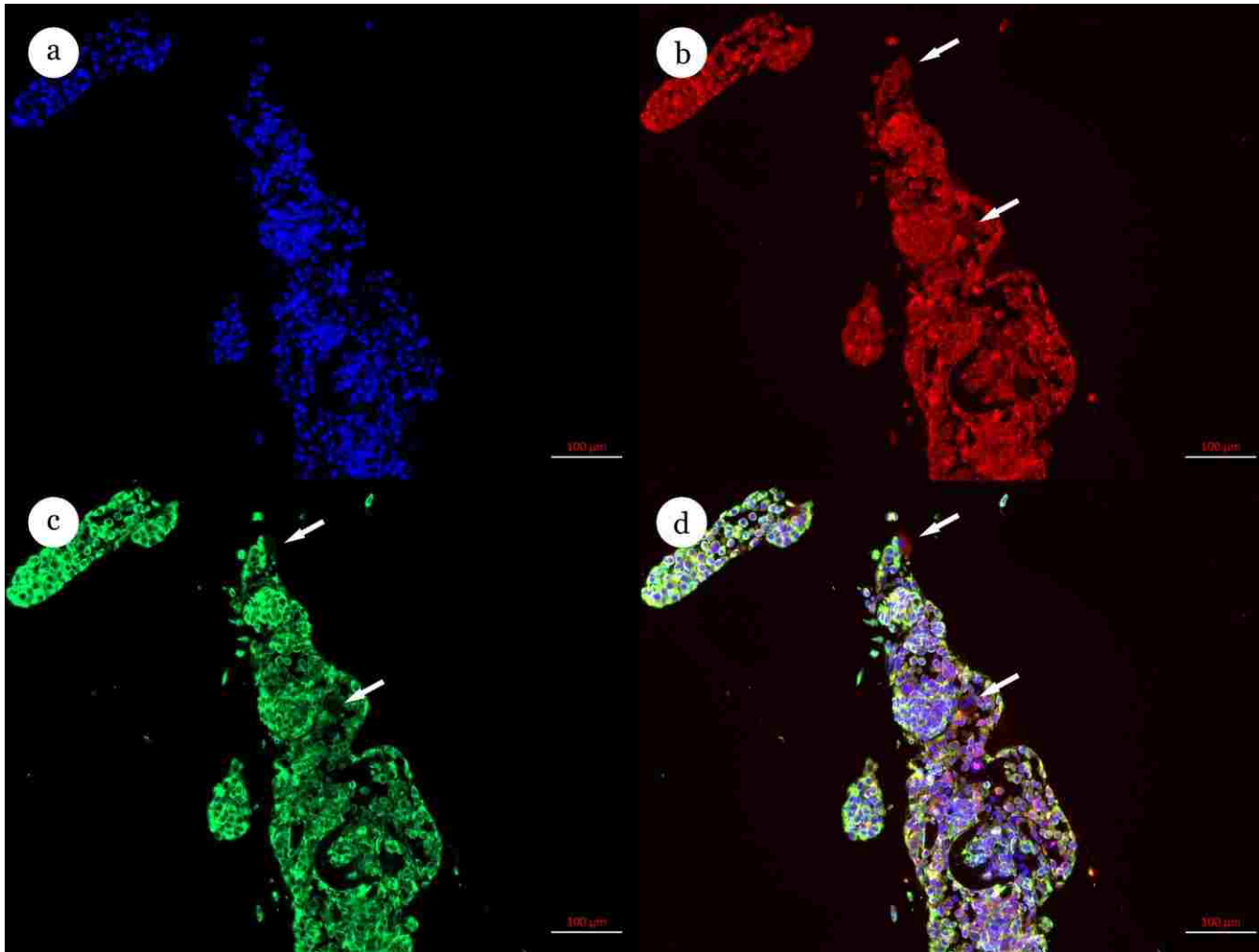


Fig. 28. Immunohistochemical comparison of connexin 30 (Cx30) expression in chimeric epithelial organoids containing MDA-MB-468 and MCF-12A cells. Both cell types express Cx30. Scale bar 100μm.

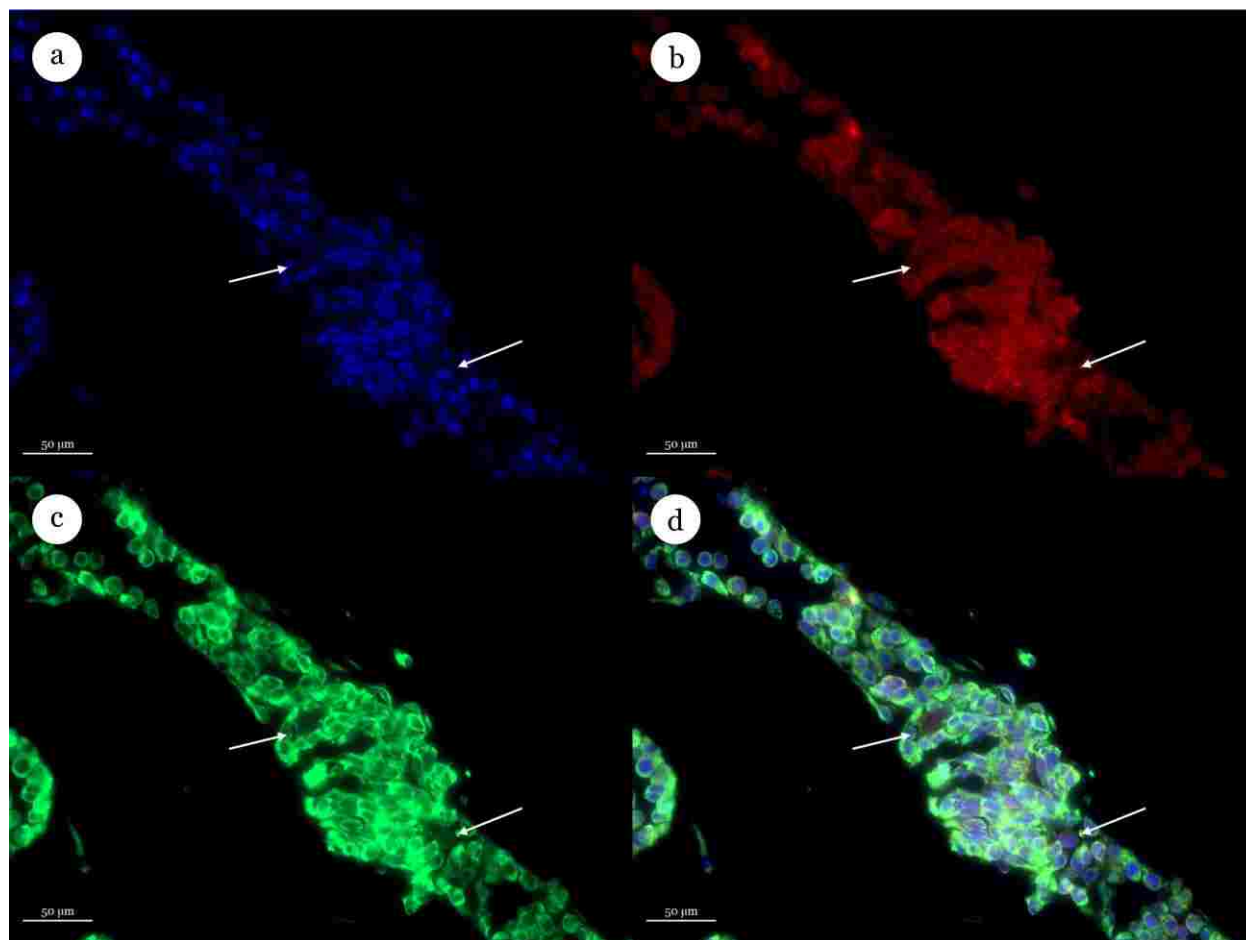


Fig. 29. Immunohistochemical comparison of connexin 32 (Cx32) expression in chimeric epithelial organoids containing MDA-MB-468 and MCF-12A cells. White arrows indicate MDA-MB-468 tumor cells. (b) Both cell types express Cx32. (c) MCF-12A cells shown in green. (d) Merged image. Scale bar 50μm.



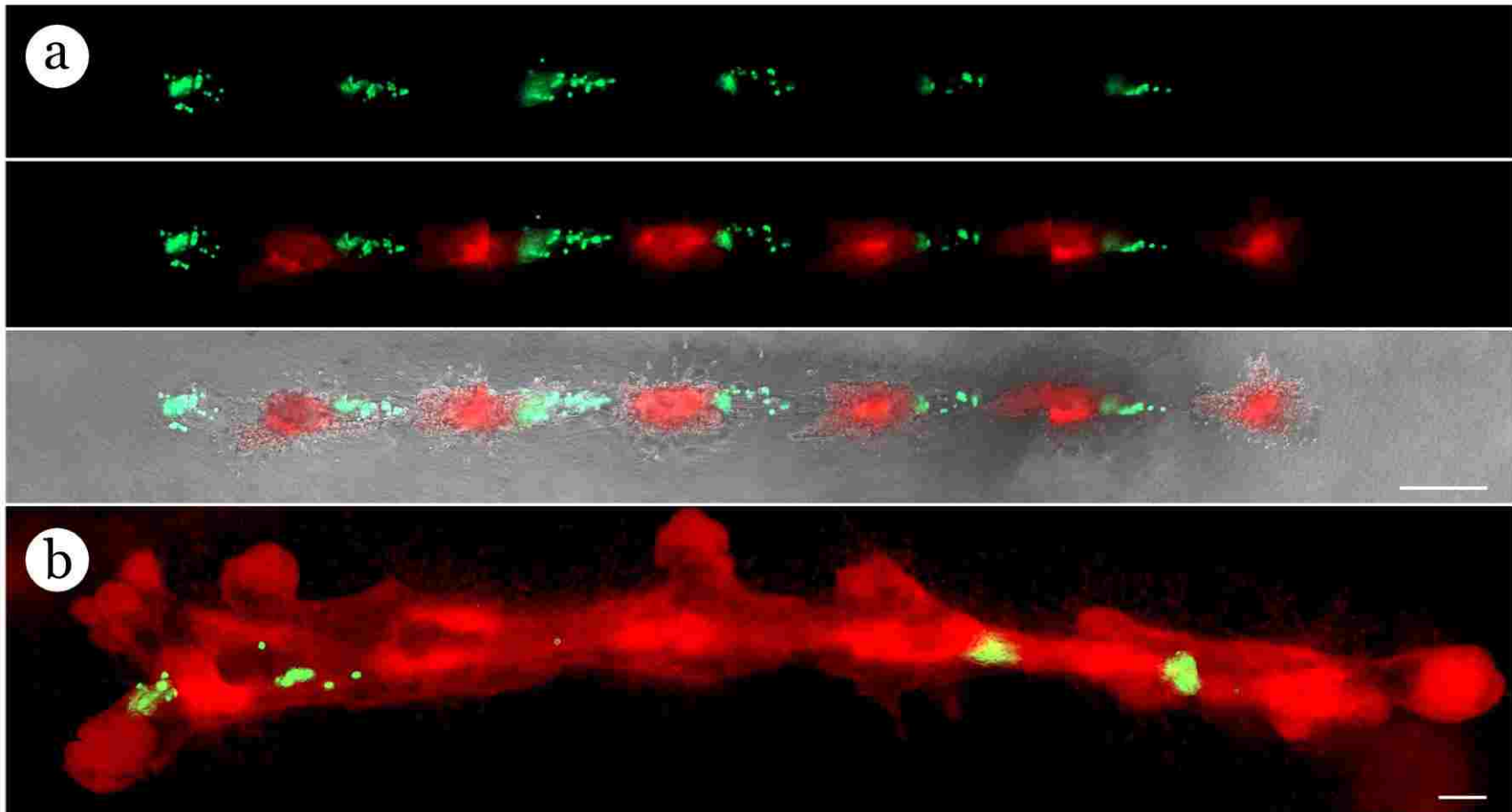


Fig. 30. Manipulating cell-cell interactions through bioprinting. (a) Day 3 results of GFP-MDA-MB-468 cell deposits spaced in-between MCF-12A cell deposits. Scale bar 200 $\mu$ m. (b) By day 7, MDA-MB-468 cell-extensions emerged from the end of the printed array. Scale bar 200 $\mu$ m.

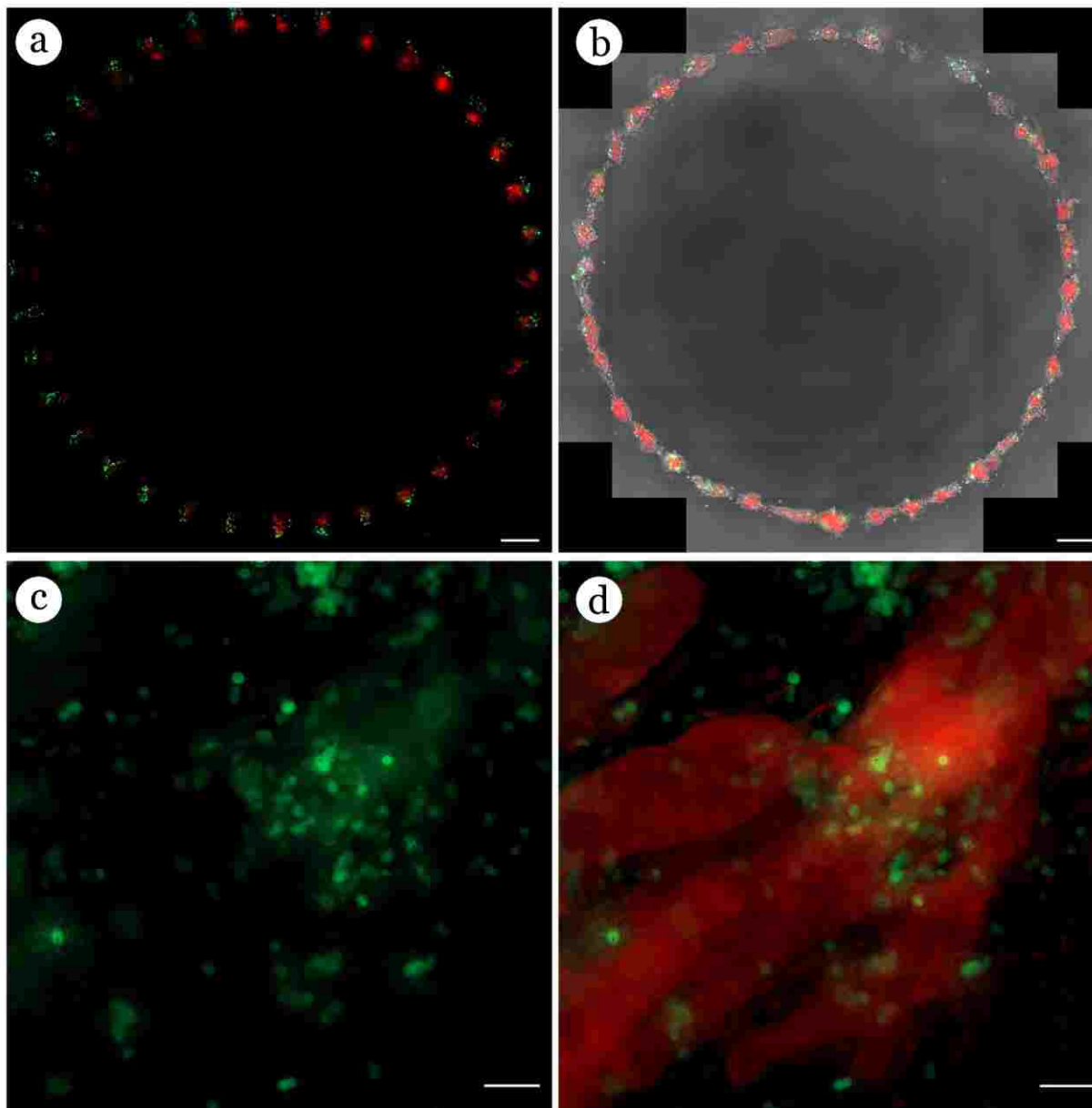


Fig. 31. Alternative methods for generating chimeric organoids. (a) GFP+ MDA-MB-468 cells and RFP+ MCF-12A cells printed independently as concentric rings. (b) By day 5, individual cell deposits fuse together to form a larger structure composed of both cell types. Scale bar 500 $\mu$ m. Tumorigenic cell types (c) can be introduced into previously developed MCF-12A cell-organoids (d). Evidence suggests some GFP+ MDA-MB-468 cells were successfully incorporated inside MCF-12A organoid structures from previous 21-day cultures. Scale bar 100 $\mu$ m.

#### *4.4.6 Manipulating Microenvironmental Cues Through Bioprinting*

In addition to increased efficiency, our bioprinting device also provides the ability to generate unique combinations, geometric configurations, and temporal additions of multiple cell types. Previously, we described organoid fusion events, where neighboring MECs initiate the formation of directional extensions to generate organized, large epithelial structures. Presumably, the areas where these restructuring processes occur contain ‘normal’ developmental cues. To determine if human cancer cell organoids could be influenced by these interactions, we utilized our bioprinting apparatus to place tumor-only cell-deposits between normal-MEC cell-deposits in equally spaced, linear arrays. Within 3 days, GFP-labeled MDA-MB-468 cells located in-between MCF-12A organoids appear to conform to the directional orientation of the merging MCF-12A structures in the bioprinted array (Fig. 30a, Sup. Movie 4.3). MDA-MB-468 cells located in-between normal organoids were incorporated into large, chimeric organoid structures (Fig. 30b). In addition to placing tumor cells between normal cell-deposits, we also wanted to determine the possibility of generating chimeric organoids by printing tumor and normal cells as separate, concentric rings (Fig. 31a). Within 5 days, we observed the formation of chimeric organoids, and no remaining evidence of the separate rings was present (Fig. 31b). These results suggest organoid formation is not limited to initial cell mixtures alone. Specifically, neighboring MCF-12A cells can influence the directional growth of tumor-only cell-deposits.

In addition to investigating tumorigenic responses to developing MEC organoids, we evaluated the potential use of our bioprinting device to deposit cells in mature stages of organoid development. To this end, we were able to successfully introduce tumorigenic cells into an established, 3-week culture containing mature MEC organoid-structures (Fig. 31c,d). These results indicate the bioprinting methods described here are capable of placing multiple cell types in more than just initial cell mixtures, which has been a major limitation of manual matrix embedding methods.

## 4.5 Discussion

This work provides a description of how bioprinting technology can be utilized to standardize current and future chimeric models of 3D epithelial cell culture assays. As such, 3D bioprinting platforms are ideally suited to facilitate the high-throughput analysis of potential mechanisms related to cancer cell redirection. To reliably recreate ‘context’ *in vitro* requires technologies capable of investigating how multiple cell types elicit changes in ECM before, during and after organoid development<sup>112</sup>. Conventional methods for studying tumor cell behaviors have relied on injection of tumor cells into cleared mammary fat pads, Boyden assays, or random 3D matrix embedding assays. While each of these methods offers its own advantages, they are difficult to optimize for visualization and biophysical parameter control, such as spatial and temporal control over experimental conditions. This report provides evidence of the superiority of bioprinting systems over conventional methods for studying tumor cell behaviors, particularly in the context of cancer cell redirection. Furthermore, the ability to introduce tumorigenic cells into epithelial organoid-structures from 21-day cultures of MCF-12A cells suggests our bioprinting method is not limited to a single, initial cell placement. This advantage gives us the ability to ask previously unanswerable, interesting questions such as: what would happen if we introduced ‘normal’ cell types into established tumor organoids?

We report the ability to generate chimeric epithelial structures containing focal outgrowths that radially expand into unoccupied regions of a collagen I gel. After a few days post-printing, these foci of epithelial growth show a centrally located lumen and the earliest development of a duct, and what appears to be a ‘TEB-like’ structure. By standardizing the process of 3D mammary epithelial organoid formation, we believe this system may provide a potential method to reliably-investigate the contextual properties of the *in vivo* situation.

Understanding the bidirectional communication between tumor cells and their microenvironment represents a powerful, advantageous way to investigate the mechanisms that influence disease promotion and progression. Furthermore, identifying the contextual contributions related to ‘normalizing’ or reversing the tumor-specific ECM associated with cancer stands as an interesting target for novel screening methods and therapeutic targets for clinical tumor therapy.

## 4.6 Conclusion

The study of breast cancer itself has ‘evolved’ in the past decade; research has migrated away from 2D culture and xenotransplantation, towards fully-humanized, 3D model systems. But, as with most things, our ability to address the experimental complexity required to further scientific investigations of this disease have been limited due to a lack of available technology. Through the ability to create and control 3D environments with a significantly increased level of precision, our bioprinting platform represents a scientific ‘catalyst’ to further advance the capabilities of *in vitro* models of numerous biological systems. While the experiments reported here represent the successful achievement of the last objective of this work, this achievement represents just the beginning of our main aim to incorporate this powerful technology to design personalized ‘microenvironments’ that better recapitulate the *in vivo* situation. Specifically, incorporating multiple cell-lines with reporter genes in our organoid arrays may provide a further method to systematically identify the factors that are integral to the normal niche, and thus sufficient to direct neoplastic mammary cells toward normal cell behavior. As our understanding of biological systems continues to develop in breadth and complexity, the ability to use bioprinting to assist in any combinatorial approach to model these dynamic interactions may be the only means necessary to fully comprehend the roles of the numerous agents involved in most biological systems.

We shall not cease from exploration,  
And the end of all our exploring  
Will be to arrive where we started  
And know the place for the first time.

T. S. Eliot

## CHAPTER 5

### SUMMARY AND FUTURE WORK

#### 5.1 Summary of the Current Study

In this study, we addressed the need to further technical advances towards the development of disease models using 3D, *in vitro* cell cultures that accurately recapitulate the *in vivo* situation. While 3D bioprinting technology is not new, the technology has yet to be heavily incorporated in current experimental techniques due to the uncertainty as to whether the research benefit will outweigh the operational cost. Furthermore, most commercially available 3D bioprinters are unable to address the unique research demands of individual research labs. Importantly, this work identified the need to overcome the limitations imposed by conventional, ‘luer-lock’ syringe systems in commercially available bioprinters. Furthermore, the custom system demonstrated the ability to handle precise cell quantities, without compromising fragile cell types. Thus, we believe we were successful in completing the first objective of this investigation, to design and develop 3D bioprinting technology capable of completing experimental tasks related to precision cell handling.

Next, we utilized our system to address the experimental inconsistency of manual cell matrix embedding techniques commonly used in MEC research. Results showed that placing multiple cells in confined locations is a viable method for generating arrays of bioprinted, MEC organoids. Results indicated a positive relationship between the number of initial cells and the amount of time required for MEC organoid formation. Importantly, our 3D bioprinted MEC organoids were of uniform size and morphology, indicating this method is sufficient for eliminating the experimental inconsistency associated with manual methods.

We then used the bioprinting platform to identify effective distances to generate large, epithelial structures that resembled the initial print geometry. This organoid ‘fusion’ process was further investigated by patterning alternating GFP and RFP-labeled MECs in a single, bioprinted array. After 14 days in culture, results indicated neighboring RFP and GFP-labeled cell-deposits underwent coordinated, interacting behaviors to generate a contiguous RFP/GFP epithelial structure. Overall, these results highlight the ability of 3D bioprinting to direct individual organoid formation, and to control the ‘self-assembly’ of large epithelial structures through coordinated, organoid fusion events. These findings indicate we successfully completed our second main objective, which was to identify the parameters associated with reliable MEC organoid generation and the ability to direct the formation of large epithelial structures using 3D bioprinting.

Given the importance of the cellular environment in regulating cellular signaling, we investigated the ability of our bioprinting platform to further advance *in vitro* methods for the study of cell-cell interactions among tumorigenic cell lines (MCF-7, MDA-MB-468) and normal cell line (MCF-12A). As expected, when compared to manual embedding methods, 3D bioprinted co-cultures of MCF-12A and either tumorigenic cell line (MCF-7, MDA-MB-468) resulted in a significant increase in chimeric organoid formation at 1 (\*\* $p < 0.001$ ) and 2 weeks (\* $p < 0.01$ ) (Table 2.). Furthermore, tumorigenic cell-deposits located in between ‘normal’ MCF-12A cell-deposits appear to conform to the linear growth pattern directed by organoid ‘fusion’ determined by the print geometry. This method may provide a potential means to recapitulate the effect of developing tissue environments, and as such it could offer an effective method to improve studies of tumor cell behavior. Given our ability to deposit multiple cell types, reliably generate chimeric organoids, and provide evidence of the ability of MCF-12A organoids to influence neighboring tumorigenic cell behavior, we believe we were successful in completing the third objective of this work.

## 5.2 Additional Considerations for Future Research

Previous investigations into the early events of 3D morphogenesis of human MECs revealed that 3D structures undergo a coordinated rotational movement, and this process is required for assembly of laminins and collagen around the 3D structures<sup>37</sup>. This rotational motion

was independent of the cell cycle, and was directly related to the assembly of endogenous BM around the 3D structures<sup>37</sup>. Furthermore, structures formed by cancer-derived cell lines failed to display rotational motion, and were defective in weaving exogenous laminin matrix<sup>37</sup>. Interestingly, dissolution of BM around mature, nonrotating acini, restored rotational movement and the ability to assemble exogenous laminin<sup>37</sup>. Together, these findings indicate that coordinated rotational motion during 3D morphogenesis of MEC acini is a significant, regulating feature of the BM assembly process.

Given the importance of rotational motion in developing MEC tissues, we utilized time-lapse imaging surveys of developing, bioprinted, MEC structures to determine the presence of rotational motion. Throughout the first week of culture, data indicated our bioprinted MEC cell aggregates underwent coordinated, cell-cell interactions to produce a rotational motion in the direction of forward growth (Sup. Movie 3.1). Overall, it appears that the process of rotational motion may be intimately related to the collective migration of cells. Similar to the way water flows out of a spring to form a river, cells appear to ‘flow’ across the entire organoid structure in the direction of active growth (Sup. Movie 3.2). Given our bioprinted MEC organoids exhibit collective, rotational motion, we believe this data provides evidence in support of our primary goal of validating our 3D bioprinting technology for generating MEC organoids. While the role of rotational motion in establishing a properly assembled BM is not fully understood, in future studies, our bioprinting technology stands as an ideal platform to controllably investigate and understand the mechanisms that regulate cell-cell and cell-matrix interactions, despite their state of constant flux.

Throughout our investigation to develop methods to reliably maintain cell-deposits inside a 3D hydrogel, we noted microneedle geometries with taper lengths less than the programmed insertion depth of the needle tip typically resulted in a broad circular deformation on the top of the collagen I gel. While this increase in gel-deformation did not alter the ability of our bioprinter to maintain cells in the target area, MECs were able to follow this opening and proliferate in the 2D environment on-top of the gel. Interestingly, these cells would then encompass the deformed, needle insertion point while maintaining cell-cell linkage with the developing organoid-structure deep within the gel. This process resulted in the generation of individual ‘sprout-like’ structures at each injection site in the 3D gel. Using time-lapse imaging to track the behavior of migrating cells inside these ‘sprout-like’ structures, we found the cells within the tips of these structures



appeared to uniformly rotate in a ‘fluid-like’ motion associated with BM assembly<sup>37</sup>(Sup. Movie 5.1). Throughout the culture period, the initial ‘sprout’ grew in diameter and length to resemble TEB structures seen *in vivo* (Fig. 25a). Further, some of these structures began to form secondary branches, indicating that these structures were not just artifacts from the needle insertion routine (Sup. Movie 5.1). The rotational motion was always perpendicular to the direction of the elongating duct (Fig. 25b). Additionally, the rotational motion was observed in both clockwise and counterclockwise directions among neighboring ‘TEB-like’ structures (Sup. Movie 5.1).

Similar ‘TEB-like’ structures resulted using MCF-7 and MDA-MB-468 tumorigenic cell lines, which suggests this effect is conserved across multiple mammary cell lines, albeit without secondary branches or rotational motion (Fig. 25c,d). Similar to the numerous, previously stated discrepancies among the two tumor cell lines, both tumor cell lines exhibited unique growth morphologies under these conditions. While the overall shape of the structures from MDA-MB-468 cells were similar to MCF-12A structures, the appearance of MDA-MB-468 structures was less smooth due to the presence of extensive fingerlike projections. ‘TEB-like’ structures of MCF-7 cells were long narrow tubes, with what appears to be consistent, tightly woven cell-cell contacts (Fig. 25d). While the meaning of this unexpected, yet interesting result has not been thoroughly investigated, we noted this process would only occur when a hole was maintained between the inside and outside layer of the gel. Could the physical presence of an ‘opening’ provide instructive cues for the initial polarization and lumen formation in the developing mammary epithelium? Indeed, for every functional mammary gland, an ‘opening’ must be created to the outside through the nipple. The nipple is where the fetal epidermis initially invaginates into the mammary fat pad, and as such it represents the growth point origin of the mammary epithelium. We also find it interesting to note that the mammary glands of male rats develop similarly to females but have no external connection to the epidermis. While we currently do not know what processes control the formation of the nipple ‘opening’ through the skin above the fetal anlage, the physical deformation of gel materials, similar to the disruption of gel materials described above, certainly presents one possible way to generate such an ‘opening’ *in vitro*.

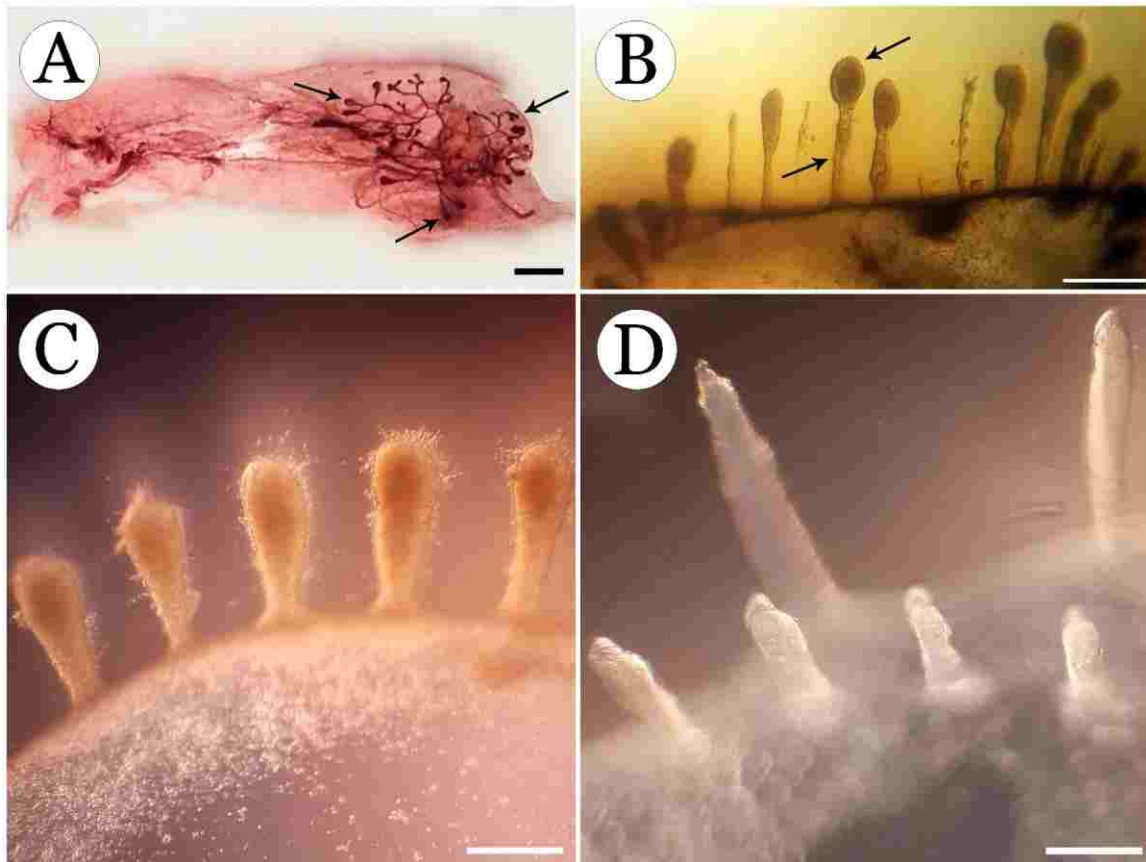


Fig. 32. Bioprinted breast organoids form ‘TEB-like’ morphologies. ‘TEB-like’ morphology results when cell-deposits are able to maintain linkage to the surface of 3D gels. (a) Section of a developing mouse mammary gland. Black arrows point to ‘TEB’ structures. Scale bar 1 mm. (b) ‘TEB-like’ structures grown *in vitro* after 14 days in culture using MCF-12A cells. Black arrows point to rounded cell mass located at the end of ‘stalk-like’ structure. Scale bar 500 $\mu$ m. Tumorigenic cell lines MDA-MB-468 (c) and MCF-7 (d) also formed similar ‘TEB-like’ structures at 14 days. Scale bar 500 $\mu$ m.

### 5.3 Future Directions for Bioprinting in MEC Research

One of the most iconic, yet mysterious structures in the mammary system is the TEB. The environment created by the TEB appears to elicit important features of regulatory signaling in the developing gland. For example, the TEB is the regulatory control point for basement membrane deposition, branching, angiogenesis, and pattern formation<sup>8,10</sup>. Also, the signaling pathways which drive and regulate the directional growth and motility of TEBs are responsible for establishing the primary structure of the entire mammary tree<sup>16</sup>. Despite advances in our understanding of the genetic regulation of mammary development<sup>3</sup>, the cellular basis of ductal elongation or bifurcation remains unknown. Active TEBs are also of a special interest, due to their ability to recruit stromal cells, heterogeneous cellular composition, invasive ability, angiogenic properties, and high proliferation rate (60-90%)<sup>10</sup>. Thus, any method that would create an *in vitro* model of the developing TEB, would represent an ideal model of the constant flux among cell-cell and cell-matrix interactions that regulate mammary gland growth and development. Furthermore, given 90% of human mammary cancers are of ductal origin, fully understanding the processes related to ductal growth would represent a significant advancement in the battle against breast cancer.

Additional areas of research should also focus on determining the contribution of cell types outside of the epithelium compartment in the development and function of the mammary gland. As our bioprinting device has the capability to place multiple cell types within close proximity, it stands as an optimal candidate to systematically investigate the impact of additional cell types on MEC behavior.

While our extrusion based bioprinting device has been able to achieve the reliable control of small cell quantities, our current bioprinting technology is still affected by cell settling due to the force of gravity. A solution to this can be as simple as increasing the viscosity of the cell containing bio-ink. This would also increase the extrusion force, which may negatively impact the extrusion process. For this reason, limiting the effect of cell settling stands as a key area to advance this technology.

Another method to improve our current bioprinting technology could come from incorporating cell surface marker sorting technology into the injection device. This would provide the capability to isolate and select specific cell populations during the printing process. Additionally, current cell sorting approaches have been known to vary between studies, which

makes quantitative comparisons of the prevalence of different populations difficult<sup>3</sup>. For example, a tenfold increase in gland reconstitution in one study was shown to be related to transplant conditions, suggestive of the dramatic effect of transplant conditions on reconstitution efficiency<sup>149</sup>. Thus, incorporating this technology with bioprinting devices would have a significant impact on performing assays designed to identify the different epithelial cell populations with stem cell properties. As stem cells are intimately related to normal development and tissue pathologies, future studies will require methods for evaluating the role of these cells during mammary development and cancer.

One of the greatest impacts of bioprinting technology is the high-throughput generation of 3D cultures. However, the increased proficiency in generating 3D cultures means nothing if there is no equally matched system to analyze results. To this end, incorporating artificial intelligence and machine learning algorithms to systematically measure experimental results, such as histological slides and 3D image stacks, stands as the most logical method to retain consistency among thousands of experiments. However, just like the need to ‘tailor-fit’ 3D culture conditions to the cell type, these algorithms must be fine-tuned and maintained for each individual experiment. For example, traditional methods for measuring Ki67 staining rely on observer discretion. While routine training can help control inter-observer variance, the amount of Ki67 bound nuclei is better represented with a ratio scale than a nominal scale (binary: yes/no). One could understand how setting a numerical threshold in an algorithm would result in a significant improvement in scoring data. We have begun to incorporate these protocols for analyzing histological sections and other large 3D image stacks. For example, in the case of Ki67 staining, we can utilize specific features of DAPI stained nuclei to detect and label each nucleus in any given slide (Fig. 33a1-a2). Next, these labels can be overlaid onto the original Ki67 image (Fig. 33a3-a4). This method allows us to determine the corrected total cell flux for each nucleus in the sample, which provides more specific quantification of overall Ki67 activation.

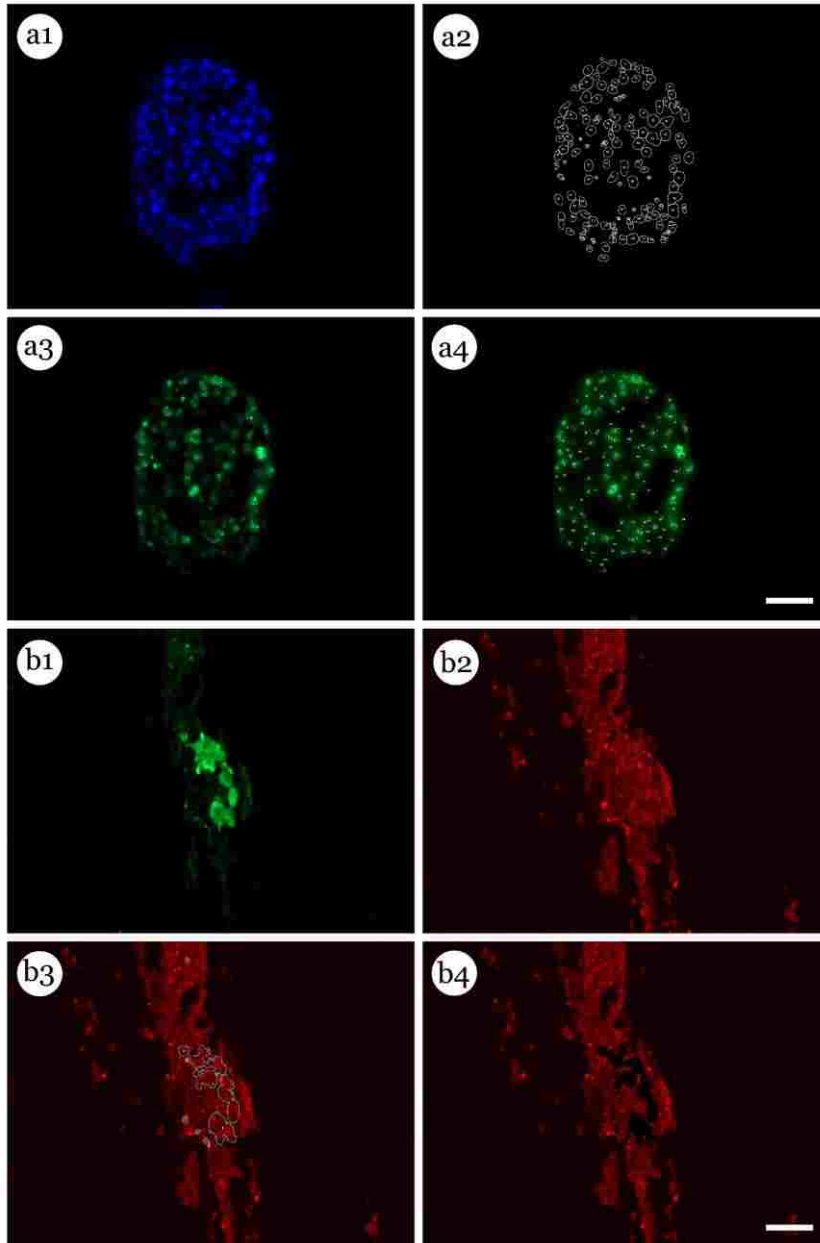


Fig. 33. Algorithm to standardize measurement of histological data. (a) To measure Ki-67 staining, nuclei (a1) are identified and counted to make a mask (a2) which can then be applied to Ki-67 staining (a3) to determine scoring data. (b) Isolating sub-populations in histological slides. (b1) GFP labeled MCF-7 cells inside chimeric organoid. (b2)  $\beta$ -catenin staining of chimeric organoid. (b3) MCF-7 cell population identified by algorithm. (b4) MCF-7 cell area subtracted from original  $\beta$ -catenin image. Scale bar 50 $\mu$ m.

Furthermore, this method can be utilized for additional proteins and histological assays. For example, consider GFP-labeled, MCF-7 cells in chimeric organoids (Fig. 33b1). Given the overall expression of  $\beta$ -catenin in a single histological slide (Fig. 33b2), if we identify the GFP-labeled MCF-7 cells (Fig. 33b3) and remove these objects from the original  $\beta$ -catenin image (Fig. 33b4), we can isolate the region of a distinct member from the original image. Similar to the Ki67 protocol, we can then calculate the corrected total cell flux for just the MCF-7 cells or MCF-12A cell population. Using this method, large batch analysis of experimental conditions can be simultaneously, and quantitatively compared without observer bias, which ultimately function to reduce both intra and inter-laboratory variance.

## 5.4 Conclusion

Overall, the future challenge for mammary research is to place the genes and proteins they encode into the larger picture of mammary development and function. Pertinent to this task of understanding the physiological significance of the unique proteins in the puzzle of mammary gland development will be the introduction of *in vitro* approaches that use genetically manipulated primary cells or cell lines to form a functional epithelium. Further, these *in vitro* constructs could then be implanted *in vivo* to define their position in the signaling networks related to mammary gland development. Furthering our use and development of these systems will be invaluable in modelling tumor progression and testing pharmacological agents in a biologically relevant context.

Here we detailed the custom-design and use of 3D bioprinting systems to improve upon conventional methods for studying tumor cell behaviors in 3D assays. These results indicate microfabrication techniques have the potential to become valuable tools in mimicking distinct properties of the *in vivo* situation. We expect the use of these systems will provide new perspectives and opportunities for future research design.

Investigating the histological patterns of both invasive and preinvasive tumors associated with breast carcinomas stands as a highly valuable means of obtaining prognostic information. As much remains to be learned about how the genotypic abnormalities associated with cancer elicit the phenotypic changes related to tumorigenesis, any technology capable of systematically investigating these mechanisms will be useful. Through the imaginative, new perspectives and

opportunities provided by bioprinting techniques, we are currently working on utilizing these microfabrication techniques as a tool for mimicking distinct properties of the *in vivo* situation. Thus, our bioprinting platform would provide the ideal method to generate high-throughput assays of primary tumor cells from patient biopsies. Therefore, in addition to acting as a multipurpose technique for a range of applications including biomedical implants and tissue engineering, we believe the greatest impact of 3D bioprinting technology may come from the potential service as an important diagnostic platform for clinicians in treatment centers and hospitals everywhere.

## REFERENCES

- 1 Nelson, C. M. & Bissell, M. J. Of extracellular matrix, scaffolds, and signaling: tissue architecture regulates development, homeostasis, and cancer. *Annu Rev Cell Dev Biol* **22**, 287-309 (2006).
- 2 Neville, M. C., Medina, D., Monks, J. & Hovey, R. C. The mammary fat pad. *J Mammary Gland Biol Neoplasia* **3**, 109-116 (1998).
- 3 Inman, J. L., Robertson, C., Mott, J. D. & Bissell, M. J. Mammary gland development: cell fate specification, stem cells and the microenvironment. *Development* **142**, 1028-1042 (2015).
- 4 Adriance, M. C., Inman, J. L., Petersen, O. W. & Bissell, M. J. Myoepithelial cells: good fences make good neighbors. *Breast Cancer Res* **7**, 190-197 (2005).
- 5 Sonnenberg, A., Daams, H., Van der Valk, M. A., Hilkens, J. & Hilgers, J. Development of mouse mammary gland: identification of stages in differentiation of luminal and myoepithelial cells using monoclonal antibodies and polyvalent antiserum against keratin. *J Histochem Cytochem* **34** (1986).
- 6 Sekhri, K. K., Pitelka, D. R. & DeOme, K. B. Studies of mouse mammary glands. I. Cytomorphology of the normal mammary gland. *J Natl Cancer Inst* **39**, 459-490 (1967).
- 7 Silberstein, G. B. Postnatal mammary gland morphogenesis. *Microsc Res Tech* **52**, 155-162 (2001).
- 8 Williams, J. M. & Daniel, C. W. Mammary ductal elongation: differentiation of myoepithelium and basal lamina during branching morphogenesis. *Dev Biol* **97**, 274-290 (1983).
- 9 Shackleton, M. *et al.* Generation of a functional mammary gland from a single stem cell. *Nature* **439**, 84-88 (2006).
- 10 Paine, I. S. & Lewis, M. T. The Terminal End Bud: the Little Engine that Could. *J Mammary Gland Biol Neoplasia* **22**, 93-108 (2017).
- 11 Russo, J. & Russo, I. H. DNA Labeling Index and Structure of Rat Mammary-Gland as Determinants of Its Susceptibility to Carcinogenesis. *J Natl Cancer I* **61**, 1451-1459 (1978).
- 12 Silberstein, G. B. & Daniel, C. W. Glycosaminoglycans in the basal lamina and extracellular matrix of the developing mouse mammary duct. *Dev Biol* **90**, 215-222 (1982).
- 13 Ewald, A. J., Brenot, A., Duong, M., Chan, B. S. & Werb, Z. Collective epithelial migration and cell rearrangements drive mammary branching morphogenesis. *Dev Cell* **14**, 570-581 (2008).
- 14 Fleury, V. & Watanabe, T. Morphogenesis of fingers and branched organs: how collagen and fibroblasts break the symmetry of growing biological tissue. *C R Biol* **325**, 571-583 (2002).
- 15 Faulkin, L. J., Jr. & Deome, K. B. Regulation of growth and spacing of gland elements in the mammary fat pad of the C3H mouse. *J Natl Cancer Inst* **24**, 953-969 (1960).
- 16 Hinck, L. & Silberstein, G. B. Key stages in mammary gland development: the mammary end bud as a motile organ. *Breast Cancer Res* **7**, 245-251 (2005).
- 17 Wiseman, B. S. *et al.* Site-specific inductive and inhibitory activities of MMP-2 and MMP-3 orchestrate mammary gland branching morphogenesis. *J Cell Biol* **162**, 1123-1133 (2003).
- 18 Hu, M. C. & Rosenblum, N. D. Genetic regulation of branching morphogenesis: lessons learned from loss-of-function phenotypes. *Pediatr Res* **54**, 433-438 (2003).
- 19 Daniel, C. W., Robinson, S. & Silberstein, G. B. The transforming growth factors beta in development and functional differentiation of the mouse mammary gland. *Adv Exp Med Biol* **501**, 61-70 (2001).
- 20 Hennighausen, L. & Robinson, G. W. Information networks in the mammary gland. *Nat Rev Mol Cell Biol* **6**, 715-725 (2005).
- 21 Davies, J. A. *Branching morphogenesis*. Springer Science (2006).
- 22 Smith, G. H. Experimental mammary epithelial morphogenesis in an in vivo model: evidence for distinct cellular progenitors of the ductal and lobular phenotype. *Breast Cancer Res Treat* **39**, 21-31 (1996).
- 23 Smith, G. H. & Boulanger, C. A. Mammary epithelial stem cells: transplantation and self-renewal analysis. *Cell Prolif* **36 Suppl 1**, 3-15 (2003).
- 24 Kordon, E. C. & Smith, G. H. An entire functional mammary gland may comprise the progeny from a single cell. *Development* **125**, 1921-1930 (1998).
- 25 Deome, K. B., Faulkin, L. J., Jr., Bern, H. A. & Blair, P. B. Development of mammary tumors from hyperplastic alveolar nodules transplanted into gland-free mammary fat pads of female C3H mice. *Cancer Res* **19**, 515-520 (1959).
- 26 Mintz, B. & Illmensee, K. Normal genetically mosaic mice produced from malignant teratocarcinoma cells. *Proc Natl Acad Sci U S A* **72**, 3585-3589 (1975).



- 27 Legate, K. R., Wickstrom, S. A. & Fassler, R. Genetic and cell biological analysis of integrin outside-in signaling. *Genes Dev* **23**, 397-418 (2009).
- 28 El-Sabban, M. E., Abi-Mosleh, L. F. & Talhouk, R. S. Developmental regulation of gap junctions and their role in mammary epithelial cell differentiation. *J Mammary Gland Biol Neoplasia* **8**, 463-473 (2003).
- 29 Gudjonsson, T. *et al.* Normal and tumor-derived myoepithelial cells differ in their ability to interact with luminal breast epithelial cells for polarity and basement membrane deposition. *J Cell Sci* **115**, 39-50 (2002).
- 30 Bissell, M. J., Hall, H. G. & Parry, G. How does the extracellular matrix direct gene expression? *J Theor Biol* **99**, 31-68 (1982).
- 31 Vichas, A. & Zallen, J. A. Translating cell polarity into tissue elongation. *Semin Cell Dev Biol* **22**, 858-864 (2011).
- 32 Streuli, C. H. & Bissell, M. J. Expression of extracellular matrix components is regulated by substratum. *J Cell Biol* **110**, 1405-1415 (1990).
- 33 Emerman, J. T. & Pitelka, D. R. Maintenance and induction of morphological differentiation in dissociated mammary epithelium on floating collagen membranes. *In Vitro* **13**, 316-328 (1977).
- 34 Barcellos-Hoff, M. H., Aggeler, J., Ram, T. G. & Bissell, M. J. Functional differentiation and alveolar morphogenesis of primary mammary cultures on reconstituted basement membrane. *Development* **105**, 223-235 (1989).
- 35 Petersen, O. W., Ronnov-Jessen, L., Howlett, A. R. & Bissell, M. J. Interaction with basement membrane serves to rapidly distinguish growth and differentiation pattern of normal and malignant human breast epithelial cells. *Proc Natl Acad Sci U S A* **89**, 9064-9068 (1992).
- 36 O'Brien, L. E., Zegers, M. M. & Mostov, K. E. Opinion: Building epithelial architecture: insights from three-dimensional culture models. *Nat Rev Mol Cell Biol* **3**, 531-537 (2002).
- 37 Wang, H., Lacoche, S., Huang, L., Xue, B. & Muthuswamy, S. K. Rotational motion during three-dimensional morphogenesis of mammary epithelial acini relates to laminin matrix assembly. *Proc Natl Acad Sci U S A* **110**, 163-168 (2013).
- 38 Davis, G. E. & Cleaver, O. B. Outside in: inversion of cell polarity controls epithelial lumen formation. *Dev Cell* **31**, 140-142 (2014).
- 39 Plachot, C. *et al.* Factors necessary to produce basoapical polarity in human glandular epithelium formed in conventional and high-throughput three-dimensional culture: example of the breast epithelium. *BMC Biol* **7**, 77 (2009).
- 40 Wozniak, M. A. & Keely, P. J. Use of three-dimensional collagen gels to study mechanotransduction in T47D breast epithelial cells. *Biol Proced Online* **7**, 144-161 (2005).
- 41 Overeem, A. W., Bryant, D. M. & van, I. S. C. Mechanisms of apical-basal axis orientation and epithelial lumen positioning. *Trends Cell Biol* **25**, 476-485 (2015).
- 42 Cassereau, L., Miroshnikova, Y. A., Ou, G., Lakins, J. & Weaver, V. M. A 3D tension bioreactor platform to study the interplay between ECM stiffness and tumor phenotype. *J Biotechnol* **193**, 66-69 (2015).
- 43 Carey, S. P., Martin, K. E. & Reinhart-King, C. A. Three-dimensional collagen matrix induces a mechanosensitive invasive epithelial phenotype. *Sci Rep* **7**, 42088 (2017).
- 44 Rodriguez-Fraticelli, A. E. & Martin-Belmonte, F. Picking up the threads: extracellular matrix signals in epithelial morphogenesis. *Curr Opin Cell Biol* **30**, 83-90 (2014).
- 45 Glukhova, M. A. & Streuli, C. H. How integrins control breast biology. *Curr Opin Cell Biol* **25**, 633-641 (2013).
- 46 Manninen, A. Epithelial polarity--generating and integrating signals from the ECM with integrins. *Exp Cell Res* **334**, 337-349 (2015).
- 47 Yonemura, S. Differential sensitivity of epithelial cells to extracellular matrix in polarity establishment. *PLoS One* **9**, e112922 (2014).
- 48 Begnaud, S., Chen, T., Delacour, D., Mege, R. M. & Ladoux, B. Mechanics of epithelial tissues during gap closure. *Curr Opin Cell Biol* **42**, 52-62 (2016).
- 49 Ravasio, A. *et al.* Gap geometry dictates epithelial closure efficiency. *Nat Commun* **6**, 7683 (2015).
- 50 Inman, J. L. & Bissell, M. J. Apical polarity in three-dimensional culture systems: where to now? *J Biol* **9**, 2 (2010).
- 51 Wang, F. *et al.* Reciprocal interactions between beta1-integrin and epidermal growth factor receptor in three-dimensional basement membrane breast cultures: a different perspective in epithelial biology. *Proc Natl Acad Sci U S A* **95**, 14821-14826 (1998).
- 52 Paszek, M. J. *et al.* Tensional homeostasis and the malignant phenotype. *Cancer Cell* **8**, 241-254 (2005).

- 53 Kleinman, H. K. & Martin, G. R. Matrigel: basement membrane matrix with biological activity. *Semin Cancer Biol* **15**, 378-386 (2005).
- 54 Barnes, C. *et al.* From single cells to tissues: interactions between the matrix and human breast cells in real time. *PLoS One* **9**, e93325 (2014).
- 55 Dhimolea, E., Soto, A. M. & Sonnenschein, C. Breast epithelial tissue morphology is affected in 3D cultures by species-specific collagen-based extracellular matrix. *J Biomed Mater Res A* **100**, 2905-2912 (2012).
- 56 Rudnicki, M. S. *et al.* Nonlinear strain stiffening is not sufficient to explain how far cells can feel on fibrous protein gels. *Biophys J* **105**, 11-20 (2013).
- 57 Stopak, D. & Harris, A. K. Connective tissue morphogenesis by fibroblast traction. I. Tissue culture observations. *Dev Biol* **90**, 383-398 (1982).
- 58 Vanni, S., Lagerholm, B. C., Otey, C., Taylor, D. L. & Lanni, F. Internet-based image analysis quantifies contractile behavior of individual fibroblasts inside model tissue. *Biophys J* **84**, 2715-2727 (2003).
- 59 Dhimolea, E., Maffini, M. V., Soto, A. M. & Sonnenschein, C. The role of collagen reorganization on mammary epithelial morphogenesis in a 3D culture model. *Biomaterials* **31**, 3622-3630 (2010).
- 60 Foster, C. S., Smith, C. A., Dinsdale, E. A., Monaghan, P. & Neville, A. M. Human mammary gland morphogenesis in vitro: the growth and differentiation of normal breast epithelium in collagen gel cultures defined by electron microscopy, monoclonal antibodies, and autoradiography. *Dev Biol* **96**, 197-216 (1983).
- 61 Krause, S., Maffini, M. V., Soto, A. M. & Sonnenschein, C. A novel 3D in vitro culture model to study stromal-epithelial interactions in the mammary gland. *Tissue Eng Part C Methods* **14**, 261-271 (2008).
- 62 Wozniak, M. A., Desai, R., Solski, P. A., Der, C. J. & Keely, P. J. ROCK-generated contractility regulates breast epithelial cell differentiation in response to the physical properties of a three-dimensional collagen matrix. *J Cell Biol* **163**, 583-595 (2003).
- 63 Weaver, V. M. *et al.* Reversion of the malignant phenotype of human breast cells in three-dimensional culture and in vivo by integrin blocking antibodies. *J Cell Biol* **137**, 231-245 (1997).
- 64 Ouyang, L. *et al.* Three-dimensional bioprinting of embryonic stem cells directs highly uniform embryoid body formation. *Biofabrication* **7**, 044101 (2015).
- 65 Murphy, S. V. & Atala, A. 3D bioprinting of tissues and organs. *Nature Biotechnology* **32**, 773-785 (2014).
- 66 Aguado, B. A., Mulyasmita, W., Su, J., Lampe, K. J. & Heilshorn, S. C. Improving Viability of Stem Cells During Syringe Needle Flow Through the Design of Hydrogel Cell Carriers. *Tissue Engineering Part A* **18**, 806-815 (2012).
- 67 Vaezi, M., Seitz, H. & Yang, S. F. A review on 3D micro-additive manufacturing technologies. *Int J Adv Manuf Tech* **67**, 1721-1754 (2013).
- 68 Highley, C. B., Rodell, C. B. & Burdick, J. A. Direct 3D Printing of Shear-Thinning Hydrogels into Self-Healing Hydrogels. *Adv Mater* **27**, 5075-5079 (2015).
- 69 Wang, Y., Adokoh, C. K. & Narain, R. Recent development and biomedical applications of self-healing hydrogels. *Expert Opin Drug Deliv* **15**, 77-91 (2018).
- 70 Kola, I. & Landis, J. Can the pharmaceutical industry reduce attrition rates? *Nature Reviews Drug Discovery* **3**, 711-715 (2004).
- 71 Meacham, C. E. & Morrison, S. J. Tumour heterogeneity and cancer cell plasticity. *Nature* **501**, 328-337 (2013).
- 72 Sun, X. X. & Yu, Q. Intra-tumor heterogeneity of cancer cells and its implications for cancer treatment. *Acta Pharmacol Sin* **36**, 1219-1227 (2015).
- 73 Junttila, M. R. & de Sauvage, F. J. Influence of tumour micro-environment heterogeneity on therapeutic response. *Nature* **501**, 346-354 (2013).
- 74 Albini, A. & Sporn, M. B. The tumour microenvironment as a target for chemoprevention. *Nat Rev Cancer* **7**, 139-147 (2007).
- 75 Egeblad, M., Nakasone, E. S. & Werb, Z. Tumors as organs: complex tissues that interface with the entire organism. *Dev Cell* **18**, 884-901 (2010).
- 76 Polyak, K., Haviv, I. & Campbell, I. G. Co-evolution of tumor cells and their microenvironment. *Trends Genet* **25**, 30-38 (2009).
- 77 Bissell, M. J. & Radisky, D. Putting tumours in context. *Nat Rev Cancer* **1**, 46-54 (2001).
- 78 Radisky, D., Hagios, C. & Bissell, M. J. Tumors are unique organs defined by abnormal signaling and context. *Semin Cancer Biol* **11**, 87-95 (2001).
- 79 Xu, F. *et al.* A three-dimensional in vitro ovarian cancer coculture model using a high-throughput cell patterning platform. *Biotechnol J* **6**, 204-212 (2011).
- 80 Horvath, L. *et al.* Engineering an in vitro air-blood barrier by 3D bioprinting. *Sci Rep* **5**, 7974 (2015).

- 81 Santis, R. *et al.* Advanced composites for hard-tissue engineering based on PCL/organic-inorganic hybrid fillers: From the design of 2D substrates to 3D rapid prototyped scaffolds. *Polymer Composites* **34**, 1413-1417 (2013).
- 82 Patricio, T. *et al.* Fabrication and characterisation of PCL and PCL/PLA scaffolds for tissue engineering. *Rapid Prototyping Journal* **20**, 145-156 (2014).
- 83 De Santis, R. *et al.* Towards the Design of 3D Fiber-Deposited Poly(epsilon-caprolactone)/Iron-Doped Hydroxyapatite Nanocomposite Magnetic Scaffolds for Bone Regeneration. *Journal of Biomedical Nanotechnology* **11**, 1236-1246 (2015).
- 84 Esposito, A. R. *et al.* PLDLA/PCL-T Scaffold for Meniscus Tissue Engineering. *Biores Open Access* **2**, 138-147 (2013).
- 85 Khalil, S., Nam, J. & Sun, W. Multi-nozzle deposition for construction of 3D biopolymer tissue scaffolds. *Rapid Prototyping Journal* **11**, 9-17 (2005).
- 86 Chang, R. & Sun, W. Effects of dispensing pressure and nozzle diameter on cell survival from solid freeform fabrication-based direct cell writing. *Tissue Engineering Part A* **14**, 41-48 (2008).
- 87 Tirella, A. & Ahluwalia, A. The impact of fabrication parameters and substrate stiffness in direct writing of living constructs. *Biotechnology Progress* **28**, 1315-1320 (2012).
- 88 Smith, C. M., Christian, J. J., Warren, W. L. & Williams, S. K. Characterizing environmental factors that impact the viability of tissue-engineered constructs fabricated by a direct-write bioassembly tool. *Tissue Engineering* **13**, 373-383 (2007).
- 89 Buyukhatipoglu, K., Jo, W. & Clyne, A. M. The role of printing parameters and scaffold biopolymer properties in the efficacy of a new hybrid nano-bioprinting system. *Biofabrication* **1** (2009).
- 90 Faulkner-Jones, A. *et al.* Development of a valve-based cell printer for the formation of human embryonic stem cell spheroid aggregates. *Biofabrication* **5** (2013).
- 91 Li, M. G., Tian, X. Y., Schreyer, D. J. & Chen, X. B. Effect of needle geometry on flow rate and cell damage in the dispensing-based biofabrication process. *Biotechnology Progress* **27**, 1777-1784 (2011).
- 92 Li, M. G., Tian, X. Y., Zhu, N., Schreyer, D. J. & Chen, X. B. Modeling Process-Induced Cell Damage in the Biodispensing Process. *Tissue Engineering Part C-Methods* **16**, 533-542 (2010).
- 93 Faulkner-Jones, A. *et al.* Bioprinting of human pluripotent stem cells and their directed differentiation into hepatocyte-like cells for the generation of mini-livers in 3D. *Biofabrication* **7** (2015).
- 94 Takahashi, K. & Yamanaka, S. Induction of pluripotent stem cells from mouse embryonic and adult fibroblast cultures by defined factors. *Cell* **126**, 663-676 (2006).
- 95 Park, J. *et al.* Microfabrication-based modulation of embryonic stem cell differentiation. *Lab on a Chip* **7**, 1018-1028 (2007).
- 96 Stolberg, S. & McCloskey, K. E. Can Shear Stress Direct Stem Cell Fate? *Biotechnology Progress* **25**, 10-19 (2009).
- 97 Yan, C. Q. *et al.* Injectable Solid Peptide Hydrogel as a Cell Carrier: Effects of Shear Flow on Hydrogels and Cell Payload. *Langmuir* **28**, 6076-6087 (2012).
- 98 Baden, T. *et al.* Open Labware: 3-D Printing Your Own Lab Equipment. *Plos Biology* **13** (2015). [10.1371/journal.pbio.1002175](https://doi.org/10.1371/journal.pbio.1002175) (2015).
- 99 Fusaki, N., Ban, H., Nishiyama, A., Saeki, K. & Hasegawa, M. Efficient induction of transgene-free human pluripotent stem cells using a vector based on Sendai virus, an RNA virus that does not integrate into the host genome. *Proc Jpn Acad Ser B Phys Biol Sci* **85**, 348-362 (2009).
- 100 Martanto, W., Baisch, S. M., Costner, E. A., Prausnitz, M. R. & Smith, M. K. Fluid dynamics in conically tapered microneedles. *AIChE Journal* **51**, 1599-1607 (2005).
- 101 Floren, M. & Tan, W. Three-dimensional, soft neotissue arrays as high throughput platforms for the interrogation of engineered tissue environments. *Biomaterials* **67**, 204-204 (2015).
- 102 Wust, S., Godla, M. E., Muller, R. & Hofmann, S. Tunable hydrogel composite with two-step processing in combination with innovative hardware upgrade for cell-based three-dimensional bioprinting. *Acta Biomaterialia* **10**, 630-640 (2014).
- 103 Nair, K. *et al.* Characterization of cell viability during bioprinting processes. *Biotechnol J* **4**, 1168-1177 (2009).
- 104 Billiet, T., Gevaert, E., De Schryver, T., Cornelissen, M. & Dubruel, P. The 3D printing of gelatin methacrylamide cell-laden tissue-engineered constructs with high cell viability. *Biomaterials* **35**, 49-62 (2014).
- 105 Roeder, B. A., Kokini, K. & Voytik-Harbin, S. L. Fibril microstructure affects strain transmission within collagen extracellular matrices. *J Biomech Eng* **131**, 031004 (2009).

- 106 Doyle, A. D., Carvajal, N., Jin, A., Matsumoto, K. & Yamada, K. M. Local 3D matrix microenvironment regulates cell migration through spatiotemporal dynamics of contractility-dependent adhesions. *Nat Commun* **6**, 8720 (2015).
- 107 Baker, M. 1,500 scientists lift the lid on reproducibility. *Nature* **533**, 452-454 (2016).
- 108 Reid, J. A. *et al.* Accessible bioprinting: adaptation of a low-cost 3D-printer for precise cell placement and stem cell differentiation. *Biofabrication* **8**, 025017 (2016).
- 109 Ranga, A. *et al.* 3D niche microarrays for systems-level analyses of cell fate. *Nat Commun* **5**, 4324 (2014).
- 110 Linnemann, J. R. *et al.* Quantification of regenerative potential in primary human mammary epithelial cells. *Development* **142**, 3239-3251 (2015).
- 111 Boyd, N. F., Lockwood, G. A., Byng, J. W., Trichler, D. L. & Yaffe, M. J. Mammographic densities and breast cancer risk. *Cancer Epidemiol Biomarkers Prev* **7**, 1133-1144 (1998).
- 112 Maller, O., Martinson, H. & Schedin, P. Extracellular matrix composition reveals complex and dynamic stromal-epithelial interactions in the mammary gland. *J Mammary Gland Biol Neoplasia* **15**, 301-318 (2010).
- 113 Sokol, E. S. *et al.* Growth of human breast tissues from patient cells in 3D hydrogel scaffolds. *Breast cancer research : BCR* **18**, 19 (2016).
- 114 Bruno, R. D. *et al.* Mammary extracellular matrix directs differentiation of testicular and embryonic stem cells to form functional mammary glands in vivo. *Sci Rep* **7**, 40196 (2017).
- 115 Bruno, R. D. *et al.* Paracrine-rescued lobulogenesis in chimeric outgrowths comprising progesterone-receptor-null mammary epithelium and redirected wild-type testicular cells. *J Cell Sci* **127**, 27-32 (2014).
- 116 Bruno, R. D. & Smith, G. H. Reprogramming non-mammary and cancer cells in the developing mouse mammary gland. *Semin Cell Dev Biol* **23**, 591-598 (2012).
- 117 Bruno, R. D., Boulanger, C. A. & Smith, G. H. Notch-induced mammary tumorigenesis does not involve the lobule-limited epithelial progenitor. *Oncogene* **31**, 60-67 (2012).
- 118 Boulanger, C. A., Bruno, R. D., Rosu-Myles, M. & Smith, G. H. The mouse mammary microenvironment redirects mesoderm-derived bone marrow cells to a mammary epithelial progenitor cell fate. *Stem Cells Dev* **21**, 948-954 (2012).
- 119 Boulanger, C. A. *et al.* Embryonic stem cells are redirected to non-tumorigenic epithelial cell fate by interaction with the mammary microenvironment. *PLoS One* **8**, e62019 (2013).
- 120 Francis, M. P., Sachs, P. C., Elmore, L. W. & Holt, S. E. Isolating adipose-derived mesenchymal stem cells from lipoaspirate blood and saline fraction. *Organogenesis* **6**, 11-14 (2010).
- 121 Sachs, P. C. *et al.* Defining essential stem cell characteristics in adipose-derived stromal cells extracted from distinct anatomical sites. *Cell Tissue Res* **349**, 505-515 (2012).
- 122 Zhao, M. *et al.* Mesenchymal stem cells in mammary adipose tissue stimulate progression of breast cancer resembling the basal-type. *Cancer Biol Ther* **13**, 782-792 (2012).
- 123 Nakasone, E. S. *et al.* Imaging tumor-stroma interactions during chemotherapy reveals contributions of the microenvironment to resistance. *Cancer Cell* **21**, 488-503 (2012).
- 124 Jeanes, A. I., Maya-Mendoza, A. & Streuli, C. H. Cellular microenvironment influences the ability of mammary epithelia to undergo cell cycle. *PLoS One* **6**, e18144 (2011).
- 125 Wilmut, I., Schnieke, A. E., McWhir, J., Kind, A. J. & Campbell, K. H. Viable offspring derived from fetal and adult mammalian cells. *Nature* **385**, 810-813 (1997).
- 126 Hochedlinger, K. *et al.* Reprogramming of a melanoma genome by nuclear transplantation. *Genes Dev* **18**, 1875-1885 (2004).
- 127 Dolberg, D. S. & Bissell, M. J. Inability of Rous sarcoma virus to cause sarcomas in the avian embryo. *Nature* **309**, 552-556 (1984).
- 128 Rosenfield, S. M. & Smith, G. H. Redirection of Human Cancer Cells upon the Interaction with the Regenerating Mouse Mammary Gland Microenvironment. *Cells* **2**, 43-56 (2013).
- 129 Sakakura, T., Nishizuka, Y. & Dawe, C. J. Mesenchyme-dependent morphogenesis and epithelium-specific cytodifferentiation in mouse mammary gland. *Science* **194**, 1439-1441 (1976).
- 130 Cunha, G. R. *et al.* Mammary phenotypic expression induced in epidermal cells by embryonic mammary mesenchyme. *Acta Anat (Basel)* **152**, 195-204 (1995).
- 131 Bussard, K. M., Boulanger, C. A., Booth, B. W., Bruno, R. D. & Smith, G. H. Reprogramming human cancer cells in the mouse mammary gland. *Cancer Res* **70**, 6336-6343 (2010).
- 132 Boulanger, C. A., Mack, D. L., Booth, B. W. & Smith, G. H. Interaction with the mammary microenvironment redirects spermatogenic cell fate in vivo. *Proc Natl Acad Sci U S A* **104**, 3871-3876 (2007).
- 133 Boulanger, C. A. & Smith, G. H. Reprogramming cell fates in the mammary microenvironment. *Cell Cycle* **8**, 1127-1132 (2009).

- 134 Smith, G. H. *et al.* Long-term in vivo expression of genes introduced by retrovirus-mediated transfer into  
mammary epithelial cells. *J Virol* **65**, 6365-6370 (1991).
- 135 Holton, S. E., Bergamaschi, A., Katzenellenbogen, B. S. & Bhargava, R. Integration of molecular profiling  
and chemical imaging to elucidate fibroblast-microenvironment impact on cancer cell phenotype and  
endocrine resistance in breast cancer. *PLoS One* **9**, e96878 (2014).
- 136 Yang, C. C. & Burg, K. J. Designing a tunable 3D heterocellular breast cancer tissue test system. *J Tissue  
Eng Regen Med* **9**, 310-314 (2015).
- 137 Wang, X. *et al.* A complex 3D human tissue culture system based on mammary stromal cells and silk  
scaffolds for modeling breast morphogenesis and function. *Biomaterials* **31**, 3920-3929 (2010).
- 138 Campbell, J. J. *et al.* A 3-D in vitro co-culture model of mammary gland involution. *Integr Biol (Camb)* **6**,  
618-626 (2014).
- 139 Wang, F. *et al.* Phenotypic reversion or death of cancer cells by altering signaling pathways in three-  
dimensional contexts. *J Natl Cancer Inst* **94**, 1494-1503 (2002).
- 140 Muschler, J. *et al.* A role for dystroglycan in epithelial polarization: loss of function in breast tumor cells.  
*Cancer Res* **62**, 7102-7109 (2002).
- 141 Howlett, A. R., Petersen, O. W., Steeg, P. S. & Bissell, M. J. A novel function for the nm23-H1 gene:  
overexpression in human breast carcinoma cells leads to the formation of basement membrane and growth  
arrest. *J Natl Cancer Inst* **86**, 1838-1844 (1994).
- 142 Rizki, A. *et al.* A human breast cell model of preinvasive to invasive transition. *Cancer Res* **68**, 1378-1387  
(2008).
- 143 Straussman, R. *et al.* Tumour micro-environment elicits innate resistance to RAF inhibitors through HGF  
secretion. *Nature* **487**, 500-504 (2012).
- 144 Weigelt, B., Ghajar, C. M. & Bissell, M. J. The need for complex 3D culture models to unravel novel  
pathways and identify accurate biomarkers in breast cancer. *Adv Drug Deliv Rev* **69-70**, 42-51 (2014).
- 145 Zhou, Y. *et al.* Multiparameter analyses of three-dimensionally cultured tumor spheroids based on respiratory  
activity and comprehensive gene expression profiles. *Anal Biochem* **439**, 187-193 (2013).
- 146 Schiemann, S., Schwirzke, M., Brunner, N. & Weidle, U. H. Molecular analysis of two mammary carcinoma  
cell lines at the transcriptional level as a model system for progression of breast cancer. *Clin Exp Metastasis*  
**16**, 129-139 (1998).
- 147 Arteaga, C. L., Hurd, S. D., Dugger, T. C., Winnier, A. R. & Robertson, J. B. Epidermal growth factor  
receptors in human breast carcinoma cells: a potential selective target for transforming growth factor alpha-  
*Pseudomonas* exotoxin 40 fusion protein. *Cancer Res* **54**, 4703-4709 (1994).
- 148 Hollestelle, A. *et al.* Four human breast cancer cell lines with biallelic inactivating alpha-catenin gene  
mutations. *Breast Cancer Res Treat* **122**, 125-133 (2010).
- 149 Spike, B. T. *et al.* A mammary stem cell population identified and characterized in late embryogenesis reveals  
similarities to human breast cancer. *Cell Stem Cell* **10**, 183-197 (2012).

## APPENDICES

### APPENDIX A: GELATION PROTOCOL FOR COLLAGEN I, RAT TAIL

Place on ice the following:

- 1.1 Corning Collagen I, rat tail
- 1.2 Sterile phosphate buffered saline (PBS)
- 1.3 Sterile 1 N NaOH
- 1.4 Sterile tube of sufficient capacity
- 2.0 Determine the Desired Collagen Concentration (mg/mL).
- 3.0 Determine the total volume of Collagen I solution required to perform the experiment ( $V_{total}$ )
- 4.0 Place on ice a sterile tube of sufficient capacity to contain the final volume of Collagen I ( $V_{total}$ ).
- 5.0 Use the following equation to calculate the volume of stock collagen ( $V_{stock}$ ) to achieve the Desired Collagen Concentration (step 2.0) and the total volume of collagen I solution ( $V_{total}$ ) required for the experiment (step 3.0).

$$Vol. of Stock Collagen (V_{stock}) = \frac{\left( \text{Desired Collagen Concentration} \frac{mg}{mL} \right) \times (V_{total} mL)}{\text{Stock Collagen Concentration} \frac{mg}{mL}}$$

- 6.0 Determine the volume of sterile, ice cold 1 N NaOH required for the experiment ( $V_{NaOH}$ ).  
 $Volume of NaOH (V_{NaOH}) = V_{stock}(mL) \times 0.023 mL$

- 7.0 Next, determine the volume of PBS required for the experiment ( $V_{PBS}$ ) by subtracting  $V_{NaOH}$  and  $V_{stock}$  (step 5.0 & 6.0) from the total volume of collagen I solution required for the experiment  $V_{total}$  (step 3.0).

$$Volume of PBS (V_{PBS}) = V_{total} - V_{stock} - V_{NaOH}$$

- 8.0 Perform the following steps, in the provided order, using aseptic technique.
- 8.1 Add the required volume of sterile, ice-cold PBS ( $V_{PBS}$ ) to the sterile tube on ice.
- 8.2 Next, add the required volume of sterile, ice-cold 1 N NaOH ( $V_{NaOH}$ ) to the volume of PBS ( $V_{PBS}$ ).
- 8.3 Mix the contents of tube and place in ice.
- 8.4 Add the calculated volume of stock collagen ( $V_{stock}$ ), mix, and leave on ice until ready for use.
- 9.0 Aseptically deliver collagen solution into cell culture device and allow to get at 37°C for at least 30 minutes prior to printing. If not used immediately, collagen solution may be held on ice for 2-3 hours.

## VITA

### JOHN A. REID

College of Engineering & Technology  
Stem Cell Lab, Suite 365  
4211 Monarch Way  
Norfolk, VA 23508

#### EDUCATION

**Old Dominion University** Norfolk, VA  
Ph.D. Biomedical Engineering 2018

Dissertation: “3D Bioprinting Systems for the Study of Mammary Development and Tumorigenesis”

**Hampden-Sydney College** Hampden-Sydney, VA  
BA, with Honors in Psychology & Pre-Medicine 2009

#### RESEARCH EXPERIENCE

**Old Dominion University** Norfolk, VA  
Design, development and utilization of a 3D bioprinting device for tissue engineering.

- Invented and manufactured an adaptable, 3D bioprinter with single cell printing resolution using accessible, ‘off the shelf’ components.
- Used state of the art computational modeling tools to optimize the bioprinting process to enable the high-throughput fabrication of high-fidelity, cell constructs in 3D.
- Developed methods to control embryoid body formation with induced pluripotent stem cells.
- Improved methods of 3D mammary epithelial cell culture through bioprinting.
- Directed branching morphogenesis of human mammary epithelial cell-organoids via bioprinting.
- Engineered bioprinted, chimeric mammary models using normal & tumorigenic cell lines to investigate microenvironmental cues related to tumor suppression and promotion.

#### HONORS & AWARDS

Biomedical Engineering Ph.D. Researcher of the Year (2017-2018) Old Dominion University

First authored paper was included in “Highlights of 2016 collection”, a special issue of IOP Science journal Biofabrication.

“This collection includes some of the very best and most influential research published in BF last year. The selected articles present excellent cutting-edge research; they have received the highest praise from our international referees and the largest number of downloads from our readers”

- IOP SCIENCE